Analog fast Fourier transforms for scalable and efficient signal processing

T. Patrick Xiao[1*], Ben Feinberg[1], David K. Richardson[1], Matthew Cannon[1], Calvin Madsen[1], Harsha Medu[2], Vineet Agrawal[2], Matthew J. Marinella[3], Sapan Agarwal[4], Christopher H. Bennett[1*]

[1*]Sandia National Laboratories, Albuquerque, 87123, New Mexico, USA.
[2]Infineon Technologies, San Jose, 95134, California, USA.
[3]Department of Electrical, Computer, and Energy Engineering, Arizona State University, Tempe, 85281, Arizona, USA.
[4]Sandia National Laboratories, Livermore, 94551, California, USA.

*Corresponding author(s). E-mail(s): txiao@sandia.gov; cbennet@sandia.gov;
Contributing authors: bfeinbe@sandia.gov; dkricha@sandia.gov; mcannon@sandia.gov; cfmadse@sandia.gov; Harsha.Medu@infineon.com; Vineet.Agrawal@infineon.com; m@asu.edu; sagarwa@sandia.gov;

Abstract

Edge devices are being deployed at increasing volumes to sense and act on information from the physical world. The discrete Fourier transform (DFT) is often necessary to make this sensed data suitable for further processing – such as by artificial intelligence (AI) algorithms – and for transmission over communication networks. Analog in-memory computing has been shown to be a fast, energy-efficient, and scalable solution for processing edge AI workloads, but not for Fourier transforms. This is because of the existence of the fast Fourier transform (FFT) algorithm, which enormously reduces the complexity of the DFT but has so far belonged only to digital processors. Here, we show that the FFT can be mapped to analog in-memory computing systems, enabling them to efficiently scale to arbitrarily large Fourier transforms without requiring large sizes or large numbers of non-volatile memory arrays. We experimentally demonstrate analog FFTs on 1D audio and 2D image signals, performing analog computations on up to 524K charge-trapping memory devices simultaneously, where each device has precisely tunable, low-conductance analog states. The scalability of both the new analog FFT approach and the charge-trapping memory device is leveraged to compute a 65,536-point analog DFT, a scale that is otherwise inaccessible by analog systems and which is $>500\times$ larger than any previous analog DFT demonstration. Analog FFT cores can provide higher energy efficiency and performance per area than specialized digital FFT processors at all FFT sizes, while also functioning as efficient matrix multiplication engines for AI workloads.

1. Introduction

The increasing deployment of remote and inter-connected sensors and actuators is leading to the collection of ever greater volumes of data from the physical world. Acting on this information in real time requires computation to be done where the data is sensed, and the raw sensed signals must often be processed by linear transforms to be made suitable for further processing, communication, or storage. One of the most ubiquitous transforms is the discrete Fourier transform (DFT), which converts spatial or temporal digital signals to their frequency representation. When used in edge or Internet-of-Things (IoT) devices, the DFT can form images of the sensed environment from radar or lidar raw data [1–4], process raw audio signals to aid in speech recognition [5, 6], and modulate signals for wireless communication with other IoT devices [7–9]. Though the need for processing at the edge is rapidly growing, the end of Dennard scaling means that there will no longer be improvements to the energy per arithmetic operation using CMOS logic [10]. Conventional digital processors may soon prove inadequate for the large-scale data processing capabilities that are desired in future edge devices.

Analog in-memory computing (IMC) systems are a potential solution to overcome these scaling limits. These systems exploit analog circuit laws to rapidly and efficiently compute matrix-vector multiplications (MVMs) inside memory arrays, while greatly reducing the crippling energy overhead of data movement between the memory and processor in traditional von Neumann architectures [11–13]. These advantages enable analog IMC to process machine learning (ML) inference workloads with potentially orders-of-magnitude greater performance per watt, as explored in numerous recent works [14–21]. However, these benefits have yet to fully materialize for executing the large DFT operations that often come before or after the ML algorithm in edge systems, and would thus become the bottleneck. This is because while the DFT can be expressed as an MVM, it can be computed using far fewer mathematical operations by using the fast Fourier transform (FFT) algorithm [22]. While the FFT has been an indispensable instrument of digital signal processing (DSP) for decades, analog IMC systems have yet to capitalize on the benefits of the FFT, severely limiting their efficiency and scalability.

Analog IMC systems to date have relied exclusively on a direct MVM mapping of the DFT and its real-only counterpart, the discrete cosine transform (DCT) [23]. With this approach, analog IMC retains its low energy-per-operation only up to DFT sizes that can fit within a single memory array. Therefore, the largest experimentally demonstrated analog DFTs and DCTs have been limited to 64 or 128 points per dimension [24–28]. Relying on these prior methods would preclude analog processing from scaling to the much larger DFT sizes that are routinely needed for many practical applications. For example, mobile or IoT devices that use 5G wireless communications standards need to support FFTs of up to 4096 points to generate orthogonal frequency-division multiplexing (OFDM) waveforms [29]. Large 2D FFTs with well over 1000 or 10,000 points per dimension also enable high-resolution range-velocity maps using frequency-modulated continuous wave (FMCW) lidar or radar for autonomous vehicles [30, 31], as well as high-resolution synthetic aperture radar imagery for satellite- or aircraft-based remote sensing applications [32].

In this article, we demonstrate a new, more scalable mapping of the Fourier transform onto analog IMC architectures that is based on the classic Cooley-Tukey FFT algorithm [33]. This method factorizes large DFTs into smaller elementary DFTs that are computed by analog MVMs, which enables a small number of modestly sized memory arrays to efficiently process arbitrarily large DFTs. Compared to prior analog IMC approaches, the analog FFT reduces the energy and area scaling of the DFT from $O(N^2)$ to $O(N\log N)$, just as the original FFT algorithm reduced the complexity of the DFT on digital processors. The analog FFT can also yield more accurate DFT computation at any transform size, independently of the memory technology used for computing. The superior scalability of the analog FFT extends the practical range of mathematical kernels that can be efficiently processed using analog IMC. This enables a flexible architecture of analog IMC cores (Fig. 1e) that can be re-programmed to accelerate different kernels, such as neural network layers and FFTs, to achieve low-power end-to-end execution of edge workloads.

As a proof-of-concept, we implemented analog FFTs on a large array of charge-trapping flash memory devices based on the silicon-oxide-nitride-oxide-silicon (SONOS) material stack, which was fabricated in a 40-nm complementary metal-oxide-semiconductor (CMOS) process. The subthreshold operation and precise analog programmability of this memory enables half a million devices to simultaneously participate in a single analog MVM while retaining high accuracy. We used the SONOS array to experimentally compute the frequency spectra of 1D audio and 2D image signals. Leveraging the scalability of both the FFT and the memory technology, we compute analog DFTs of up to 65,536 points, which is more than

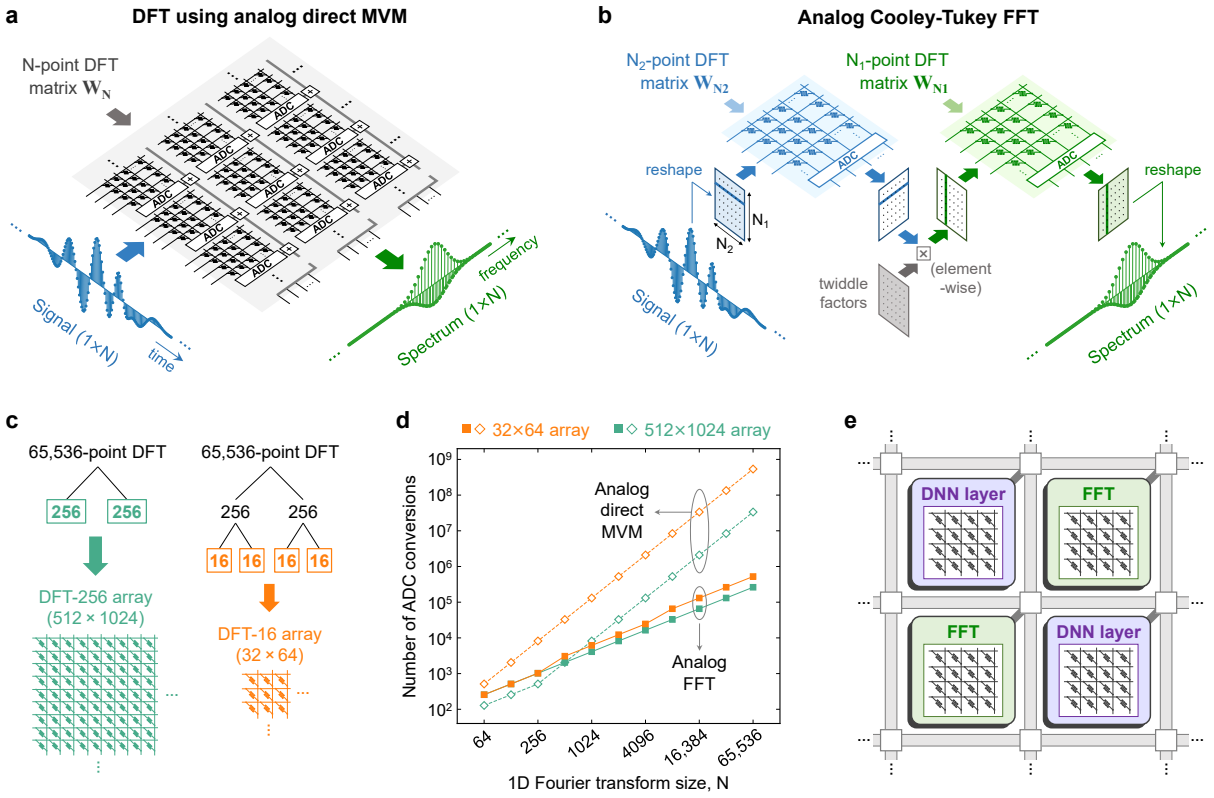

Fig. 1 Processing large Fourier transforms using analog in-memory computing. (a) The direct MVM approach requires a large DFT matrix to be split across many arrays. (b) The analog Cooley-Tukey FFT factorizes the N-point DFT into smaller DFTs of size N_1 and N_2. Only the real part of the temporal signal and frequency spectrum are shown for simplicity. (c) Two of many ways to factorize a 65,536-point DFT using the analog FFT. The leaves of the trees are elementary DFTs mapped to analog MVMs, and the branches are Cooley-Tukey factorizations. (d) Comparison of how the number of ADC conversions scales with DFT size for the analog direct MVM and the analog FFT. We consider analog IMC systems with a maximum single-array DFT size of 16 points (32×64 array size), and 256 points (512×1024 array size). (e) A mesh fabric of analog IMC cores can accelerate a diverse range of workloads. The same cores for processing FFTs can be reprogrammed to execute DNN layers and other kernels.

500× larger than any prior DFT computed using analog hardware [28]. We also show using experimentally-validated models that analog IMC hardware can provide accurate end-to-end acceleration of complex edge workloads such as automatic speech recognition, which combine FFTs with ML processing.

2. The analog fast Fourier transform

Analog in-memory computing systems and digital processors are governed by fundamentally different scaling laws for their energy consumption. The energy associated with digital processing generally scales with the number of arithmetic operations such as multiplies and adds. Analog IMC systems follow a different scaling law, due to an essential characteristic of these architectures: though the matrix computations inside the memory array are extremely efficient, almost all the energy is consumed by peripheral circuits, particularly those involved in sensing and converting analog summed currents to digital outputs with 8-bit or similar resolution [12, 17, 34–36]. Therefore, the total number of conversions by the analog-to-digital converter (ADC) is a useful measure that generally scales together with the total energy consumption, independent of the specific memory technology or circuit implementation.

Beyond its importance for signal processing, the discrete Fourier transform epitomizes the different ways that the two hardware paradigms can scale. The DFT converts a signal $\mathbf{x}$ with length N to its frequency spectrum $\mathbf{X}$:

$$X_k = \sum_{n=0}^{N-1} x_n e^{-i2\pi nk/N} \tag{1}$$

This equation can be explicitly written as a complex-valued MVM: $\mathbf{X} = \mathbf{W}_N\mathbf{x}$, where $\mathbf{W}_N$ is the N-point DFT matrix of size $N \times N$. The element at the (n, k) position of this matrix has the value $(\omega_N)^{nk}$, where $\omega_N = e^{-i2\pi/N}$.

In digital hardware, the DFT is generally computed using an FFT algorithm. The FFT exploits divide-and-conquer techniques to compute the DFT using far fewer operations than by computing the above MVM directly. This fundamentally reduces the DFT's computational complexity, and hence its energy scaling, from $\mathcal{O}(N^2)$ to $\mathcal{O}(N\log_2 N)$ [22]. The reduction is possible by exploiting the symmetries of the DFT matrix. For matrices without symmetry or periodicity, such as matrices of deep neural network (DNN) weights, the number of operations is irreducible without the use of approximations.

The conventional analog IMC approach to the DFT is to program the real and imaginary parts of the matrix $\mathbf{W}_N$ onto a resistive memory crossbar, then compute Equation 1 directly as an analog MVM [23, 24, 26, 37]. When the DFT is computed directly using a single array, the energy scales with the number of outputs of a DFT, which is $\mathcal{O}(N)$. However, this result holds only for small N. As N becomes large, the matrix $\mathbf{W}_N$ eventually exceeds the maximum size of a memory array. There are many factors that constrain the physical size of resistive crossbars, including the maximum current supported by the peripheral circuitry [17], parasitic IR voltage drops along the array interconnects [38], accumulation of memory device conductance errors and noise [39], write disturb [40], and process yield considerations. In this regime, the direct MVM approach requires a large DFT matrix to be split across many physical arrays, with each array producing partial results that are digitized then added, as shown in Fig. 1a. The number of ADC conversions needed to produce a single element of $\mathbf{X}$ scales as $\mathcal{O}(N)$, leading to a total DFT energy scaling of $\mathcal{O}(N^2)$. The area also scales as $\mathcal{O}(N^2)$, regardless of whether it is dominated by the peripheral circuits or the memory array. The rapid, quadratic growth of energy and area with N limits the size and nature of problems that can be processed efficiently with this approach using analog hardware.

We show that analog IMC hardware can overcome this limit by implementing the FFT algorithm and inheriting its fundamental scalability advantages. Specifically, we use Cooley and Tukey's original two-factor FFT algorithm to compute any DFT whose length is a composite number: $N = N_1 \times N_2$ [22, 33]. The input $\mathbf{x}$ and output $\mathbf{X}$, which are vectors of length N, can be reshaped into 2D matrices with dimensions $N_1 \times N_2$: we call these $\tilde{\mathbf{x}}$ and $\tilde{\mathbf{X}}$, respectively. The indices of the new matrices are related to those of the original vectors by $\tilde{x}_{n_1,n_2} = x_{n_1+N_1 n_2}$ and $\tilde{X}_{k_1,k_2} = X_{N_2 k_1+k_2}$. By exploiting the periodicity of $\mathbf{W}_N$, Equation 1 can be re-written as:

$$\tilde{X}_{k_1,k_2} = \sum_{n_1=0}^{N_1-1} \omega_{N_1}^{n_1 k_1} \omega_N^{n_1 k_2} \sum_{n_2=0}^{N_2-1} \omega_{N_2}^{n_2 k_2} \tilde{x}_{n_1,n_2} \tag{2}$$

To explicitly show the mapping onto analog hardware, this equation can be cast in matrix form as:

$$\tilde{\mathbf{X}} = (\mathbf{W}_{N_1} [\mathbf{T} \odot (\mathbf{W}_{N_2}\tilde{\mathbf{x}})]^{\mathrm{T}})^{\mathrm{T}} \tag{3}$$

where $\odot$ is the element-wise product and $\mathbf{T}$ is an $N_1 \times N_2$ matrix of twiddle factors defined by $\mathbf{T}_{mn} = (\omega_N)^{mn}$. Fig. 1b shows a sequence of steps that implement the analog FFT in Equation 3. In the first stage, an N_2-point DFT is computed for every row of the matrix $\tilde{\mathbf{x}}$ using a sequence of analog MVMs on a resistive memory array, which execute the matrix-matrix multiplication $\mathbf{W}_{N_2}\tilde{\mathbf{x}}$. The results are digitized and multiplied element-wise with the twiddle matrix $\mathbf{T}$ using digital multipliers. Next, a second stage of N_1-point DFTs is executed to perform the multiplication with $\mathbf{W}_{N_1}$, again via a sequence of analog MVMs. Finally, the result $\tilde{\mathbf{X}}$ is reshaped back into a vector to obtain $\mathbf{X}$. This Cooley-Tukey decomposition enables a large N-point DFT, which otherwise needs to be split across many arrays, to be computed with just two arrays that implement an N_1-point analog DFT and an N_2-point analog DFT, respectively. Alternatively, the analog MVMs that make up the two stages of the FFT can be executed in parallel on multiple arrays, as shown in Fig. S1. This enables the analog FFT to match the throughput of the direct MVM, while still requiring much less total area for the analog cores. This parallel scheme further enables the twiddle multiplications to be folded into the analog MVMs, eliminating the need for any digital multiplications (see Supplementary Section 1).

To scale to a DFT size N that is much larger than the array size, the Cooley-Tukey factorization can be applied recursively to further reduce the elementary DFT sizes, or radices, as shown in Fig. 1c. The physical size of the memory array sets the upper bound on the size K of an elementary analog DFT; to compute a K-point complex DFT using one MVM in a single array, the array needs to have at least $2K$ rows and $4K$ columns [23]. Large inverse DFTs (IDFTs) can be similarly decomposed by Cooley-Tukey

factorization onto smaller analog IDFTs, since the IDFT matrix is simply the conjugate transpose of $\mathbf{W}_N$ and has the same symmetries.

Fig. 1d compares how the number of required ADC conversions scales between the two analog DFT approaches, considering both a small array ($K = 16$) and a large array ($K = 256$). The latter corresponds to the largest analog MVM that can be executed by the SONOS array used in this work, and also matches the array size of other large analog IMC prototypes [19]. For the direct MVM method, the array's dimensions set the critical DFT size where the scaling law transitions from $O(N)$ to $O(N^2)$. For the analog FFT, if the Cooley-Tukey decomposition is only applied once, i.e. $N \leq K^2$, the total number of ADC conversions in the analog FFT scales as $\mathcal{O}(N)$. When the DFT is recursively factorized, all of these operations increase proportionally with the number of Cooley-Tukey decompositions, which scales as $\mathcal{O}(\log_K N)$. Combining these two trends, the energy of the analog FFT scales as $\mathcal{O}(N\log_K N)$ in the limit of large N. The worst-case area overhead of the parallel analog FFT also scales as $\mathcal{O}(N\log_K N)$, as explained in Supplementary Section 12. Therefore, both the energy and area scaling laws are superior to the $\mathcal{O}(N^2)$ scaling of the direct MVM approach. In general, the DFT size where the analog FFT and direct MVM have similar efficiency is $N = 2K$. Above this, the FFT approach is increasingly more efficient due to its more favorable scaling, leading to orders-of-magnitude lower energy consumption and area for large DFT sizes.

The overall $\mathcal{O}(N\log N)$ scaling of the analog FFT is similar to that of the digital FFT, but there are essential differences in the algorithmic structure. In digital FFT implementations, recursively decomposing the DFT down to the smallest possible elementary DFTs (i.e. radix-2 or radix-4) optimally reduces the complexity from $\mathcal{O}(N^2)$ to $\mathcal{O}(N\log_2 N)$ [22]. Meanwhile, for analog FFTs, it is more optimal from an energy standpoint to minimize the depth of the Cooley-Tukey factorization tree by terminating the decomposition as soon as the factored DFT is small enough to fit onto one memory array. Further factorization would decrease the total number of arithmetic operations, which is helpful for digital systems, but would increase the number of intermediate DFT results and hence the number of ADC conversions, which is harmful for analog systems (see Fig. S10b). This explains why having a larger physical array size is more energy-efficient for large analog FFTs, as shown in Fig. 1d. However, because of the $\mathcal{O}(N\log_K N)$ scaling of the analog FFT, small arrays (small K) can also scale to large FFTs with only a modest energy penalty compared to large arrays. A similar divide-and-conquer approach can be used to compute DCTs in analog hardware with $\mathcal{O}(N\log_K N)$ energy and area scaling, by using a fast DCT algorithm that decomposes the DCT into arbitrary composite factors [41], then programming the factored DCT matrices onto resistive crossbars.

Analog FFT processors can be rapidly reconfigured to compute DFTs of various sizes without re-programming any memory devices. This is possible due to the symmetries in the DFT matrix. A memory array that has been programmed with a K-point DFT matrix can be re-used to compute a smaller DFT of size $K/(a \times b)$ simply by applying inputs to every a^{th} row and measuring the outputs from every b^{th} column. This reconfigurability can be used to dynamically change the FFT radix or to switch to direct MVM mode (for small DFTs), and this usage is experimentally demonstrated on an audio FFT example in Supplementary Section 5. The flexibility to support multiple FFT sizes is valuable for applications such as wireless communications, where it is often desirable to switch on the fly between different channel bandwidths or standards [42, 43]. More broadly, the reconfigurability of analog arrays enables a highly flexible accelerator architecture, shown in Fig. 1e, where each analog IMC core within the fabric can be programmed to implement variable-length FFTs, DNN layers, finite impulse response filters [27], linear equation solvers [37], and other linear algebra kernels. The versatility of the analog IMC core allows the architecture to efficiently process workloads that otherwise would have required the combination of multiple specialized digital or analog processors.

3. Analog DFTs using SONOS charge-trapping memory

To execute analog FFTs, we used an array of SONOS charge-trapping memory devices that have stable and precisely programmable analog conductance levels. The state variable of SONOS memory is the amount of charge that is confined in a silicon nitride charge-trapping layer, which modulates the electronic conductance of the underlying silicon channel through the field effect. A 1024×1024 crossbar array of SONOS devices was fabricated in a 40-nm CMOS process that uses the compact two-transistor (2T) memory cell shown in Fig. 2a. The array was integrated with peripheral CMOS circuits to support analog MVMs and write-verify programming of each SONOS device to a target conductance. To minimize conductance change over time, the programming procedure selectively places charge in mid-gap electronic traps in the nitride layer that have large energy barriers for escape [44–46]. We operate the SONOS

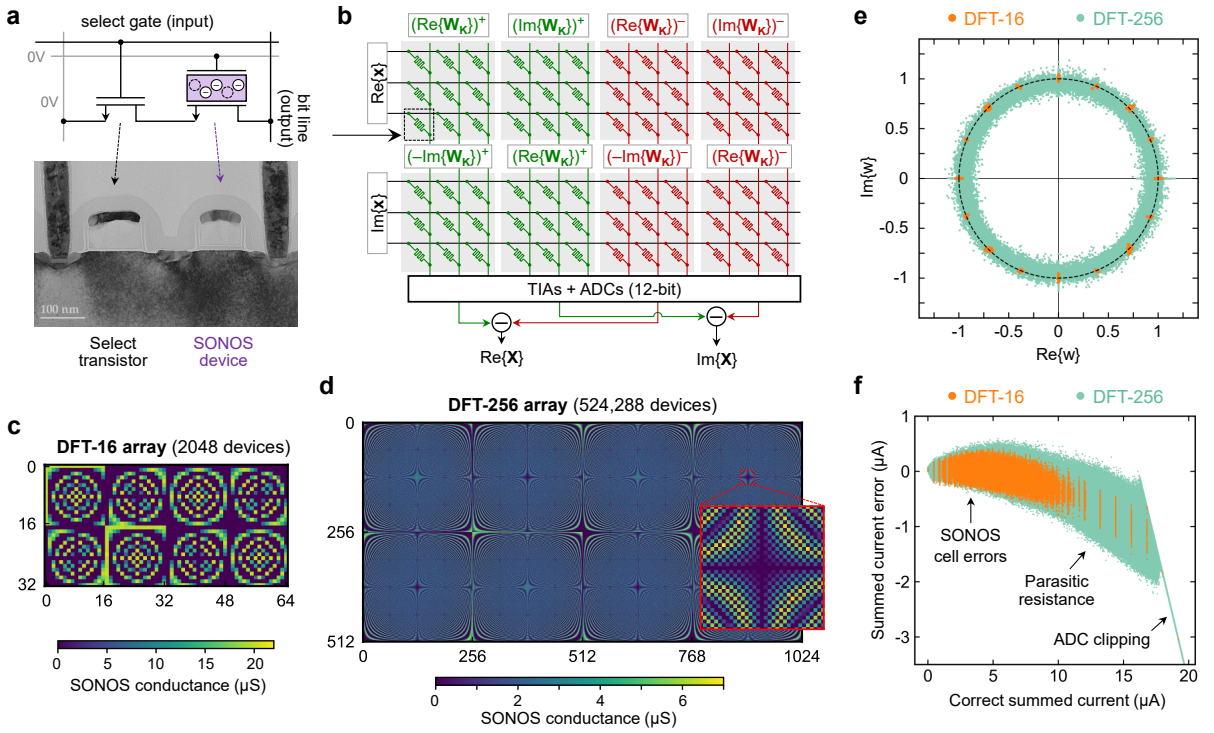

Fig. 2 DFT mapping onto a SONOS charge-trapping memory array. (a) Electrical schematic (top) and transmission electron microscope image (bottom) of the two-transistor SONOS memory cell. (b) Mapping a DFT operation with complex-valued weights and inputs to a resistive memory crossbar. The SONOS cell with the input-output connections in (a) is simplified in this schematic to a resistor. (c) Measured SONOS conductance profile for a DFT-16 matrix. (d) Measured SONOS conductance profile for a DFT-256 matrix. Inset shows a 32×32 region of the programmed array. (e) Constellation of the complex-valued DFT weight values stored in the programmed SONOS devices, for DFT-16 and DFT-256. The ideal DFT weights lie along the unit circle (black dashed circle). (f) Accuracy of individual current-mode analog MVMs for 16-point and 256-point DFTs, showing the dominant sources of error in different current regimes. Data on more than 3.7×10^7 analog current sums are collected from processing the audio signal in Fig. 3.

transistors primarily in the subthreshold region, where the device has a large conductance On/Off ratio ($>10^6$) and errors that approach zero at low conductance [45]. The statistically characterized, state-dependent device-to-device variation and drift in the programmed SONOS conductances are quantified in Fig. S5e and S5f.

The analog DFT mapping in Fig. 2b is used to multiply a complex-valued DFT weight matrix with a complex-valued vector [23]. The difference in conductance of two SONOS devices encodes the signed value of each real or imaginary weight. To execute a DFT, the input vector $\mathbf{x}$ is applied bit-serially to the select gate lines, and each selected SONOS cell draws a current from its bit line (BL) that is proportional to its conductance. On this chip, the analog sum of currents collected on the BL is converted to a voltage by a transimpedance amplifier (TIA), then to digital outputs using an ADC [46]. Digital post-processing accumulates the analog MVM results for different input bits and produces the complex-valued DFT output $\mathbf{X}$ (see Methods). The on-chip ADC has a resolution of 12 bits over the range from 0 to 17 μA.

Fig. 2c and Fig. 2d show the measured conductance profiles of a portion of the SONOS array after programming a DFT-16 matrix and a DFT-256 matrix, respectively. A maximum target SONOS conductance of 20 μS was used for the DFT-16 subarray, while the DFT-256 subarray used a reduced maximum conductance of 6.2 μS to ensure that most of the summed currents in our exemplar applications (described below) do not exceed the ADC's limits. Fig. 2e shows the locations in the complex plane of the DFT weights that were programmed onto the SONOS array, whose ideal values ($e^{i2\pi nk/K}$) would lie perfectly along the unit circle. In general, the SONOS-encoded DFT weights are tightly distributed around the circle; the DFT-16 weights have a mean absolute error of $\epsilon_{|\omega|} = 0.0118$ in magnitude and $\epsilon_{\angle\omega} = 0.338°$ in phase. The DFT-256 weights have somewhat larger errors: $\epsilon_{|\omega|} = 0.0458$ and $\epsilon_{\angle\omega} = 1.037°$. This is because the smaller conductances used for the DFT-256 matrix led to a smaller ratio between the signal and error components of the conductance, and a larger amount of conductance drift caused a systematic reduction in the weight magnitudes. Conductance statistics for DFT arrays of various sizes can be found in Supplementary Section 4. Notably, large DFT matrices have values that are distributed approximately

uniformly over the conductance range; this differs dramatically from DNN weight matrices, which generally have an abundance of near-zero weights and are exponentially skewed toward low conductance [39, 45]. This implies that for the same array size, analog DFT operations will accumulate larger currents, and potentially larger errors, than the typical MVM operations used for DNN inference.

To illustrate the sources of error in the SONOS-based analog DFTs, Fig. 2f shows the error statistics of the analog current sums (representing dot products) across a large number of 16-point and 256-point elementary DFT computations, performed as part of the audio processing FFT experiments in the next section. There are three main sources of error, which dominate at different regimes of the summed current. For small summed currents, the error is random and zero-centered, and originates from the accumulated random variability and noise in the conductances of the SONOS devices, as described above. At intermediate to large summed currents, the error is dominated by parasitic IR drops across the resistances of the array's rows and columns, which cause a systematic reduction in current [38]. This effect is more pronounced for the 256-point analog DFTs due to the much larger MVM size (512×1024), while the 16-point DFTs have much lower summed currents on average, and hence has negligible IR drops. Finally, for the largest outlier currents in Fig. 2f, the ADC clips the current measurement to the limit of 17 µA, leading to a negative error that increases linearly with the correct current value.

4. Audio processing using analog FFTs

To experimentally demonstrate the analog Cooley-Tukey FFT and evaluate its accuracy, we used the SONOS array as a spectrum analyzer for audio waveforms. A useful representation of the spectrum of a signal is the spectrogram, which shows how the signal's frequency spectrum changes with time [47]. This is generated using a short-time Fourier transform (STFT), which computes the DFT over temporal sliding windows of the signal. The magnitude squared of the complex-valued STFT output yields the power spectrum for each time window, and these spectra are stacked in time to produce the final spectrogram. For this experiment, we used a four-second audio waveform from the Flickr8k Audio Caption dataset [48], with slight zero-padding to 65,536 samples (4.096 seconds at 16 kHz sampling rate). The waveform is shown in Fig. 3a and contains the spoken caption, "Two dogs reach for a yellow frisbee as it flies through the air." Fig. 3b shows the spectrogram of this signal on a logarithmic scale, computed using a digital STFT at single-precision floating-point (FP32) on a CPU. We used Hamming windows with 512 samples (i.e. uses 512-point FFTs), with 75% overlap between windows, which are typical parameters for processing speech waveforms. Fig. 3c shows the spectrogram generated experimentally using an analog STFT, where each 512-point FFT was decomposed into 32-point and 16-point DFTs ($N_1 = 32$, $N_2 = 16$) that were computed using the SONOS array.

The SONOS-computed spectrogram reproduces all of the key features of the FP32 spectrogram and resolves the frequency signature of each spoken word. In this experiment, we are able to compute frequency components that span several orders of magnitude in dynamic range, because each component was accumulated over 12 bits of the input signal using digital shift-and-add operations. The peak signal-to-noise ratio (PSNR), which measures the element-wise error between the two spectrograms, is 56.99 dB. There are somewhat subtle differences between the spectrograms, mainly visible as the presence of background noise in some parts of the SONOS spectrogram, which originates from device-to-device variability and cycle-to-cycle read noise in the SONOS conductances, accumulated over many devices in an analog MVM. As another assessment of the spectrogram's quality, we reconstructed the four-second audio waveform by digitally computing the inverse FFT (IFFT) on the SONOS-computed complex-valued spectrum of each sliding window. Both the original and reconstructed audio files are provided as Supplementary Information. Each spoken word is clearly reproduced in the reconstructed audio clip, with a nearly imperceptible difference compared to the original audio.

To demonstrate the scalability of the analog FFT, we use the SONOS array to compute a 65,536-point FFT, sufficient to generate the spectrum of the full audio waveform in Fig. 3a without breaking it up into sliding windows. The 65,536-point analog FFT is computed by factoring it into 256-point analog DFTs (i.e. $N_1 = N_2 = 256$) that were executed on the SONOS subarray in Fig. 2d. We note that a transform size of 65,536 points is far too large to be feasibly implemented in analog without the Cooley-Tukey FFT; if using a direct MVM approach, the partitioned collection of arrays would need to have 3.4×10^{10} memory devices in total. The power spectrum of the audio waveform as computed experimentally by the SONOS array is shown in Fig. 3d, alongside the true spectrum computed at FP32 precision. The large size of the FFT yields a fine frequency resolution of 0.244 Hz. The left inset zooms into the frequency range of female human speech (∼165 to 255 Hz [49]), showing close point-by-point agreement between the SONOS and FP32 computations. Across the full range of frequencies, the SONOS-computed spectrum

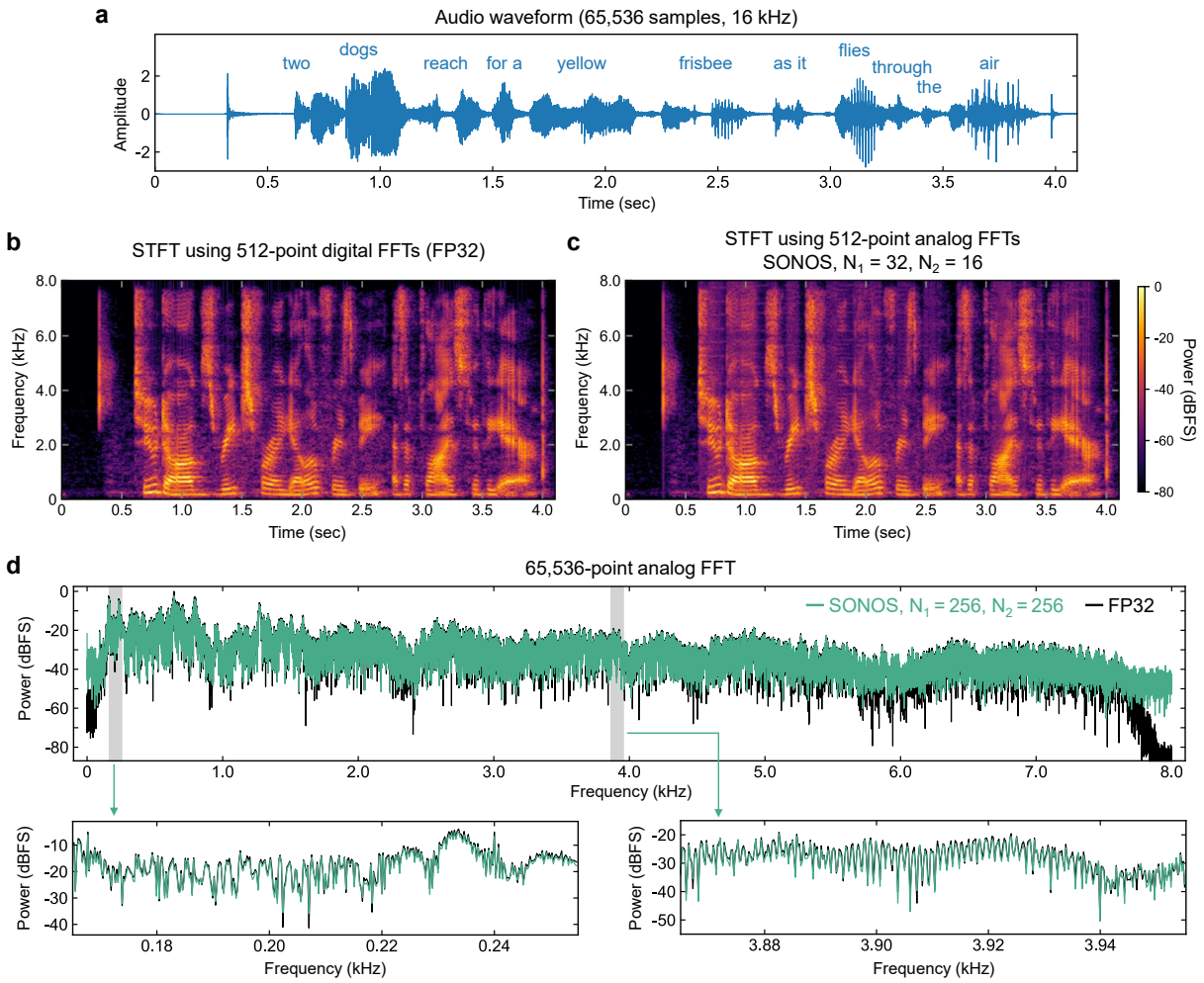

Fig. 3 Audio processing with analog FFTs. (a) Speech audio waveform with 65,536 samples. (b) Spectrogram of the audio waveform generated by FP32 STFTs, using a window size of 512 samples, a hop length of 128 samples, and a Hamming window function. The frequency resolution is 31.25 Hz. (c) Spectrogram generated experimentally using STFTs that are implemented with 512-point analog FFTs. The FFTs are factored into 32-point and 16-point analog DFTs that are executed on the SONOS array. (d) Power spectrum of the full audio waveform, computed by a 65,536-point analog FFT using the SONOS array (teal), compared to an FP32 digital FFT (black). The analog FFT was factored into 256-point analog DFTs that are executed on the SONOS array. Insets zoom in on two parts of the spectrum. The frequency resolution is 0.244 Hz. dBFS: decibels relative to full-scale.

has a PSNR of 41.10 dB relative to FP32. The slightly lower PSNR compared to the STFT is due to the use of significantly larger elementary DFTs, which have larger analog MVM errors as shown in Fig. 2e. Additionally, we used both the magnitude and phase of the SONOS-computed spectrum to reconstruct the audio waveform via a single IFFT. The reconstructed audio clearly reproduces the spoken message (see Supplementary Information).

5. Image processing using the analog vector-radix FFT

For image processing applications, analog approaches to the DFT must be extended to two dimensions. The DFT of a two-dimensional $M \times N$ input $\mathbf{x}$ can be computed with two matrix-matrix multiplications:

$$\mathbf{X} = [\mathbf{W}_N(\mathbf{W}_M\mathbf{x})^{\mathrm{T}}]^{\mathrm{T}} \tag{4}$$

Using resistive memory arrays, a direct MVM approach to computing the above expression involves a sequence of N analog MVMs (M-point DFTs) followed by M analog MVMs (N-point DFTs). Considering the case of $N \times N$ square-shaped 2D DFTs for simplicity, the energy of this approach scales as $\mathcal{O}(N^3)$ due to the need to partition the MVMs across many memory arrays when N is large.

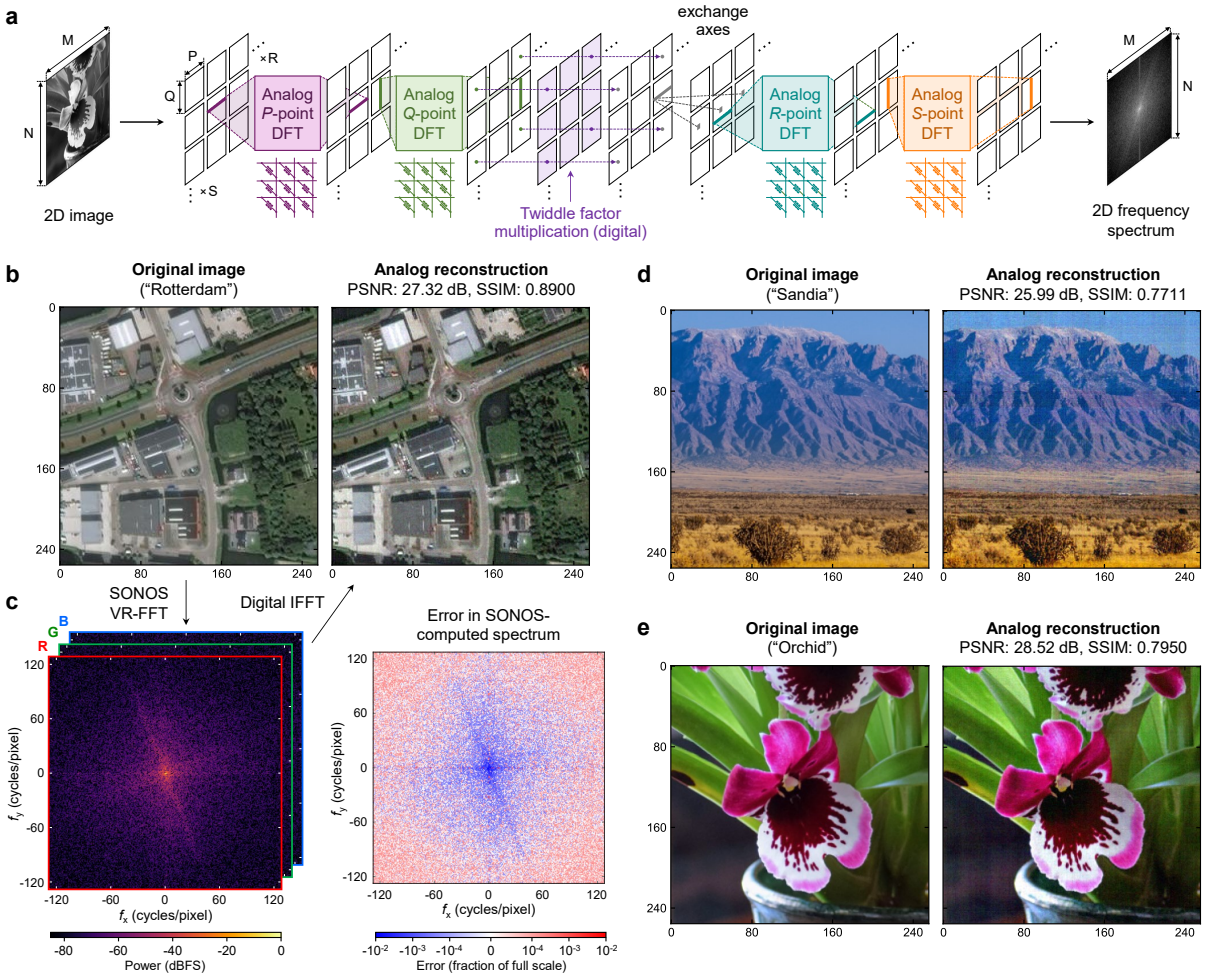

Fig. 4 Analog vector-radix FFT for 2D image processing. (a) Diagram of the analog 2D ($M \times N$) VR-FFT, which is composed of several analog DFT stages of smaller size. (b) Comparison of (left) a 256 × 256 input image with (right) the analog reconstruction of the same image. The input is a satellite overhead image of Rotterdam from the SpaceNet-6 dataset [50]. The analog reconstruction is obtained by experimentally computing the analog VR-FFT of the image using the SONOS array (with $P = Q = R = S = 16$), followed by an ideal digital IFFT. (c) 2D magnitude spectrum of the image in (b), computed using the SONOS array, showing one of three color channels. The right side shows the color-averaged error of the magnitude spectrum relative to that calculated by a 2D FFT at FP32 precision. (d-e), Original vs experimental analog reconstruction for two other 256 × 256 images. ("Orchid" photograph was taken by the author. "Sandia" photograph from Dorothy Harris, Wikimedia Commons, CC-BY-2.0 license.)

By applying the Cooley-Tukey decomposition to both dimensions together, the computational complexity of the 2D DFT can be reduced dramatically. This multi-dimensional generalization of the Cooley-Tukey FFT is the vector-radix FFT (VR-FFT) [51, 52], and its mapping onto analog in-memory computing is illustrated in Fig. 4a for the 2D case. In this scheme, each dimension of the input is factored: $M = P \times R$ and $N = Q \times S$. The factors P, Q, R, and S are the sizes of the elementary analog DFTs, which are performed sequentially on the entire image in four stages with one element-wise twiddle multiplication step after the second stage. For very large images, these smaller DFTs can be recursively decomposed. The mathematical details of the analog VR-FFT are described in the Methods. If we again consider an $N \times N$ input, the energy of the analog 2D VR-FFT scales as $\mathcal{O}(N^2 \log_K N)$, which is significantly more efficient than the analog direct MVM approach for large N, and is fundamentally similar to the $\mathcal{O}(N^2 \log_2 N)$ energy scaling of digital 2D FFT implementations [22].

We used the analog VR-FFT to experimentally compute the spectrum of spatial frequencies in 2D images, utilizing a SONOS subarray that is much smaller than the image size. We selected exemplar RGB images, shown in Fig. 4b, 4d, and 4e, which contain satellite aerial imagery and natural scenes. For the VR-FFT, we decomposed each 256×256 FFT with the factors $P = Q = R = S = 16$, which allows all of the analog DFT steps to be computed by a single SONOS subarray programmed to the DFT-16 matrix. Each color channel was processed independently. Fig. 4c (left) shows the magnitude spectrum of the 2D spatial frequencies for the red channel of the "Rotterdam" image as computed by the SONOS array. The

magnitude is largest for low spatial frequencies near zero, and for frequencies that lie along a diagonal through the origin. This diagonal corresponds to the angle of a straight road that spans the entire width of the "Rotterdam" image.

To evaluate the fidelity of analog image processing, we used both the magnitude and phase of the SONOS-computed frequency spectrum to reconstruct the original image, via FP32 2D IFFTs on a digital processor. We note that unlike prior experiments that tiled smaller reconstructions into a larger image [24], our reconstructions are based on the SONOS-computed spectrum of entire 256×256 images. These are shown on the right side of Fig. 4b, 4d, and 4e. To roughly compensate for signal loss caused by parasitic IR drops, the images were uniformly brightened using a scaling factor based on Parseval's theorem for Fourier transforms, as described in Supplementary Section 8. In general, the SONOS VR-FFT preserves the spatial features in these images without introducing significant artifacts, though there is slight graininess caused by random analog conductance errors and circuit noise. Close inspection of the analog reconstructions also reveals that the edges are sharper compared to the original images (especially "Rotterdam"). This effect is caused by parasitic IR drops, which contribute negative MVM errors that grow with the summed current as shown in Fig. 2f, and therefore leads to a reduction of the strongest components in the frequency spectrum. For these images, the IR drops attenuate the low spatial frequencies, as shown in Fig. 4c (right), resulting in an image sharpening effect in the reconstruction.

We report in Fig. 4 two similarity metrics between the original and analog reconstructed image: the PSNR, which measures pixel-wise errors, and the structural similarity index measure (SSIM), which evaluates statistical and structural differences between images [53]. All three reconstructed images have similarly high values of PSNR $>$ 25 dB, but the SSIM has a greater variance, likely due to the metric's sensitivity to the presence of high-contrast edges [54]. We also experimentally computed the 2D frequency spectra of the "Rotterdam" image at several scales, using both the analog FFT and the analog direct MVM. Compared to analog FFTs, the reconstructed images using direct MVMs had lower quality metrics due to a greater amount of error accumulation in large arrays, as shown in Supplementary Section 9.

6. Scalability, performance, and efficiency

We now use simulations to assess the scalability of the analog FFT on more practical, larger-scale FFT workloads. We have validated that our accuracy model (described in Methods), when configured to simulate the properties of the fabricated SONOS test chip, produces results that closely match our experimental data, as shown in Fig. S16. For the results in this section, we modify this accuracy model to simulate a more energy-efficient analog IMC core than our fabricated prototype, but retain the same error models for the SONOS devices and parasitic IR drops. This more efficient core, whose operation is described more fully in Supplementary Section 11, uses 8-bit ADCs and performs subtraction and input bit accumulation in the analog domain.

We first evaluate how the accuracy of the analog 2D VR-FFT scales to a real application with large transform sizes, by applying it to an image formation algorithm for synthetic aperture radar (SAR), shown in Fig. 5a. We use raw phase history data from a SAR sensor and an implementation of the widely used polar-format image formation algorithm, both of which are publicly available [62]. SAR systems use chirped pulses to sample information about the imaged scene in the spatial frequency domain. The polar-format algorithm first interpolates this complex-valued data onto a rectangular grid in frequency space, then uses a 2D DFT to form an image along the axes that are perpendicular (range) and parallel (azimuth) to the sensor's flight path [2]. Fig. 5a shows the formed aerial SAR images, where the 2048×2048 DFT was computed both using an FP32 FFT (left) and using the analog VR-FFT on a simulated SONOS IMC core (right), where 8-bit inputs and 8-bit ADCs were used in all four stages. Even at this large transform size, the analog VR-FFT is able to maintain high fidelity (SSIM $>$ 85%) and preserve all the salient features in the SAR image.

Next, we assess the quality of the analog FFT when its results are used for complex downstream workloads. For this purpose, we simulate the end-to-end automatic speech recognition (ASR) pipeline in Fig. 5b. Raw audio waveforms are first pre-processed with STFTs using 512-point FFTs as in our audio processing experiment, then the resulting spectrograms are passed into a large recurrent neural network transducer (RNNT) model that outputs the predicted text transcription [63]. We select the pre-trained RNNT model from the MLPerf Inference Benchmark [64] and evaluate the word error rate (WER) of the transcription on the Librispeech test dataset [65]. Using the model for the efficient SONOS-based analog MVM core described above, we simulate two scenarios: analog processing of the STFTs only, and analog processing of both the STFTs and all of the long-short term memory (LSTM) and fully-connected (FC) layers in RNNT, which collectively have 45.3 million weights. These layers are mapped

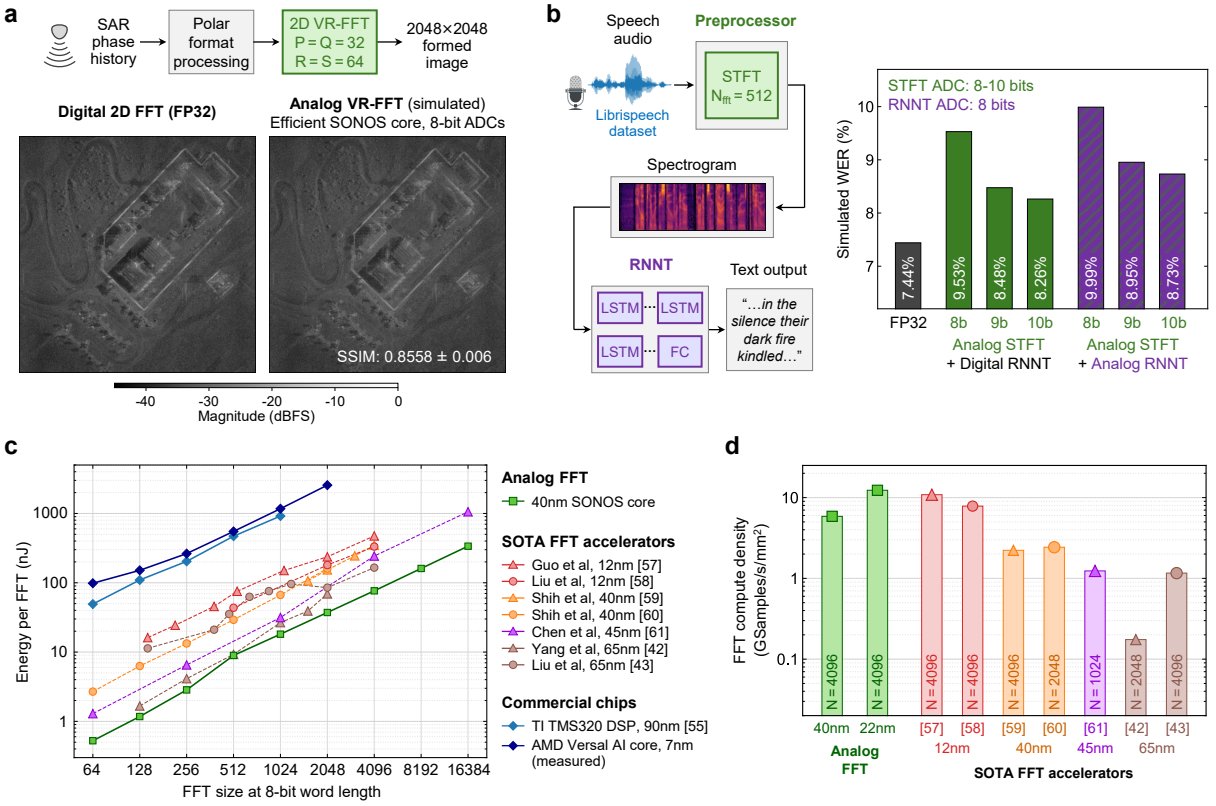

Fig. 5 Simulated accuracy, energy, and performance scaling of analog Fourier transforms. (a) Formation of a 2048×2048 range-azimuth image from raw SAR phase history data, using an analog VR-FFT as part of the polar format algorithm. The SSIM of the simulated image using analog FFTs (right) is computed relative to the formed image using a 2D FFT at FP32 precision (left). The mean and standard deviation of the SSIM is reported, from ten Monte Carlo accuracy simulations of an optimized 40-nm SONOS core with 8-bit ADCs. (b) Automatic speech recognition using 512-point analog FFTs for spectrogram generation and analog MVMs to accelerate the RNNT speech-to-text neural network. The simulated WER on the Librispeech "test-clean" dataset (2620 audio samples) is reported, where SONOS-based analog MVMs are used for STFT only, and for both STFT and RNNT. The ADC resolution for the analog STFT is varied from 8 to 10 bits, while for all RNNT layers it is fixed at 8 bits. (c) Comparison of the FFT energy vs 1D FFT size for a SONOS-based analog FFT, commercial chips that can process DSP workloads [55, 56], and various state-of-the-art (SOTA) digital FFT processors from the literature that support a flexible FFT size [42, 43, 57–61]. For the analog FFT, the ADC resolution is 8 bits and the maximum array size is 1024×1024 (one array can process up to a 256-point DFT). (d) Comparison of the FFT compute density, quantified as the throughput normalized by chip area, between the SONOS-based analog FFT core and specialized digital FFT processors. The analog FFT was evaluated for a 4096-point FFT. The other processors were evaluated at their individual maximum supported FFT size that can fit onto one chip.

to analog in-memory computing arrays in a similar manner as demonstrated in Ref. 19. We find that when spectrograms are generated by analog STFTs with 8-bit ADCs, the WER increases by ∼2% relative to a fully FP32 baseline, but this difference decreases to ∼1% when using 9-bit ADCs, which provide slightly higher precision and dynamic range in the spectral coefficients. The WER saturates for an ADC resolution higher than 9 bits, as the SONOS conductance errors become the bottleneck for MVM precision. Meanwhile, we find that 8-bit ADC precision provides sufficient accuracy for the RNNT layers, and that combining analog STFTs with analog RNNT processing only marginally increases the WER. This demonstrates that a fabric like that of Fig. 1e, where highly efficient analog MVM cores can be used flexibly as ML or DSP engines, can yield accurate results for commercially relevant edge applications.

In Fig. 5c, we compare the energy efficiency of the 40-nm-SONOS based analog FFT to state-of-the-art designs from the literature for specialized FFT processors, as well as two commercial chips with DSP cores. The digital FFT accelerators, which are not matrix multiplication engines, implement a variety of architectures and algorithms to optimally compute the FFT. Since these FFT implementations use varying numbers of operations, their efficiency is not well captured by the TOPS/W (TeraOperations/s/Watt) metric typically used for ML processors. We also compare the area-normalized performance of these FFT processors in Fig. 5d. For the analog FFT, we focus on the 8-bit ADC design, which is close to the analog error dominated regime as described above. To ensure an iso-precision comparison, we linearly scaled both the energy efficiency and compute density of all the digital FFT processors from their original FFT

word length to 8 bits [57]. For the analog implementation, Cooley-Tukey decomposition is used only for DFT sizes larger than 256. See Supplementary Section 11 for details on the analog IMC core's parallelized and pipelined operation, and the projections for its energy, area, and performance.

Across a wide range of practical FFT sizes, the analog FFT processor can achieve a higher energy efficiency than the most efficient digital ASICs for the FFT. It also provides higher FFT throughput per area than the digital FFT ASICs at a comparable process node. When implemented using a more scaled 22-nm SONOS memory technology [46], the analog FFT can deliver higher performance per area than a digital FFT ASIC design in a 12-nm node, as shown in Fig. 5d. While significant, we note that these are not orders-of-magnitude improvements because, as described earlier, the low-radix digital FFTs and the high-radix analog FFTs offer distinct, mutually exclusive paths to high efficiency and performance: the first leads to a greater reduction in operation count, while the second drastically reduces the energy per operation.

The key unique advantage of the analog FFT is that it delivers best-in-class efficiency and performance while being far more flexible than digital ASICs that are heavily optimized for the FFT: the same analog arrays can be re-programmed as matrix multiplication engines for ML algorithms that can deliver up to 255 TOPS/W of energy efficiency (depending on the matrix size, see Fig. S24). The analog core can also be re-programmed to efficiently implement other linear transforms that are useful in edge signal processing, such as the DCT, Chirp-Z transform, discrete wavelet transform, and interpolation – some of which can be processed using divide-and-conquer techniques similar to the analog FFT. When compared to the AMD Versal, which is also a flexible processor for AI and DSP workloads, the analog IMC core can execute FFTs at >60× higher efficiency, and matrix multiplications at >65× higher efficiency, for typical DNN matrices that have more than 256 rows. The analog FFT can be realized using any technology for analog IMC, such as memristors [28] or capacitive matrix multiplication engines [66]. Future implementations that can achieve higher TOPS/W or higher compute density for matrix multiplication would also improve the efficiency and throughput-per-area of analog FFTs that are carried out at the same precision.

7. Conclusion

We have shown that the fast Fourier transform can be implemented on analog in-memory computing accelerators, enabling analog systems to scale efficiently and accurately to practically useful DFT sizes that were otherwise inaccessible. By decoupling the full DFT size from the physical array size, we have experimentally demonstrated a 65,536-point analog DFT computed using SONOS memory, which is more than 500× larger than the largest previous demonstration [28]. The analog FFT technique allows the same resistive crossbar array to serve both as an efficient, scalable, and flexible FFT engine, and as an efficient matrix multiplication engine for ML and linear algebra workloads. This versatility can transform the capabilities of edge systems that often need both DSP and ML processing within a low power envelope. A homogeneous fabric of reprogrammable, multi-purpose accelerators would also simplify the hardware design of such systems, while providing superior efficiency and performance to a heterogeneous combination of state-of-the-art digital ASICs. Applying similar principles to other divide-and-conquer algorithms may further expand the versatility of analog in-memory computing hardware beyond its traditional domain of matrix multiplication.

References

[1] Walker, J. L. Range-doppler imaging of rotating objects. *IEEE Transactions on Aerospace and Electronic Systems* **16**, 23–52 (1980).

[2] Jakowatz, C., Wahl, D., Eichel, P., Ghiglia, D. & Thompson, P. *Spotlight-Mode Synthetic Aperture Radar: A Signal Processing Approach* (Springer US, 2012).

[3] Richards, M. A. *et al. Fundamentals of Radar Signal Processing* Vol. 1 (McGraw-Hill New York, 2005).

[4] Sun, S., Petropulu, A. P. & Poor, H. V. MIMO radar for advanced driver-assistance systems and autonomous driving: Advantages and challenges. *IEEE Signal Processing Magazine* **37**, 98–117 (2020).

[5] Amodei, D. *et al.* Deep Speech 2: End-to-end speech recognition in English and mandarin. *International Conference on Machine Learning* 173–182 (2016).

[6] Radford, A. *et al.* Robust speech recognition via large-scale weak supervision. *International Conference on Machine Learning* 28492–28518 (2023).

[7] Hwang, T., Yang, C., Wu, G., Li, S. & Ye Li, G. OFDM and its wireless applications: A survey. *IEEE Transactions on Vehicular Technology* **58**, 1673–1694 (2009).

[8] Cai, Y., Qin, Z., Cui, F., Li, G. Y. & McCann, J. A. Modulation and multiple access for 5G networks. *IEEE Communications Surveys & Tutorials* **20**, 629–646 (2018).

[9] Michailow, N. *et al.* Generalized frequency division multiplexing for 5th generation cellular networks. *IEEE Transactions on Communications* **62**, 3045–3061 (2014).

[10] Hennessy, J. L. & Patterson, D. A. A new golden age for computer architecture. *Communications of the ACM* **62**, 48–60 (2019).

[11] Burr, G. W. *et al.* Neuromorphic computing using non-volatile memory. *Advances in Physics: X* **2**, 89–124 (2017).

[12] Xiao, T. P., Bennett, C. H., Feinberg, B., Agarwal, S. & Marinella, M. J. Analog architectures for neural network acceleration based on non-volatile memory. *Applied Physics Reviews* **7**, 031301 (2020).

[13] Sebastian, A., Le Gallo, M., Khaddam-Aljameh, R. & Eleftheriou, E. Memory devices and applications for in-memory computing. *Nature Nanotechnology* **15**, 529–544 (2020).

[14] Li, C. *et al.* Long short-term memory networks in memristor crossbar arrays. *Nature Machine Intelligence* **1**, 49–57 (2019).

[15] Yao, P. *et al.* Fully hardware-implemented memristor convolutional neural network. *Nature* **577**, 641–646 (2020).

[16] Xue, C.-X. *et al.* A CMOS-integrated compute-in-memory macro based on resistive random-access memory for AI edge devices. *Nature Electronics* **4**, 81–90 (2021).

[17] Wan, W. *et al.* A compute-in-memory chip based on resistive random-access memory. *Nature* **608**, 504–512 (2022).

[18] Huang, Y. *et al.* Memristor-based hardware accelerators for artificial intelligence. *Nature Reviews Electrical Engineering* 1–14 (2024).

[19] Ambrogio, S. *et al.* An analog-AI chip for energy-efficient speech recognition and transcription. *Nature* **620**, 768–775 (2023).

[20] Le Gallo, M. *et al.* A 64-core mixed-signal in-memory compute chip based on phase-change memory for deep neural network inference. *Nature Electronics* **6**, 680–693 (2023).

[21] Fick, L., Skrzyniarz, S., Parikh, M., Henry, M. B. & Fick, D. Analog matrix processor for edge AI real-time video analytics. *IEEE International Solid-State Circuits Conference (ISSCC)* **65**, 260–262 (2022).

[22] Duhamel, P. & Vetterli, M. Fast Fourier transforms: A tutorial review and a state of the art. *Signal Processing* **19**, 259–299 (1990).

[23] Cai, R., Ren, A., Wang, Y. & Yuan, B. Memristor-based discrete Fourier transform for improving performance and energy efficiency. *IEEE Computer Society Annual Symposium on VLSI (ISVLSI)* 643–648 (2016).

[24] Li, C. *et al.* Analogue signal and image processing with large memristor crossbars. *Nature Electronics* **1**, 52–59 (2018).

[25] Hu, M. *et al.* Memristor-based analog computation and neural network classification with a dot product engine. *Advanced Materials* **30**, 1705914 (2018).

[26] Zhao, H. *et al.* Energy-efficient high-fidelity image reconstruction with memristor arrays for medical diagnosis. *Nature Communications* **14**, 2276 (2023).

[27] Huang, Y. *et al.* Radiofrequency signal processing with a memristive system-on-a-chip. *Nature Electronics* 1–10 (2025).

[28] Wang, Z. *et al.* Real-time signal processing enabled by fused networks on a memristor-based system on a chip. *Science Advances* **11**, eadv3436 (2025).

[29] Zaidi, A. A. *et al.* OFDM numerology design for 5G New Radio to support IoT, eMBB, and MBSFN. *IEEE Communications Standards Magazine* **2**, 78–83 (2018).

[30] Kim, S., Jung, Y. & Lee, S. Multipoint combined processing for FMCW LiDAR. *IEEE Sensors Journal* **22**, 8933–8943 (2022).

[31] Heo, J., Jung, Y., Lee, S. & Jung, Y. FPGA implementation of an efficient FFT processor for FMCW radar signal processing. *Sensors* **21** (2021).

[32] Yu, W., Xie, Y., Li, B., Chen, H. & Liu, X. Spaceborne synthetic aperture radar imaging mapping methodology based on FPGA-DSP hybrid heterogeneous architecture. *The Journal of Engineering* **2019**, 7313–7317 (2019).

[33] Cooley, J. W. & Tukey, J. W. An algorithm for the machine calculation of complex Fourier series. *Mathematics of computation* **19**, 297–301 (1965).

[34] Khaddam-Aljameh, R. *et al.* HERMES-Core — a 1.59-TOPS/mm^2 PCM on 14-nm CMOS in-memory compute core using 300-ps/LSB linearized CCO-based ADCs. *IEEE Journal of Solid-State Circuits* **57**, 1027–1038 (2022).

[35] Yu, S., Jiang, H., Huang, S., Peng, X. & Lu, A. Compute-in-memory chips for deep learning: Recent trends and prospects. *IEEE Circuits and Systems Magazine* **21**, 31–56 (2021).

[36] Aguirre, F. *et al.* Hardware implementation of memristor-based artificial neural networks. *Nature Communications* **15**, 1974 (2024).

[37] Song, W. *et al.* Programming memristor arrays with arbitrarily high precision for analog computing. *Science* **383**, 903–910 (2024).

[38] Xiao, T. P. *et al.* Analysis and mitigation of parasitic resistance effects for analog in-memory neural network acceleration. *Semiconductor Science and Technology* **36**, 114004 (2021).

[39] Xiao, T. P. *et al.* On the accuracy of analog neural network inference accelerators. *IEEE Circuits and Systems Magazine* **22**, 26–48 (2022).

[40] Burr, G. W. *et al.* Access devices for 3D crosspoint memory. *Journal of Vacuum Science & Technology B* **32**, 040802 (2014).

[41] Puschel, M. & Moura, J. M. Algebraic signal processing theory: Cooley–Tukey type algorithms for DCTs and DSTs. *IEEE Transactions on Signal Processing* **56**, 1502–1521 (2008).

[42] Yang, C.-H., Yu, T.-H. & Markovic, D. Power and area minimization of reconfigurable FFT processors: A 3GPP-LTE example. *IEEE Journal of Solid-State Circuits* **47**, 757–768 (2012).

[43] Liu, S. & Liu, D. A high-flexible low-latency memory-based FFT processor for 4G, WLAN, and future 5G. *IEEE Transactions on Very Large Scale Integration (VLSI) Systems* **27**, 511–523 (2019).

[44] Agrawal, V. *et al.* In-memory computing array using 40nm multibit SONOS achieving 100 TOPS/W energy efficiency for deep neural network edge inference accelerators. *IEEE International Memory*

Workshop (IMW) 1–4 (2020).

[45] Xiao, T. P. *et al.* An accurate, error-tolerant, and energy-efficient neural network inference engine based on SONOS analog memory. *IEEE Transactions on Circuits and Systems I: Regular Papers* **69**, 1480–1493 (2022).

[46] Agrawal, V. *et al.* Subthreshold operation of SONOS analog memory to enable accurate low-power neural network inference. *International Electron Devices Meeting (IEDM)* 21.7.1–21.7.4 (2022).

[47] Koenig, W., Dunn, H. K. & Lacy, L. Y. The sound spectrograph. *The Journal of the Acoustical Society of America* **18**, 19–49 (1946).

[48] Rashtchian, C., Young, P., Hodosh, M. & Hockenmaier, J. Collecting image annotations using Amazon's Mechanical Turk. *NAACL HLT 2010 Workshop on Creating Speech and Language Data with Amazon's Mechanical Turk* 139–147 (2010).

[49] Baken, R. & Orlikoff, R. *Clinical Measurement of Speech and Voice* Speech Science (Singular Thomson Learning, 2000).

[50] Shermeyer, J. *et al.* SpaceNet 6: Multi-sensor all weather mapping dataset. *IEEE/CVF Conference on Computer Vision and Pattern Recognition (CVPR) Workshops* (2020).

[51] Rivard, G. Direct fast Fourier transform of bivariate functions. *IEEE Transactions on Acoustics, Speech, and Signal Processing* **25**, 250–252 (1977).

[52] Harris, D., McClellan, J., Chan, D. & Schuessler, H. Vector radix fast Fourier transform. *IEEE International Conference on Acoustics, Speech, and Signal Processing* **2**, 548–551 (1977).

[53] Wang, Z., Bovik, A., Sheikh, H. & Simoncelli, E. Image quality assessment: from error visibility to structural similarity. *IEEE Transactions on Image Processing* **13**, 600–612 (2004).

[54] Nilsson, J. & Akenine-Möller, T. Understanding SSIM. *arXiv:2006.13846* (2020).

[55] McKeown, M. FFT implementation on the TMS320VC5505, TMS320C5505, and TMS320C5515 DSPs. *Texas Instruments Incorporated, White Paper SPRABB6B* (2010).

[56] Xilinx. Versal 2D-FFT Implementation Using Vitis Acceleration Library Tutorial (XD073) (2023). URL: https://github.com/Xilinx/Vitis-Tutorials/tree/2023.2/AI_Engine_Development/AIE/Design_Tutorials/06-fft2d_AIEvsHLS/AIE.

[57] Guo, Y. *et al.* A 60-mode high-throughput parallel-processing FFT processor for 5G/4G applications. *IEEE Transactions on Very Large Scale Integration (VLSI) Systems* **31**, 219–232 (2023).

[58] Liu, M., Wang, Z., Luo, H., Lin, S. & Liang, L. A novel high-throughput FFT processor with a block-level pipeline for 5G MIMO OFDM systems. *IEEE Transactions on Very Large Scale Integration (VLSI) Systems* **33**, 2059–2063 (2025).

[59] Shih, X.-Y., Chou, H.-R. & Liu, Y.-Q. VLSI design and implementation of reconfigurable 46-mode combined-radix-based FFT hardware architecture for 3GPP-LTE applications. *IEEE Transactions on Circuits and Systems I: Regular Papers* **65**, 118–129 (2018).

[60] Shih, X.-Y., Chou, H.-R. & Liu, Y.-Q. Design and implementation of flexible and reconfigurable SDF-based FFT chip architecture with changeable-radix processing elements. *IEEE Transactions on Circuits and Systems I: Regular Papers* **65**, 3942–3955 (2018).

[61] Chen, X., Lei, Y., Lu, Z. & Chen, S. A variable-size FFT hardware accelerator based on matrix transposition. *IEEE Transactions on Very Large Scale Integration (VLSI) Systems* **26**, 1953–1966 (2018).

[62] MacDonald, D. RITSAR: Synthetic aperture radar (SAR) image processing toolbox for Python (2015). URL: https://github.com/dm6718/RITSAR/.

[63] Graves, A. Sequence transduction with recurrent neural networks. *arXiv:1211.3711* (2012).

[64] Reddi, V. J. *et al.* MLPerf Inference Benchmark. *ACM/IEEE International Symposium on Computer Architecture (ISCA)* 446–459 (2020).

[65] Panayotov, V., Chen, G., Povey, D. & Khudanpur, S. Librispeech: An ASR corpus based on public domain audio books. *IEEE International Conference on Acoustics, Speech and Signal Processing (ICASSP)* 5206–5210 (2015).

[66] Lee, J., Zhang, B. & Verma, N. A switched-capacitor SRAM in-memory computing macro with high-precision, high-efficiency differential architecture. *IEEE European Solid-State Electronics Research Conference (ESSERC)* 357–360 (2024).

[67] Xiao, T. P., Bennett, C. H., Feinberg, B., Marinella, M. J. & Agarwal, S. CrossSim: Accuracy simulation of analog in-memory computing URL: https://www.cross-sim.sandia.gov.

[68] Rasch, M. J. *et al.* Hardware-aware training for large-scale and diverse deep learning inference workloads using in-memory computing-based accelerators. *Nature Communications* **14**, 5282 (2023).

[69] Zhang, D. *et al.* Fast fourier transform (FFT) using flash arrays for noise signal processing. *IEEE Electron Device Letters* **43**, 1207–1210 (2022).

[70] Warden, P. Speech commands: A dataset for limited-vocabulary speech recognition. *arXiv:1804.03209* (2018).

[71] Oppenheim, A., Willsky, A. & Nawab, S. *Signals & Systems* (Prentice Hall, 1997).

[72] Bavandpour, M., Sahay, S., Mahmoodi, M. R. & Strukov, D. Efficient mixed-signal neurocomputing via successive integration and rescaling. *IEEE Transactions on Very Large Scale Integration (VLSI) Systems* **28**, 823–827 (2019).

[73] Marinella, M. J. *et al.* Multiscale co-design analysis of energy, latency, area, and accuracy of a ReRAM analog neural training accelerator. *IEEE Journal on Emerging and Selected Topics in Circuits and Systems* **8**, 86–101 (2018).

[74] Murmann, B. ADC Performance Survey 1997-2025 (2025). [Online]. Available: https://github.com/bmurmann/ADC-survey.

[75] Balasubramonian, R., Kahng, A. B., Muralimanohar, N., Shafiee, A. & Srinivas, V. CACTI 7: New tools for interconnect exploration in innovative off-chip memories. *ACM Transactions on Architecture and Code Optimization (TACO)* **14**, 14:1–14:25 (2017).

[76] AMD. AI Inference with Versal (TM) AI Core Series (2023). [Online]. Available: https://www.xilinx.com/content/dam/xilinx/publications/solution-briefs/xilinx-versal-ai-compute-solution-brief.pdf.

[77] Shi, J. *et al.* Evolution and optimization of BEOL MOM capacitors across advanced CMOS nodes. *European Solid-State Device Research Conference (ESSDERC)* 190–193 (2018).

Methods

SONOS analog IMC demonstration system

The SONOS IMC chip used in this work was fabricated in a commercial 40-nm foundry process. The formation of the embedded SONOS memory cell in Fig. 2a was integrated into the front-end-of-line CMOS logic process. The IMC chip contains a 1024×1024 array of SONOS memory cells along with analog and digital circuitry to support write, read, and analog MVM operations. Fig. S3 shows the analog IMC demonstration system used in this work. The fabricated die was wire-bonded to a 100-pin thin quad flat package (TQFP), and the packaged SONOS IMC chip was mounted on a socket on a custom-designed circuit board. Commands and input/output data were sent to and from the IMC chip through an Infineon Technologies ARM microcontroller on a second custom-designed board. Four Keysight N6705C DC power supplies and a 9V power adapter were used to power the IMC chip, microcontroller, and boards. The microcontroller communicates with the host PC through a USB interface. All experiments were conducted through sequences of read, write, and analog MVM commands that were sent to the microcontroller using a Python application programming interface.

Programming and characterizing the SONOS array

The conductances of the SONOS devices were programmed with a write-verify algorithm that was designed to minimize variability and drift. To obtain a precise and stable conductance, the algorithm selectively places charge in deep, mid-gap electronic traps within the nitride that have a large energy barrier for charge confinement, while vacating charge from shallow traps near the band edges that de-trap over short timescales [44, 45]. All conductances and currents reported in this work were measured with the same voltage bias at the four terminals of the SONOS cell in Fig. 2a: 0.06V on the bit line (V_{BL}), 2.5V on the select transistor gate (V_{SG}), 0V on the source line (V_{SL}, the select transistor source), and 0V on the control gate (V_{CG}, the SONOS transistor gate). The resolution of the SONOS cell current measurements is 0.88 nA, set by the fine-resolution setting of the 12-bit ADC on the IMC chip. Our systematic characterization of the state-dependent programming variability and conductance drift in the SONOS cells is described in Supplementary Section 3.

When programming a DFT matrix onto a section of the SONOS array, the complex-valued matrix $\mathbf{W}_K$ is first decomposed into four real matrices as shown in Fig. 2b to support multiplication with a complex-valued input vector $\mathbf{x}$. Each real value is encoded by the difference in conductance of two SONOS cells. We use the convention where for a positive-valued weight, one cell encodes the absolute value while the other cell is programmed to a target of 0 µS, and vice versa for negative weights [39]. The maximum SONOS conductance $G_{\max}$ used to represent DFT weights was set primarily by the ADC input current limit of 17 µA. A large $G_{\max}$ would cause excessive clipping of analog current sums by the ADC, while a small $G_{\max}$ reduces the effective DFT weight precision because the conductance errors (shown in Fig. S5e) become a larger fraction of the utilized conductance range. To balance these errors, we first simulated all of the analog DFT operations for each of our FFT experiments prior to programming. We then set $G_{\max}$ to the largest value which ensured that 99.99% of the simulated analog sums were not clipped by the ADC, then programmed the SONOS array using this value. In general, the selected $G_{\max}$ decreases with increasing DFT size because more SONOS cell currents are summed. For the results in Figs. 3, 4, and 5, we used $G_{\max} = 20$ µS for the DFT-8 and DFT-16 arrays, $G_{\max} = 16.7$ µS for DFT-32, and $G_{\max} = 6.2$ µS for DFT-256. Supplementary Section 4 has additional experimental results on the conductance statistics for DFT arrays of various sizes.

SONOS chip analog DFT computation

To compute analog MVMs, input values are applied bit-serially to the SONOS array to the select gate (SG) lines. If a bit is '1', the SG is driven to 2.5V to turn on the select transistor, and the SONOS transistor conducts current from the BL to the source line (SL). If a bit is '0', the SG is biased to 0V, and the cell does not conduct any current from the BL. Each BL is held at 0.06V by a voltage regulator. The control gate (CG) is held at 0V. The SONOS cell conducts current only in one direction (BL to SL), which keeps its drain current more robust to variations in the BL voltage. For each input bit, the summed current on each BL is converted to a voltage using a TIA, then converted to a 12-bit digital value by the ADC. In analog MVM mode, the on-chip ADC has an input current dynamic range of 17 µA and a current spacing between ADC levels of 4.88 nA. Any summed current that exceeds this limit is clipped to the maximum value upon digital read-out.

To increase the throughput of analog MVMs on the test chip for smaller DFT sizes ($K < 64$), we programmed multiple copies of the DFT matrix onto the SONOS array and tiled them block-diagonally. This allowed multiple bit-wise MVMs to be processed concurrently in a single analog MVM. All SONOS cells not lying along the block diagonal were programmed to 0 µS. The large On/Off ratio of the SONOS memory eliminates sneak currents and ensures that the bit-wise MVM results are independent. MVMs with positive and negative input values were computed in separate cycles then subtracted digitally. On this chip, the results of each analog bit-wise MVM were digitized. To obtain the final real and imaginary DFT outputs, the following digital post-processing steps were conducted: (1) for each analog MVM, subtraction of the summed results for positive and negative weights, (2) for each input magnitude bit, subtraction of the results for positive and negative inputs, and (3) for each input magnitude bit, power-of-two weighted accumulation of the result.

For all experiments, we used 13-bit signed integers (12 magnitude bits and a sign bit) for the inputs to each analog DFT, with the exception of the first VR-FFT stage which used 8-bit unsigned integers since this was the original format of the JPEG images. Intermediate results between DFT stages were re-quantized to 13 bits before the next analog DFT stage, over a range that is set by their maximum value. The digital baseline FFTs used the same resolution for the input audio waveform or image as the analog FFTs, but used FP32 precision for the computation. In the experiments, twiddle factor multiplications between the DFT stages of the FFT were computed digitally at FP32 precision. As described in the main text and in Supplementary Section 1, it is also possible to fold the twiddle factor multiplications into the analog MVMs for higher efficiency. Since the audio and image signals used for the experiments were purely real, their frequency spectra should be zero-symmetric with frequency. To produce the audio spectra in Fig. 3, we calculated the element-wise mean of the complex-valued positive- and negative-frequency spectral components that were computed by the SONOS array.

Vector-radix FFT details

We describe here the mathematical formulation of the 2D VR-FFT and its implementation using analog MVMs, which is summarized in Fig. 4a. Analogous to the 1D case, the first step is to reshape the 2D input matrix $\mathbf{x}$ to a 4D matrix $\tilde{\mathbf{x}}$, with dimensions $R \times S \times P \times Q$, where $M = P \times R$ and $N = Q \times S$. The values of R, S, P and Q are the sizes of the elementary DFT operations in the factorization and are directly related to the dimensions of the constituent analog MVMs. As drawn in Fig. 4a, this reshape can be visualized as partitioning $\mathbf{x}$ into an $R \times S$ grid of sub-matrices, each of which has dimensions $P \times Q$. The matrix $\tilde{\mathbf{x}}$ has four indices: the pair (r, s) indexes a sub-matrix and the pair (p, q) indexes an element of the sub-matrix. In the VR-FFT, a $P \times Q$ 2D DFT is first performed on every sub-matrix $\tilde{\mathbf{x}}_{r,s}$, then the resulting matrix is element-wise multiplied by a matrix of twiddle factors $\mathbf{T}_{r,s}$ whose values also depend on the sub-matrix. The result is a 4D intermediate matrix $\mathbf{y}$ with the same dimensions as $\tilde{\mathbf{x}}$, where each sub-matrix is specified by:

$$\mathbf{y}_{r,s} = \mathbf{T}_{r,s} \odot [\mathbf{W}_Q(\mathbf{W}_P\, \tilde{\mathbf{x}}_{r,s})^{\mathrm{T}}]^{\mathrm{T}} \tag{5}$$

Next, the positions of the (p, q) and (r, s) axis pairs of $\mathbf{y}$ are exchanged to form a matrix $\tilde{\mathbf{y}}$ with dimensions $P \times Q \times R \times S$. Afterwards, an $R \times S$ 2D DFT is performed on every sub-matrix of $\tilde{\mathbf{y}}$:

$$\tilde{\mathbf{X}}_{p,q} = [\mathbf{W}_S(\mathbf{W}_R\, \tilde{\mathbf{y}}_{p,q})^{\mathrm{T}}]^{\mathrm{T}} \tag{6}$$

Finally, the 4D matrix $\tilde{\mathbf{X}}$ is re-shaped to obtain the 2D spectrum $\mathbf{X}$.

Each of the smaller 2D DFTs in Equation 5 and 6 can be computed using a sequence of analog MVMs within a resistive memory array. The four matrix-matrix multiplications in the two equations comprise the four stages of the VR-FFT that must be computed sequentially. The number of required ADC conversions, without any further application of Cooley-Tukey decomposition, is proportional to the product $PQRS$, or $\mathcal{O}(MN)$. In the limit of a very large 2D DFT, these constituent 1D DFTs can be computed using 1D analog FFTs, and their energy would each scale as $\mathcal{O}(N \log_K N)$, where K is the size of the elementary analog DFT. The total number of ADC conversions needed for the VR-FFT would scale in this regime as $PQRS \times (\log_K P + \log_K Q + \log_K S + \log_K R)$, which is equivalent to $\mathcal{O}(MN \log_K(MN))$. For square DFTs where $M = N$, this asymptotic scaling law simplifies to $\mathcal{O}(N^2 \log_K N)$.

Accuracy simulations of the SONOS FFT/DFT

Accuracy simulations of the analog FFT in Fig. 5 and the Supplementary Information were conducted using the CrossSim modeling tool [67]. These simulations were conducted in two modes: (1) behavioral

replication of the fabricated 40-nm SONOS test chip to validate the realism of our simulations, and (2) modeling of a more efficient 40-nm SONOS IMC core that is described in Supplementary Section 11.

In mode 1, we chose the analog hardware parameters in CrossSim to model: the bit-serial operation of analog MVMs; the SONOS cell conductance variability, drift, and read noise; 12-bit ADC quantization and clipping for each bit-wise MVM; and parasitic resistances in the array. Modeling of the variability and drift in the SONOS cells is based on analytical fits to the conductance characterization data in Fig. S5e and S5f; for replicating an experiment, the drift time was set to one or three days, depending on the actual time since programming for a specific experiment. Random errors due to SONOS variability and drift were re-sampled by running multiple Monte Carlo simulations of the full workload. By contrast, random cycle-to-cyle read noise was re-sampled on every bit-wise analog MVM, and was modeled based on the 40-nm SONOS noise properties reported in Ref. 44. The simulated accuracy values in Fig. 5a-b report the mean of ten Monte Carlo runs; the variance on all the accuracies were small. To model the effects of parasitic IR drops on accuracy, we added an error to the summed currents that increased quadratically with the correct value of the summed current, similar to the method used in Ref. 68. This simple model does not capture the complicated input data dependence and spatial non-uniformity of the IR drops [38], but fits well to the average trend of the errors in Fig. 2f. Fig. S16 shows that simulations using this mode match well to our experimental results.

In mode 2, we retained the same models for the SONOS device variability, read noise, and array parasitic resistance. We modeled one day of SONOS drift, as we expect a more optimized chip to have much higher throughput, and a weight refresh interval of one day would have a very small power and endurance overhead in real edge deployments. Additionally, we modified the MVM accuracy model to subtract the currents from positive and negative weight columns, and from positive and negative inputs, in the analog domain prior to the ADC. We also assumed charge-domain analog accumulation of partial results from different input bits. These changes reduce the number of ADC conversions as well as the dynamic range of inputs to the ADC; the required circuit modifications are discussed in Supplementary Section 11. The ADC resolution was changed from the test chip's resolution of 12 bits to 8, 9, or 10 bits for the different results in Fig. 5a-b. To minimize both quantization and clipping errors at these lower resolutions, the input dynamic range for each ADC was optimized based on profiling of the input data for the individual analog DFT stages, as well as the neural network layers in RNNT.

DSP workload accuracy simulations

The analog FFT operations that were simulated for the workload results in Fig. 5a and 5b used mode 2 of the analog FFT accuracy simluation, described above.

For the SAR results in Fig. 5a, we used raw SAR sensor data that was collected on a test flight by Sandia National Laboratories, available at Ref. [62]. We also used the Python implementation of the polar-format algorithm in this repository, without modification until the 2D DFT step. The complex-valued SAR phase history contains data that are sampled at discrete points on a polar annulus in the spatial frequency domain. The polar-format algorithm interpolates this data onto a rectangular grid, first along the range then along the azimuth direction. Then, a 2D DFT is performed to obtain a real-space image. We simulate analog processing only for the 2D DFT step while the other parts of the algorithm are done in digital. We quantized the floating-point inputs to the DFT to 8 bits (sign-magnitude), for both the FP32 FFT and the analog VR-FFT; we found that this made a negligible difference in the final image. No Parseval correction was applied for the analog VR-FFT. The magnitude of the FFT result is plotted on a logarithmic scale in Fig. 5a, normalizing by the maximum pixel value of the FP32 formed image. The SSIM was computed using the logarithmic-scale images in Fig. 5a. We note that the raw data was collected using 1999 chirp pulses with 1800 samples per pulse, where each pulse had the same center frequency of 2.67 GHz. This was slightly upsampled to form a 2048×2048 image.

For the ASR results in Fig. 5b, STFTs were simulated on raw Librispeech audio waveforms using 512-point analog FFTs, with a Cooley-Tukey decomposition of $N_1 = 32$ and $N_2 = 16$. These were applied to zero-padded windows with a window size of 320 samples, a hop length of 160 samples, and a Hanning window function. This was followed by a few digital steps prior to passing the inputs to RNNT: conversion to a power spectrogram, conversion to a Mel-frequency spectrogram with 80 logarithmically spaced frequency bins (features), element-wise logarithm, and per-feature normalization to a mean of zero and standard deviation of one. Within RNNT, all LSTM and FC layers were simulated using CrossSim, using the same hardware parameterizations as the analog FFT but with a fixed ADC resolution of 8 bits. Transcendental functions in the LSTMs were assumed to be computed digitally, and weight matrices larger than 1024×1024 were partitioned across multiple SONOS arrays with separate ADCs.

SONOS IMC core energy, performance, and area projections

The fabricated 40-nm test chip used for our experiments was designed to demonstrate high-precision SONOS-based analog MVMs, but was not optimized for performance, power efficiency, or area. Therefore, the energy, performance, and area metrics for the analog FFT in Fig. 5c-d are modeled based on a more optimal SONOS-based IMC core design with faster and more efficient peripheral circuits. The details of these energy, performance, and area models are described in Supplementary Section 11.

Versal AI Engine benchmarking

The FFT energy values in Fig. 5c for the AMD Versal were obtained by executing 2D-FFT designs on a Versal AI core (VC1902) chip, following the documentation in Ref. 56. The designs implemented 2D row-column FFTs of various sizes ($N \times N$, from $N = 64$ to $N = 2048$) at CINT16 precision on the AI Engines, and were compiled using the AMD Vitis AI tool (version 2023.1) for the VCK190 evaluation board. The compiled programs were serially written to bootable program images, which were written to SD cards using the BalenaEtcher tool, and then booted up one at a time on the VCK190's PetaLinux environment, then finally executed on the AI Engines. The AI Engines were run at 1.00 GHz and communicated with a data mover kernel via a 128-bit AXI4-Stream interface at 312.5 MHz. We report results from runs that contained five parallel instances of the same design on the chip, which reduced the per-instance power consumption. The latencies of individual 2D FFTs were obtained from the runtime trace data, and these were scaled to derive the latencies of 1D N-point FFT in the batch. Power estimates were obtained from the Xilinx Power Design Manager tool in a vector analysis mode, which used switching data from detailed timing simulations to produce accurate estimates of signal toggle rates and dynamic power consumption. We include only the power consumption of the AI Engines to ensure a fair comparison with the other FFT accelerators. The energy per FFT was obtained by multiplying the 1D FFT latency by the per-instance power consumption. For Fig. 5c, the energy was further reduced by 2× to estimate the power for an 8-bit (rather than 16-bit) word length.

Acknowledgements

We thank A. Talin and W. Wahby for comments and feedback on the manuscript. This work was supported by the Laboratory-Directed Research and Development (LDRD) Programs at Sandia National Laboratories. This article has been authored by an employee of National Technology & Engineering Solutions of Sandia, LLC under Contract No. DE-NA0003525 with the U.S. Department of Energy (DOE). The employee owns all right, title and interest in and to the article and is solely responsible for its contents. The United States Government retains and the publisher, by accepting the article for publication, acknowledges that the United States Government retains a non-exclusive, paid-up, irrevocable, world-wide license to publish or reproduce the published form of this article or allow others to do so, for United States Government purposes. The DOE will provide public access to these results of federally sponsored research in accordance with the DOE Public Access Plan https://www.energy.gov/downloads/doe-public-access-plan.

Supplementary Information

Appendix 1 Parallelized analog FFTs for high throughput

In the most area-efficient implementation of the analog FFT, all of the elementary DFTs within an FFT stage are computed sequentially using a single resistive memory array. However, this implementation comes at a penalty to latency and throughput, due to the sequential execution of matrix-vector multiplications (MVMs) that make up each matrix-matrix multiplication. To attain higher speed at the cost of area, the elementary DFTs within an FFT stage can be executed in parallel across multiple arrays, rather than sequentially using a single array. This solution is shown in Fig. S1. In this scheme, the N_1 MVMs of the first stage are computed in parallel across N_1 arrays that each store the matrix $\mathbf{W}_{N_2}$. Likewise, the N_2 MVMs of the second stage are computed in parallel across N_2 arrays.

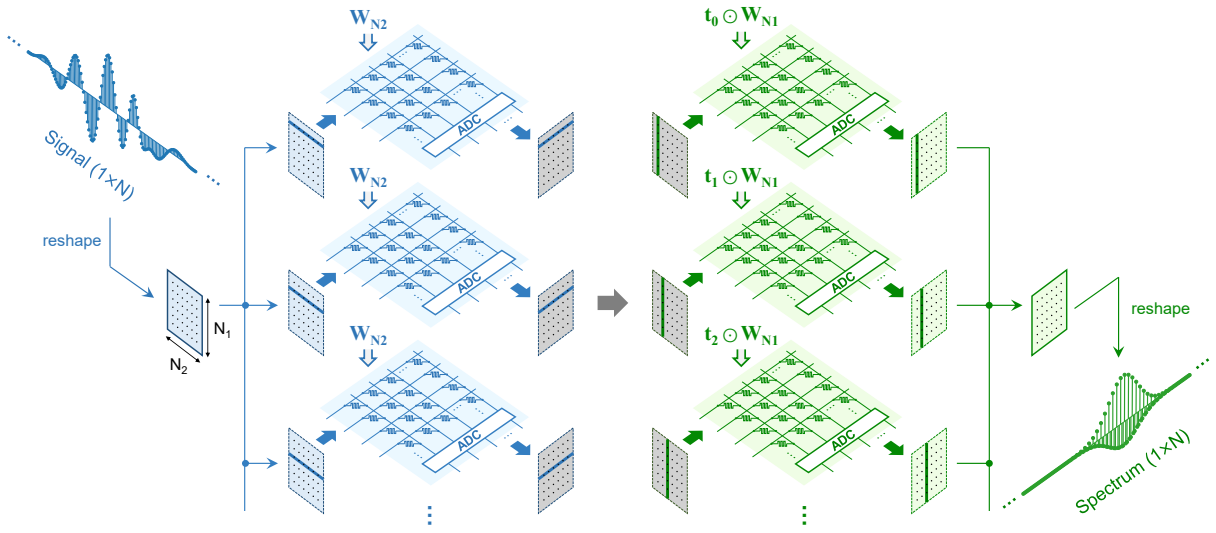

Fig. S1 High-throughput parallelized implementation of an analog FFT with a single Cooley-Tukey decomposition.

In addition to high throughput, another benefit of this parallelized scheme is that **it eliminates the need for explicit digital twiddle factor multiplications**. Instead, the twiddle factor multiplications can be folded into the analog MVMs of the second stage so that they introduce no additional energy, latency, or storage overhead during runtime. This can be done by first decomposing the $N_1 \times N_2$ twiddle matrix into its column vectors: $\mathbf{T} = [\mathbf{t}_0 \ \mathbf{t}_1 \ \mathbf{t}_2 \ ... \ \mathbf{t}_{N_2-1}]$. Each of the N_2 memory arrays that are allocated for the second stage is then programmed with a unique matrix; the i^{th} array is programmed to store $\mathbf{t}_i \odot \mathbf{W}_{N_1}$, where $\odot$ is an element-wise or Hadamard product. In this hardware implementation, the twiddle multiplications come at zero additional cost in time, energy, or area. We also note that the cost of an element-wise multiplication pre-processing step (e.g. a window function) can also be eliminated using the same method, by folding it into the programmed matrices of the first stage. The parallel MVMs in the first stage, the storage of intermediate results, and the parallel MVMs in the second stage can all be pipelined. This allows the parallel analog FFT to match the throughput of an analog direct MVM approach.

In mathematical terms, this hardware implementation can be understood to implement the equation below, which yields the same result as Equation (3):

$$\mathbf{X} = [\mathbf{I}_{N_2} \otimes_i (\mathbf{t}_i \odot \mathbf{W}_{N_1})]\, \mathbf{P}\, (\mathbf{I}_{N_1} \otimes \mathbf{W}_{N_2})\, \mathbf{x} \tag{A1}$$

where $\mathbf{I}_k$ is the $k \times k$ identity matrix and $\otimes$ is the Kronecker product. The product $\mathbf{I}_{N_1} \otimes \mathbf{W}_{N_2}$ is equivalent to tiling the matrix $\mathbf{W}_{N_2}$ block-diagonally N_1 times. The notation $\mathbf{I}_{N_2} \otimes_i \mathbf{F}_i$ indicates a direct sum of matrices, i.e. tiling the matrices $\mathbf{F}_0, \mathbf{F}_1, ..., \mathbf{F}_{N_2-1}$ block diagonally, following Ref. 41. In hardware, the block diagonals are implemented in separate arrays while the zero-valued off-diagonal elements do not need to be implemented. In this mathematical formulation, $\mathbf{x}$ is transformed into $\mathbf{X}$ through two large MVMs rather matrix-matrix multiplications. $\mathbf{P}$ is a matrix that represents a permutation operation on

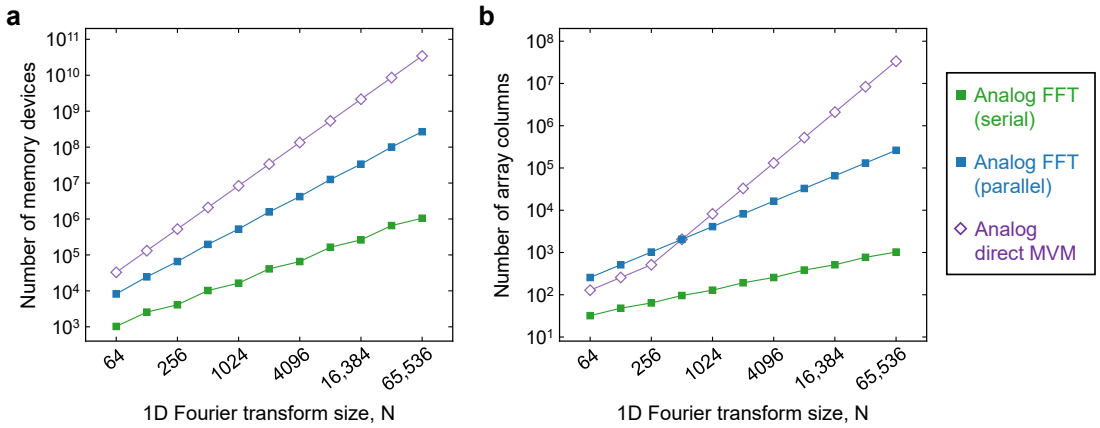

Fig. S2 Comparison of the area scaling of the serial implementation of the analog FFT, parallel implementation of the analog FFT, and the analog direct MVM implementation of the DFT, in terms of (a) total number of memory devices, and (b) total number of array columns. The maximum array size is assumed to be 512×1024, which implements an elementary DFT size of 256.

the intermediate $N \times 1$ vector, and performs the equivalent function to the inner transpose in Equation (3). The 1D vectors $\mathbf{x}$ and $\mathbf{X}$ differ only by a possible permute operation from the original input signal and the final DFT output, respectively.

Even after provisioning for multiple arrays, the parallel analog FFT has a more favorable area scaling than the analog direct MVM while achieving the same throughput. This is shown in Fig. S2, which compares the area scaling of the analog direct MVM, and two implementations of the analog FFT: the serial implementation in Fig. 1b, and the parallel implementation in Fig. S1. For this scaling analysis, we consider two proxies for the total area: the total number of resistive memory devices (if the memory array area dominates), and the total number of memory array columns (if the column peripheral circuitry area dominates). By both measures, the area overhead of the parallel FFT scales much more slowly with the transform size compared to the direct MVM; for large N, the area overhead of the parallel FFT is several orders of magnitude smaller.

We note that the dynamic reconfigurability property of the analog FFT that was described in Section 2 still holds even when the twiddle matrices are folded into the DFT matrices to implement this parallel FFT scheme. This is shown in Supplementary Section 5.

Appendix 2 SONOS analog IMC chip and demonstration system

Fig. S3 shows the hardware demonstration system used for the experiments in this work. Additional details are described in Methods. We note that this IMC chip was designed to demonstrate accurate analog MVMs using a large, 1024×1024 SONOS array, but the chip was not optimized for power efficiency, speed, or area.

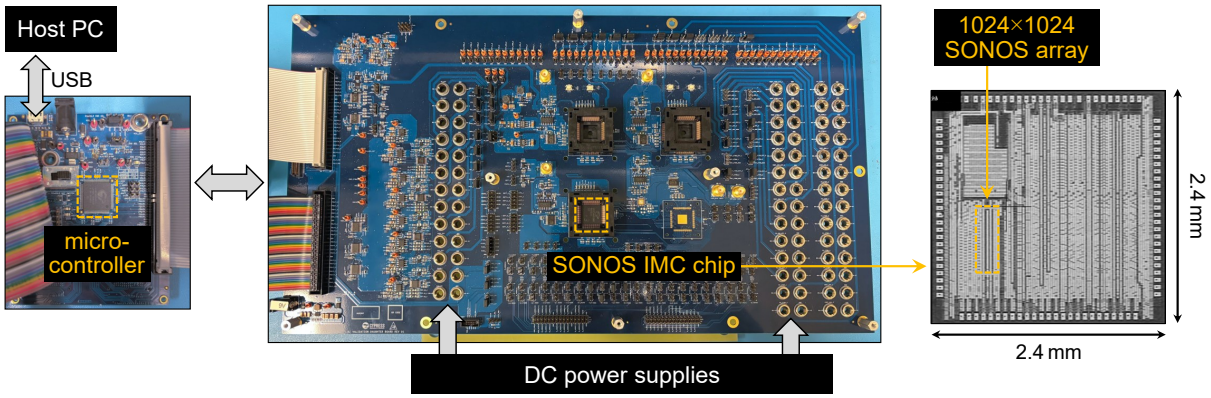

Fig. S3 Diagram of the hardware demonstration system used for the analog DFT and FFT experiments in this work. The packaged SONOS in-memory computing (IMC) chip was mounted on a 100-pin TQFP socket on a custom-designed board (center) that included components necessary to power the IMC chip. Only one of multiple sockets on the board was used for this experiment. Data and commands were sent to and from the IMC chip to an Infineon Technologies ARM microcontroller on a second custom board (left), connected to the center board through ribbon cables. The microcontroller communicated with the host PC through a USB interface. The boards were powered by four Keysight N6705C power supplies and a 9V power adapter, which were left disconnected in the photo. The right side shows a die photo of the IMC chip. The yellow rectangle shows the location of the 1024 × 1024 SONOS array, though the structure of the array is not visible due to metal over-layers.

Appendix 3 SONOS charge-trapping memory and analog state characterization

This work used a non-volatile charge-trapping memory technology based on the SONOS (silicon-oxide-nitride-oxide-silicon) material stack, shown in Fig. S4a. The state variable in this memory is the quantity of charge that is stored in a silicon nitride layer, which is intentionally rich with defects that act as electronic trapping sites. During programming, charge is added or removed from the trapping layer by Fowler-Nordheim tunneling of electrons or holes through the lower oxide, as shown in Fig. S4a. The amount of trapped charge changes the threshold voltage of the underlying transistor channel, which is shown in Fig. S4b. While the stored charge is not part of the conductive channel, it electrostatically modulates its conductance. The quantity of charge within the structure remains stable over time due to the double confinement provided by the energy wells of the electronic traps and the potential barriers at the nitride-oxide interfaces. The traps span a range of energies inside the nitride bandgap; "deep" traps close to the midgap have larger energy barriers than "shallow" traps close to the band edges.

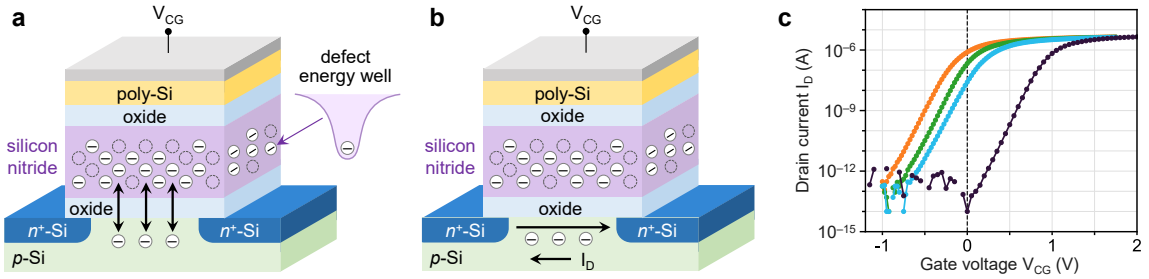

Fig. S4 Simplified diagram of a SONOS charge-trapping memory device. (a) During programming, charge is injected into electronic traps in the silicon nitride layer by tunneling. (b) During read or analog MVM, current flows between the source and drain (left and right) terminals, through a channel whose conductance is electrostatically modulated by the trapped charge through the field effect. (c) I_D-V_{CG} transfer characteristics of a SONOS memory cell, which has four terminals as shown in Fig. 2a. The curves correspond to four non-volatile states which draw a current of 800 nA (orange), 200 nA (green), 25 nA (blue), and < 1 pA (black) at $V_{CG} = 0$V. Here, the select gate is fixed at 2.5V, the bit line voltage is 0.1V, and the select transistor source is 0V. Note that this bias differs from the bit line voltage of 0.06V used for reads and analog MVMs in the rest of the paper.

Fig. S4c shows the gate transfer characteristics of an individual SONOS cell, which also contains a select transistor as shown in Fig. 2a. The curves correspond to different programmed non-volatile states, showing multiple values of the threshold voltage. For this measurement, we used a semiconductor parameter analyzer to bypass the resolution limits of the on-chip ADC. As described in Methods, during read and MVM operations, a fixed voltage bias ($V_{SG} = 2.5$V, $V_{CG} = 0$V, and $V_{BL} = 0.06$V, relative to the select transistor source) is applied to the terminals, and the conductance of the SONOS device is defined under this operating bias. This condition is approximately represented by the dashed line in Fig. S4c, with the difference that $V_{BL} = 0.1$V in this measurement. Nonetheless, this shows that a very large conductance dynamic range spanning about six orders of magnitude is accessible.

A SONOS device that is programmed to operate in the subthreshold regime can have extremely low conductance, down to $G < 1$ pS; this state is used to store zero-valued DFT weights. For the non-zero DFT weights, we still primarily operate the SONOS device in the subthreshold or weak inversion regime, where the silicon channel has not fully inverted but its conductance can nonetheless be tuned with high precision. For the higher conductance values used in this paper ($G > \sim$10 µS), the devices operate in the strong inversion regime, where the channel has a high density of free electrons.

Separately from the FFT experiments, we characterized the state-dependent conductance variability and drift characteristics of the SONOS analog memory cells. This was done by programming a 128×512 portion of the array to a gradient pattern of conductance targets. The gradient pattern consisted of a 4×32 tiling of 128 blocks, where each block is a 32×16 rectangular group of SONOS cells. All 512 cells within a block were programmed to the same current target. Across the blocks, 128 linearly spaced current targets were selected from 0 nA to 1400 nA (0 µS to 23.3 µS). Fig. S5a shows the measured conductances of all 65,536 SONOS cells in the gradient pattern just after programming. The conductances are read out using the on-chip ADC, with a conductance resolution of 14.7 nS. Fig. S5b shows a second measurement of the same cells taken three days after programming.

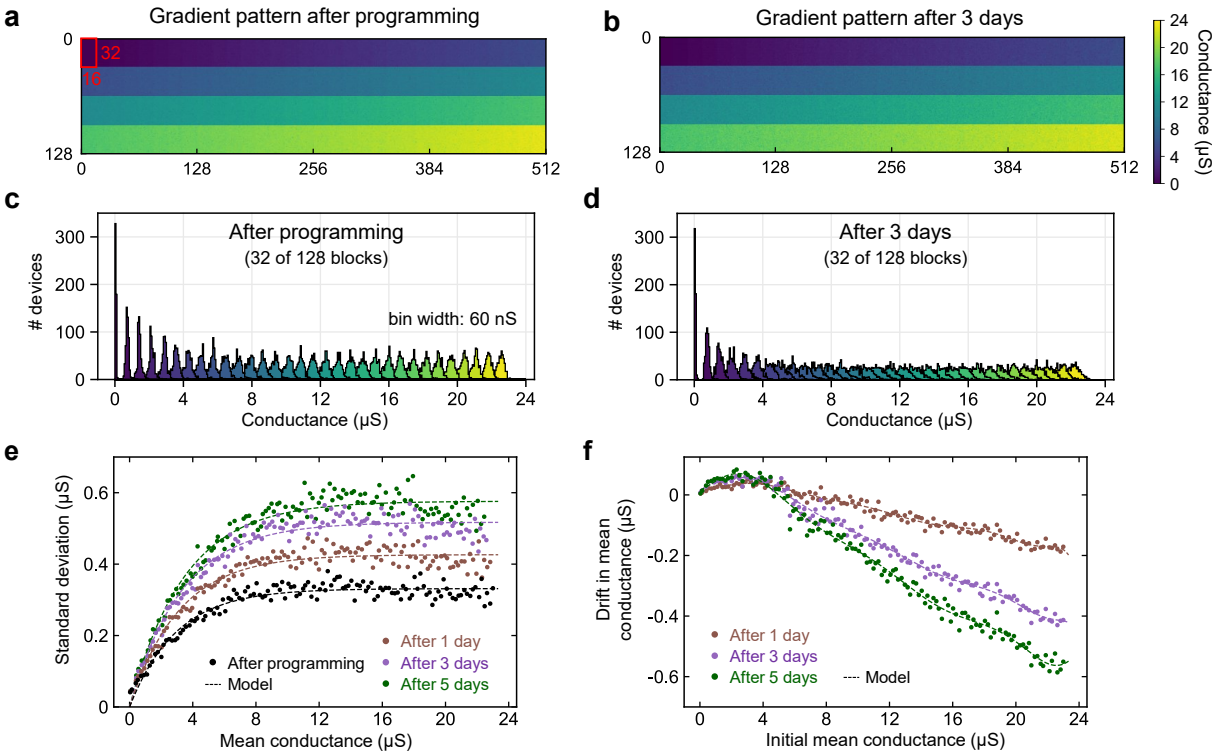

Fig. S5 (a) Spatial profile of measured SONOS conductances in a 128×512 sub-array that was programmed with a gradient pattern to characterize the state dependence of conductance variability and drift. Measurement was taken just after programming. A single block (out of 128) with a uniform target conductance is labeled. (b) Conductances in the same sub-array measured three days after programming. (c)-(d) Histograms of measured SONOS conductances in 32 of 128 blocks (every fourth block) in (a) and (b), respectively. Each block contains 512 devices. (e) Standard deviation of the conductance in all 128 blocks after programming and after one, three, and five days. (f) Drift in the mean conductance of all 128 blocks after one, three, and five days, as a function of the initial mean conductance of each block. In (e) and (f), dashed curves are fits to the data.

Fig. S5c shows the distribution of SONOS conductances for 32 of the 128 blocks, measured just after programming. Because the target conductance is uniform within a block, the ideal width of each distribution is zero. The actual non-zero width of the distributions is due to random conductance variability in the SONOS cells caused by device-to-device process variation, write noise, and read noise. This variability directly causes random errors in the values of DFT weights used for analog computation. Notably, the distributions asymptotically approach a width of zero in the limit of zero conductance. This is a unique property of the SONOS memory device when operated in the subthreshold conductance regime. In this regime, random variability in the quantity of stored charge translates linearly to a variability in V_T but exponentially to a variability in the channel conductance. When the target conductance is very low, a large random variability in V_T may induce a large *relative* variability in the conductance, but a very small *absolute* variability due to the small conductance. It can be shown that as a result, the subthreshold conductance variability is proportional to the conductance [45]. We quantify the width of each block's conductance distribution by its standard deviation, and this is plotted in Fig. S5e by the black points for all 128 blocks. The proportionality between conductance and variability at low conductance can be clearly seen. At larger conductances, the width of the distribution eventually saturates to the conductance tolerance used in the write-verify algorithm.

Fig. S5d shows the same distributions measured after three days. During this time, stored charge in the nitride layer can escape thermally from the electronic traps, and subsequently migrate within the nitride layer or leave the nitride via trap-assisted tunneling through the oxides. The drift dynamics can be complex due to the presence of both trapped electrons and trapped holes, and the fact that a defect's influence on the channel conductance depends on its physical location within the nitride layer. The programming algorithm is designed to minimize de-trapping by selectively storing charge in deep traps near the middle of the nitride bandgap, but a small number of carriers can nonetheless de-trap over this time period. The above effects induce a change in the channel's threshold voltage and conductance. Since these effects are thermal in origin and hence stochastic, the variability in conductance tends to increase

over time. This causes the conductance distributions in Fig. S5d to be wider in general than the ones in Fig. S5c. This can also be observed directly by comparing the black and purple points in Fig. S5e.

We also observed that the conductance drift over time had some systematic state dependence. Fig. S5f shows how the mean conductance of each of the 128 blocks shifted over the first day, over the first three days, and over the first five days after programming. Overall, the conductances tend to decrease with time indicating a net loss of holes or net gain of electrons with time. The state with the minimum conductance is the most stable with time for the same reason that it has the highest conductance precision; drift in V_T for deep subthreshold states induce a very small absolute change in conductance. The rate of conductance drift slows down with time as the loosely bound stored charge in the shallow traps of the silicon nitride are gradually depleted.

For accuracy simulations, the time-dependent conductance variability and the mean drift of conductance over time were modeled using analytical fits to the data in Fig. S5e and S5f, respectively. The variability was fit using a saturating exponential function of G: $\sigma(G,t) = A(t) \times \left(1 - e^{-G/B(t)}\right)$. The mean drift at each measured time point was fit using a tenth degree polynomial function of G. These analytical fits are shown by the dashed curves in Fig. S5e and S5f.

For the audio and image processing experiments in this paper, drift was an ongoing effect during the computation, i.e. later parts of the computation experienced more errors due to drift than the earlier parts. For simulation purposes, we modeled either one day or three days of drift, depending on which was closer to the actual time after programming of these experiments.

Appendix 4 Precision and distribution of SONOS DFT weights

Fig. S6 shows the constellation in the complex plane of the DFT weights that are stored physically in programmed SONOS devices for various DFT sizes. For all matrices, the ideal weights have the form $\exp(-i2\pi nk/N)$ where n and k are indices into the 2D matrix. These complex exponentials all have a magnitude of 1, so the ideal weights all lie along the unit circle in the complex plane. The weights stored in the SONOS devices are generally close to their target locations along the circle. Errors in the radial direction correspond to errors in magnitude, while errors along the circumferential direction correspond to errors in the phase of the complex-valued weights. Fig. S7 shows the mean absolute error (MAE) of both the magnitude (red) and phase (green) of the DFT weights for the different DFT sizes.

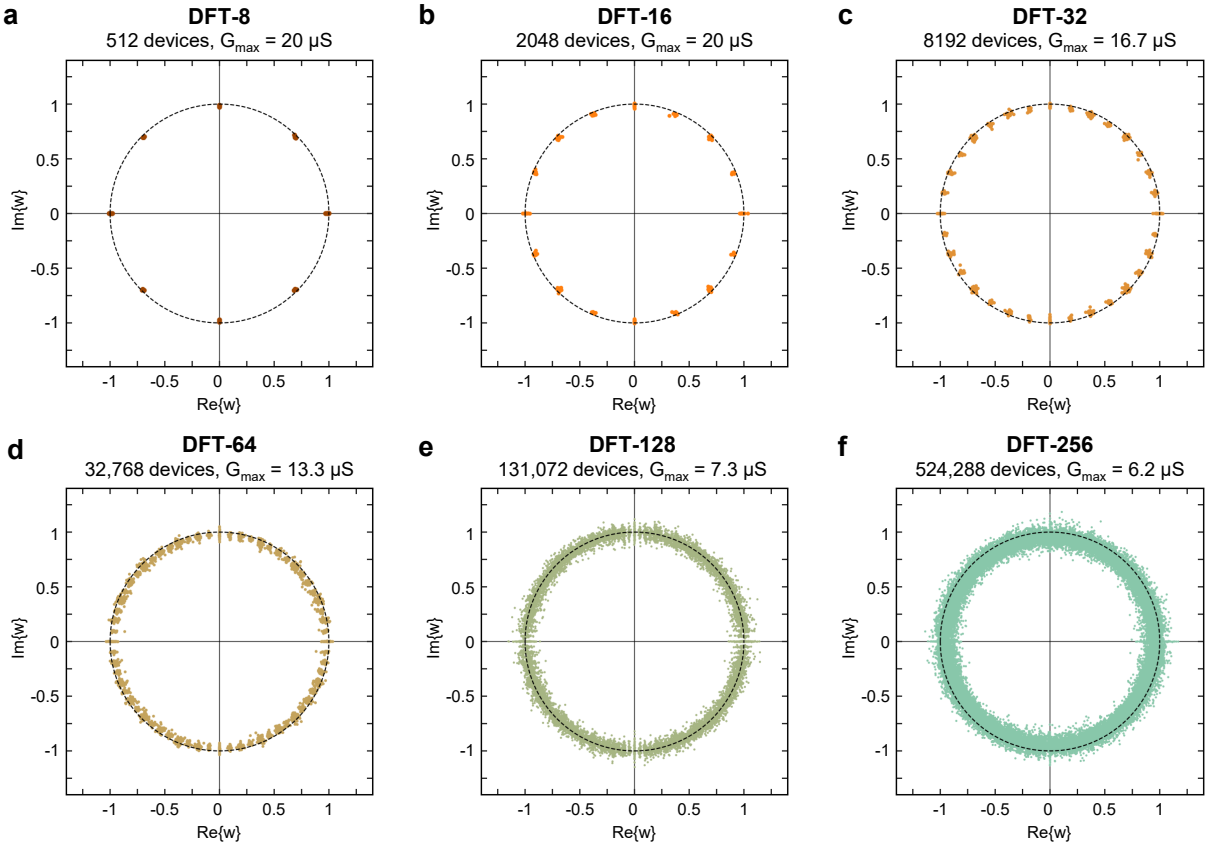

Fig. S6 Constellation of complex-valued DFT weight values stored in SONOS devices, for several sizes of the programmed DFT matrix. Weights are measured just after programming. The ideal DFT weights lie along the unit circle (dashed).

Since the DFT arrays were used for analog DFT computation in addition to weight storage, we selected the maximum SONOS conductance $G_{\max}$ to ensure optimally accurate analog MVMs. Too large a value for $G_{\max}$ induces errors due to ADC saturation and parasitic IR drops. Meanwhile, a small $G_{\max}$ reduces the precision of the DFT weights, because the conductance variability, noise, and drift become a larger proportion of the utilized conductance range. The chosen values of $G_{\max}$ in Fig. S6 were optimized for the distribution of summed column currents for the speech processing experiments. For processing the 2D spatial images, which have a much larger zero-frequency component, we selected different values for $G_{\max}$ which are shown in Table S1. For larger DFT sizes, which require larger arrays, the maximum conductance was reduced to keep the summed currents low. At the level of individual DFT weights, because the range of SONOS conductances was reduced with increasing DFT size, both the magnitude and phase errors increase with DFT size, as shown in Fig. S7.

Fig. S8 shows the distributions of the individual SONOS conductances that implement the DFT matrices in Fig. S6. As the DFT size increases, more values are sampled along the unit circle in the complex plane, causing a gradual transition from a discrete to a nearly continuous conductance distribution. Each distribution contains a large peak at the minimum conductance, because our scheme for mapping signed weights leads to at least half the SONOS devices being programmed to nearly zero conductance.

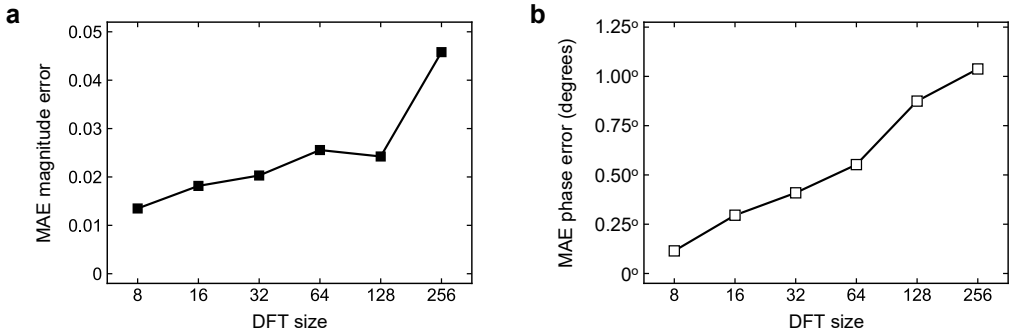

Fig. S7 Mean absolute error in the (a) magnitude and (b) phase of DFT weights stored in the SONOS array vs DFT size, based on the same SONOS weights in Fig. S6.

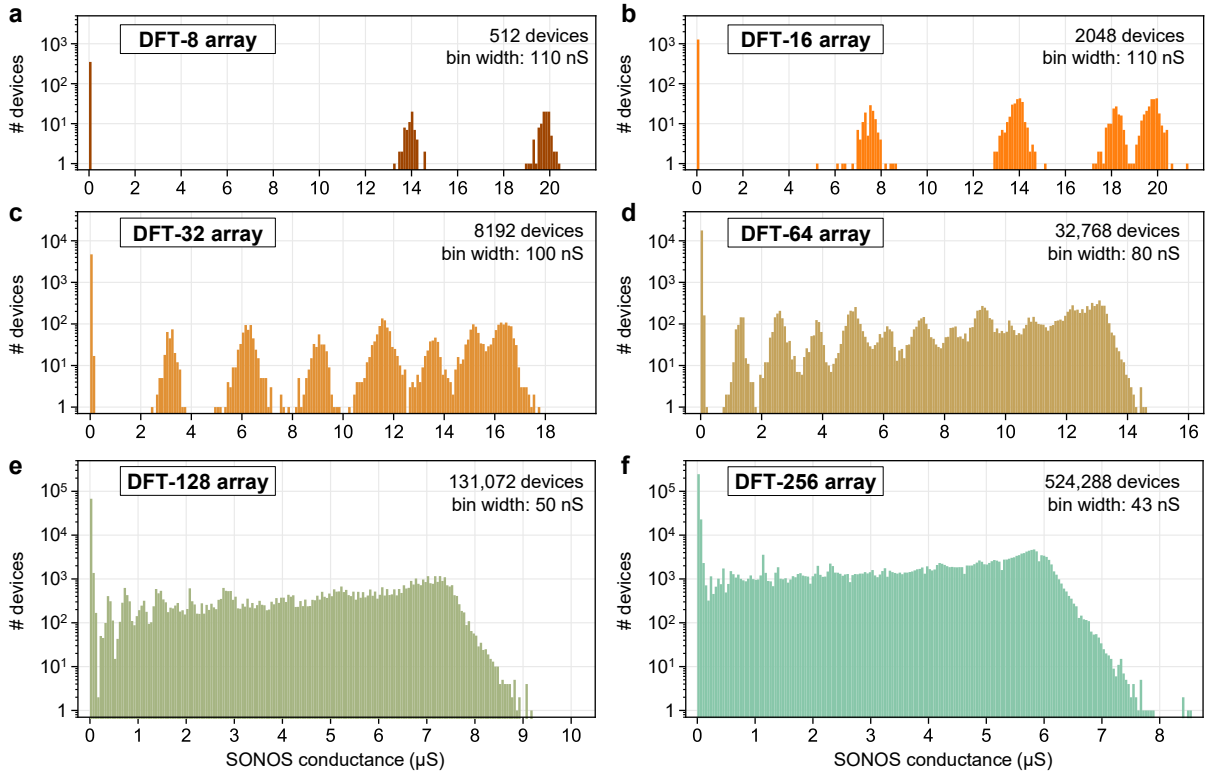

Fig. S8 Distribution of the measured SONOS conductances corresponding to the programmed DFT matrices in Fig. S6.

There is a highly consequential difference between the conductance distributions of DFT matrices and the conductance distributions of deep neural network (DNN) weight matrices. Across many different DNN models, it has been observed that the weight value distributions tend to be heavily peaked around zero, with the number of weights decaying exponentially with increasing magnitude. When using our differential mapping scheme, this leads to conductance distributions that also decay exponentially away from the minimum conductance level [39, 45]. This is not the case for the DFT weights. Because the complex-valued DFT weights are distributed uniformly around the unit circle, the conductance distribution is closer to uniform than exponential, with a much higher average conductance compared to DNNs. This observation leads to an important difference in the error tolerance of the accuracy of analog FFTs and analog DNN inference. Analog DNN inference benefits enormously from having minimal error at low conductance, while the error at high conductance is less consequential [39]. Meanwhile, for analog FFTs, it is important to keep the conductance errors low across the entire dynamic range of the device. We note, however, that a higher precision in the minimum conductance level is still beneficial for analog FFTs when using a proportional differential mapping from weights to conductances, because half of the devices in the array will utilize the minimum conductance state.

Appendix 5 Dynamic reconfigurability of the analog FFT

As described in Section 2, an analog FFT system can be dynamically re-configured to compute FFTs of smaller sizes without re-programming any memory devices. This cheap reconfigurability is possible by exploiting a property of the DFT matrix. If N_1 is a multiple of N_2, i.e. $N_2 = N_1/(a \times b)$ where a and b are positive integers, then it can be shown that:

$$(\omega_{N_2})^{nk} = e^{-i2\pi nk/N_2} = e^{-i2\pi(na\times kb)/N_1} = (\omega_{N_1})^{na\times kb} \tag{E2}$$

Therefore, an N_2-point DFT can be computed using a memory array that implements $\mathbf{W}_{N_1}$ simply by applying the inputs to every a^{th} row and measuring the outputs from every b^{th} column.

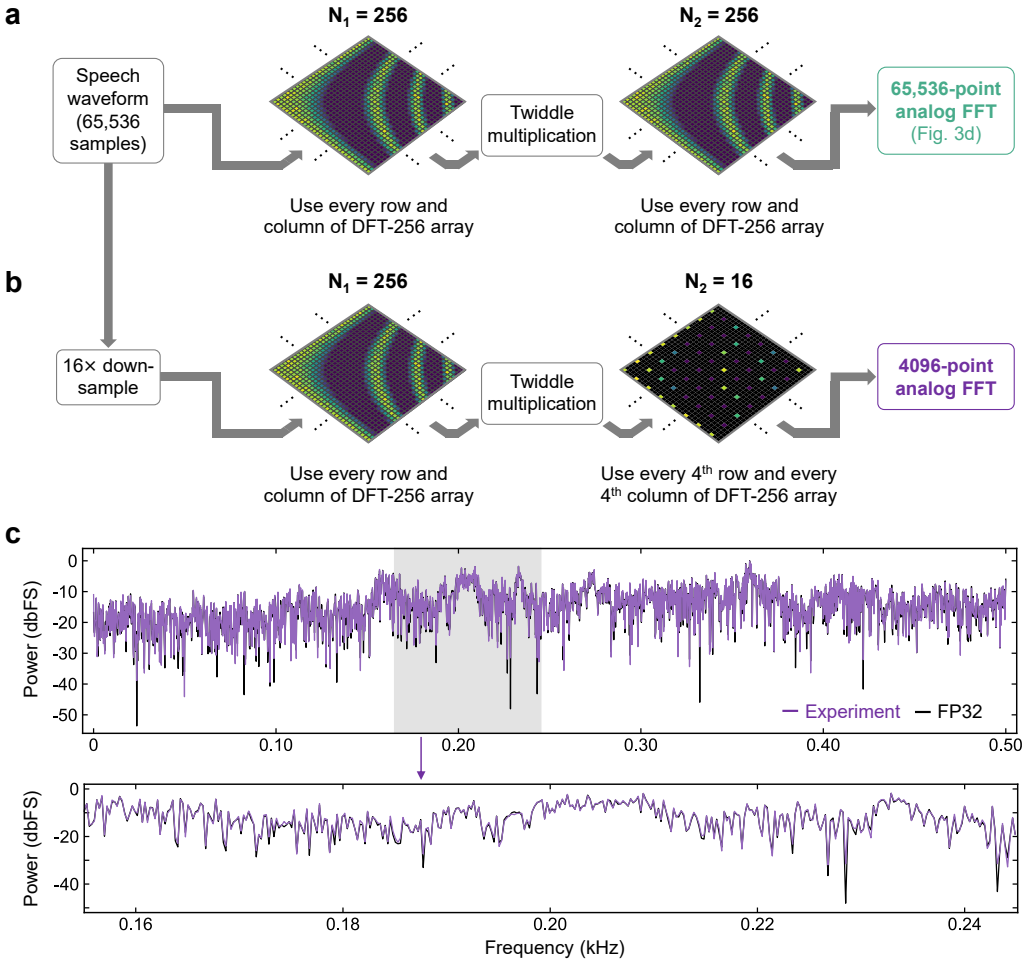

Fig. S9 (a) Fully utilizing a single programmed DFT-256 SONOS array to compute a 65,536-point FFT. The input waveform and frequency spectrum are shown in Fig. 3a and 3d, respectively. (b) A 16-point DFT can be computed by selectively activating the rows and columns of the same programmed DFT-256 array. Images show a 32×32 portion of the DFT-256 array; unused devices are colored black. (c) SONOS-computed power spectrum of the 4096-point down-sampled audio signal (top), and a zoom into one portion of the spectrum (bottom).

We demonstrate this capability by re-using the SONOS sub-array that was programmed with the DFT-256 matrix. This sub-array was initially used to compute the 65,536 analog FFT in Fig. 3d, using a Cooley-Tukey decomposition with $N_1 = N_2 = 256$. This configuration, which fully utilizes the programmed array, is shown in Fig. S9a. Next, without reprogramming any SONOS devices, we computed a 4096-point analog FFT on a 16× down-sampled version of the same audio signal, as shown in Fig. S9b. The first DFT stage used $N_1 = 256$, as before. The second DFT stage used $N_2 = 16$, where the 16-point analog DFTs were computed using the already programmed array by activating every fourth row and every fourth column. The power spectrum that is computed using the 4096-point analog FFT is shown in Fig. S9c. The SONOS-computed spectrum is in close agreement with the result of an FP32 digital FFT that was computed on the downsampled signal, with a PSNR of 36.62 dB.

This reconfigurability can be extended to the case where the technique in Supplementary Section 1 is used to "fold" the twiddle factors into the DFT matrices before programming the resistive elements. In this case, the arrays in the first DFT stage would contain the normal DFT matrices that can be reconfigured as described above, but the second DFT stage would use multiple arrays that are each programmed with an element-wise product of a DFT matrix and a different column of a twiddle matrix.

Let us consider the case where we would like to compute two different FFT sizes: $F_1 = N_1 \times N_2$ and $F_2 = N_3 \times N_4$. We assume that N_1 is a multiple of N_3 and N_2 is a multiple of N_4: $N_1 = AN_3$ and $N_2 = BN_4$, where A and B are integers that are greater than or equal to 1. For the first stage, since $N_1 \geq N_3$, the arrays would be programmed with the N_1-point DFT matrix. Since N_1 is an integer multiple of N_3, the rows and columns of these arrays can be selectively activated as described above to compute the N_3-point DFTs. Therefore, the same arrays can be re-used for the first stage of both the F_1-point and F_2-point FFTs.

Since $N_2 \geq N_4$, the arrays in the second stage would be programmed with the matrices $(\mathbf{t_j} \odot \mathbf{W}_{N_2})$, where j ranges from 0 to $N_1 - 1$. Here, $\mathbf{t_j}$ is one column of the twiddle matrix for an FFT of size F_1, so the elements of this column are: $\mathbf{t}_{\mathbf{j},k} = (\omega_{N_1 N_2})^{jk}$. Then, a single element at the index (n, k) of this "folded" matrix represents the value:

$$\begin{aligned}\left(\mathbf{t_j} \odot \mathbf{W_{N_2}}\right)_{n,k} &= (\omega_{N_1 N_2})^{jk} (\omega_{N_2})^{nk} \\ &= \exp\left[-i2\pi\left(\frac{jk}{N_1 N_2} + \frac{nk}{N_2}\right)\right]\end{aligned} \tag{E3}$$

Now, suppose we had instead programmed the arrays to execute the second stage of the F_2-point DFT. In this case, these arrays would have been programmed with a different set of folded matrices, $(\mathbf{t'_{j'}} \odot \mathbf{W}_{N_4})$. Here, $\mathbf{t'_{j'}}$ is one column of the twiddle matrix for an F_2-point FFT. A single element at the index (n', k') of this different folded matrix represents the value:

$$\begin{aligned}\left(\mathbf{t'_{j'}} \odot \mathbf{W_{N_4}}\right)_{n',k'} &= (\omega_{N_3 N_4})^{j'k'} (\omega_{N_4})^{n'k'} \\ &= \exp\left[-i2\pi\left(\frac{j'k'}{N_3 N_4} + \frac{n'k'}{N_4}\right)\right]\end{aligned} \tag{E4}$$

The question now is whether the value in Equation E4 can be accessed using the proper choice of indices in Equation E3. To find this, we can equate the arguments of the two exponentials:

$$\frac{jk}{N_1 N_2} + \frac{nk}{N_2} = \frac{j'k'}{N_3 N_4} + \frac{n'k'}{N_4} \tag{E5}$$

We make the following substitutions: $k = ak'$, $n = bn'$, and $j = cj'$, where a, b, and c are integers. Then, by equating the two terms in each sum separately, the equation above can be satisfied with the following conditions on a, b, and c:

$$a \times c = A \times B \tag{E6}$$

$$a \times b = B \tag{E7}$$

This has at least one integer solution: $a = B, b = 1, c = A$. If A or B can be factored, then there may be other solutions. In either case, this shows that by selectively activating the rows and columns of the properly selected arrays that were programmed with the folded matrices in Equation E3, we can compute an MVM with the folded matrices in Equation E4. Therefore, the parallel analog FFT technique in Fig. S1 can still be re-configured to compute FFTs of different sizes.

Appendix 6 The effect of varying analog FFT factorizations

6.1 Efficient analog FFT factorizations

There are many possible ways to factor an N-point DFT using two-factor Cooley-Tukey decompositions. Several examples are shown in Fig. S10a for $N = 4096$, where the decomposition is applied once or multiple times to break up the computation into smaller elementary DFTs. Fig. S10b shows how the total number of ADC conversions depends on the factorization. While recursively applying Cooley-Tukey decompositions reduces the total number of arithmetic operations that are performed inside the analog MVMs, it also generates more intermediate results that must be converted to digital values. Therefore, as noted in the main text, for analog systems the optimal choice for energy efficiency is to terminate the decomposition as soon as the original DFT can be factored into DFTs that are small enough to fit into one memory array. For $N = 4096$ and an array size of 512×1024, it is optimal to apply the Cooley-Tukey decomposition exactly once, e.g. with $N_1 = N_2 = 64$.

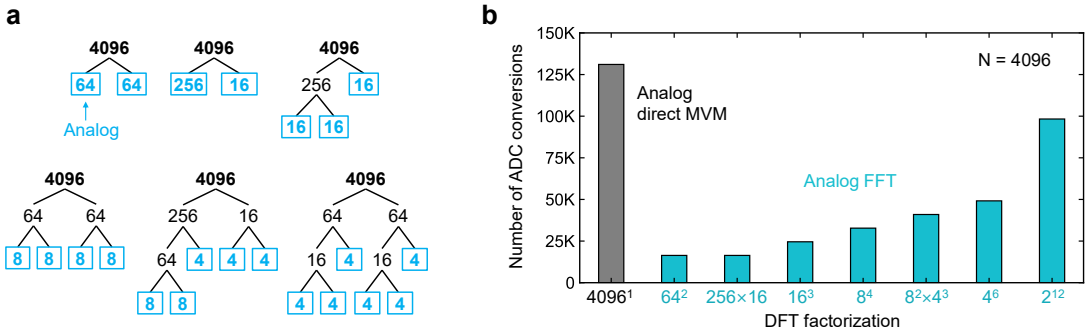

Fig. S10 (a) Several possible factorizations of a 4096-point DFT using two-factor Cooley-Tukey decompositions. Blue indicates the elementary analog DFT operations. (b) The effect of analog FFT factorization on the number of ADC conversions for a 4096-point DFT, assuming a maximum array size of 512×1024.

By contrast, in digital systems, it is generally optimal to decompose the DFT into the smallest possible radices – usually radix-2 or radix-4 – since the energy expenditure generally scales with the total number of arithmetic operations. The analogous case in Fig. S10 is the $4096 = 2^{12}$ factorization, which decomposes the computation into 2-point analog DFTs, i.e. an analog MVM implementation of the basic 2×2 butterfly operation. This is an inefficient operating point for analog MVMs, since the matrix is too small to effectively amortize the energy cost of the peripheral circuits and ADCs.

We note that the processing of radix-2 decimation-in-time FFTs has previously been proposed inside NAND flash memory arrays [69], but this method was based on analog element-wise vector multiplication rather than analog MVM operations, so it is fundamentally different from our approach. Yet, like the case described above, this scheme involves at least one ADC operation for every intermediate result of a radix-2 FFT, which incurs a high energy cost.

6.2 Audio processing accuracy with varying FFT factorizations

The analog FFT factorization can also influence the accuracy of the FFT computation by affecting the size of the analog MVM operations. To study this for FFTs with a single Cooley-Tukey decomposition, we experimentally computed the spectrograms of eight audio clips from Google's Speech Commands Dataset [70]. Most of these audio clips have 16,384 samples, for a duration of 1.024 seconds (16 kHz sampling rate). For each clip, the spectrograms were computed using STFTs with a window size of 256 samples and no window function. The STFTs were computed using the SONOS analog IMC array with different factorizations of the DFT, including the 256-point analog direct MVM.

Fig. S11a shows one of the waveforms, containing the word "stop". Fig. S11b shows the ideal spectrogram as computed using digital 256-point FFTs at FP32 precision. Fig. S11c shows the spectrogram computed experimentally using 256-point DFTs with analog direct MVMs on the SONOS array, and Fig. S11d shows the spectrogram computed using 256-point analog FFTs with $N_1 = N_2 = 16$. Both of the SONOS-computed spectrograms reproduce all of the key features of the FP32 spectrogram for the spoken word "stop", including the initial high-frequency "s" sound and the louder, lower-frequency "top" sound.

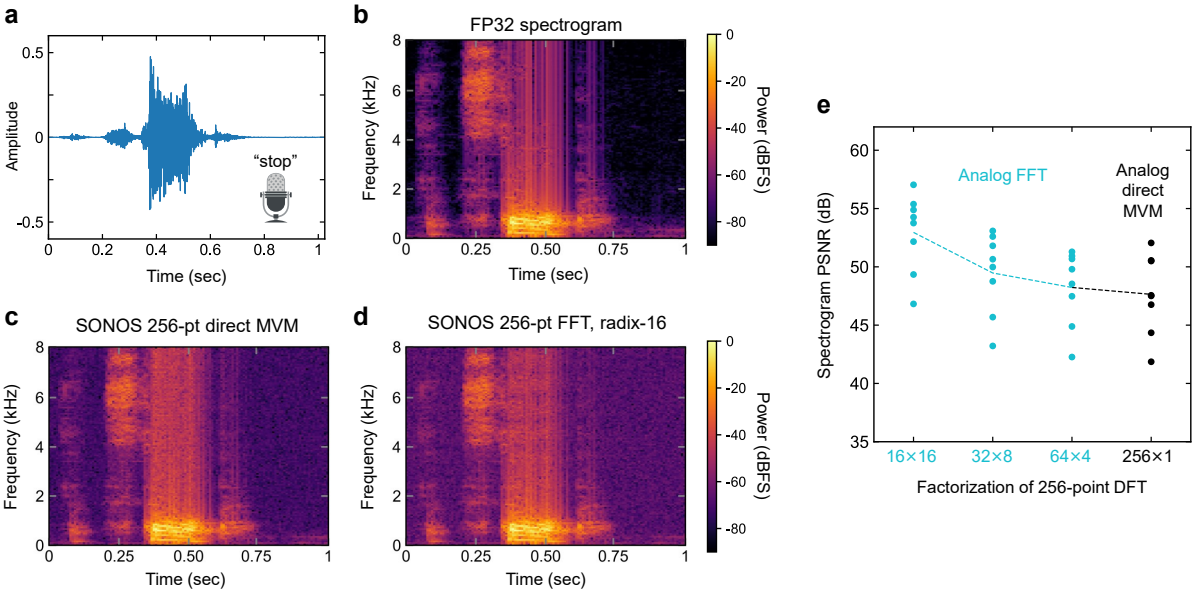

Fig. S11 (a) Audio waveform with 16,384 samples containing the spoken command "stop." (b) Spectogram of the audio waveform generated by FP32 FFTs, using rectangular windows with a size of 256 samples and a hop length of 128 samples. (c) Same spectrogram computed experimentally using 256-point analog DFTs implemented using direct MVMs on the SONOS array. (d) Same spectrogram computed using 256-point analog FFTs, factored into 16-point analog DFTs that are executed on the SONOS array. (e) PSNR of the SONOS-computed spectrogram relative to the FP32 spectrogram, for several DFT factorizations. For each factorization, eight spectrograms were generated for eight distinct command words.

We also computed spectrograms for seven other voice commands and two other factorizations of the 256-point DFT: $(N_1 = 32, N_2 = 8)$ and $(N_1 = 64, N_2 = 4)$. Fig. S11e summarizes how the FFT factorization affects the PSNR metric of the SONOS-computed spectrograms relative to the FP32 spectrogram. In general, as the size of the elementary analog DFT (the larger of the two factored DFTs) increases, there is a gradual reduction in the accuracy of the computation. This is because the larger analog DFTs accumulate a greater amount of analog error from SONOS device conductance variations and noise, as well as accumulated parasitic IR drops along the array interconnects.

The trend in Fig. S11e shows that the choice of factorization or radix for the analog FFT brings a minor trade-off between accuracy and efficiency. At the small DFT size of 256, the most energy-efficient choice is the direct MVM because the full 256-point DFT can be computed by our SONOS array without having to split the DFT matrix. The radix-16 FFT (i.e. $N_1 = N_2 = 16$) is somewhat more accurate due to the smaller MVM size, but not by a large margin. The optimal choice of DFT factorization is the one that maximizes energy efficiency while meeting the accuracy needs of the end application.

Appendix 7 Analog dot product accuracy

Fig. S12 shows the correlation between the ideal and SONOS-computed dot products from the analog IMC test chip, for different input signals and elementary DFT sizes.

The dot products in Fig. S12a were obtained from processing the speech waveform in Fig. 3a; the DFT-16 operations were used for spectrogram generation and the DFT-256 operations were used to compute the one-shot 65,536-point FFT. These dot products were computed from the same summed currents shown in Fig. 2f, after subtracting the contributions from positive and negative inputs and weights, and accumulating the result over input bits. Interestingly, while parasitic IR drops introduced systematic errors into the current sums in Fig. 2f, the dot products do not show any significant systematic errors. This is because the errors induced by IR drops cancel to a large extent when the digitized current sums for the positive and negative components are subtracted. This cancellation was faciliated by the fact that the audio input signal had a mean value close to zero. We note that while this cancellation appears on average, the IR drops are not fully canceled within the individual dot products so their effects are still non-zero. Also, this cancellation effect may be weaker for systems that have much larger parasitic metal resistance.

The dot products in Fig. S12b were obtained from the 2D image processing experiment on the "Rotterdam" image in Fig. 4b. The dot products are from the first stage of the VR-FFT, which used 16-point DFTs. Compared to the dot products in Fig. S12a, the effects of parasitic IR drops are more visible: they manifest as a systematic negative error that grows with the value of the dot product. The greater effect of parasitic IR drops in this example comes from the fact that the pixel values in the input image are strictly positive with a significant positive mean value. This positive bias means that there is less cancellation of errors due to parasitic IR drops compared to the speech processing example. This is consistent with the error profile in the 2D frequency spectrum shown in Fig. 4c, where the large low-frequency components have a systematic negative error. This positive bias is somewhat specific to this particular image processing example: in practical sensor DSP applications, we do not expect such a large bias to be present. This includes both the SAR image formation example in Fig. 5a and the automatic speech recognition example in Fig. 5b (which would have a similar error profile to Fig. S12a).

The SONOS-computed dot products show an overall close agreement with the ideal values. For the 16-point DFTs in Fig. S12a, the RMS error in the dot product is 0.35% of the maximum true dot product value in this experiment. For the 16-point DFTs in Fig. S12b, the corresponding normalized RMS dot product error is 0.81%. The larger error in the latter case is due to the lack of cancellation of errors due to parasitic IR drops, described above. For the 256-point DFTs in Fig. S12a, the normalized RMS dot product error is 1.60%. As discussed in the main text, the 256-point DFT has a larger error due to the greater amount of error accumulation in the analog sum and the smaller signal-to-noise ratio in the programmed conductances.

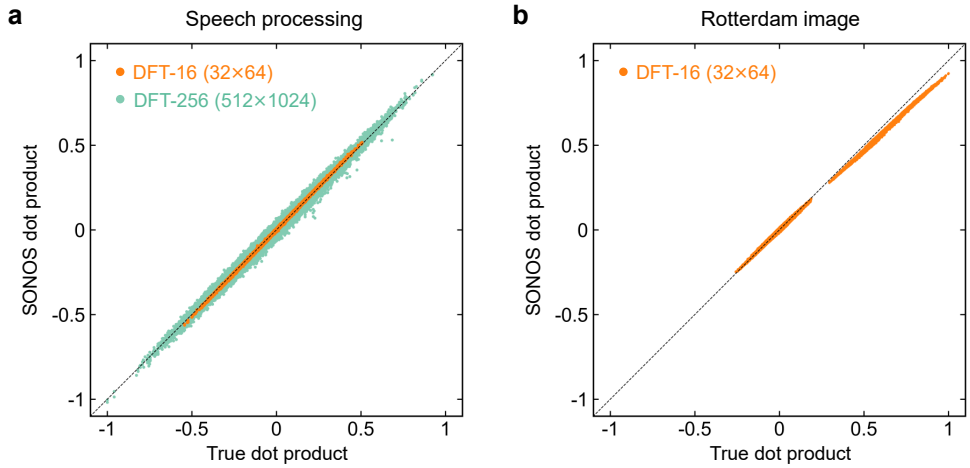

Fig. S12 Correlation between the true and SONOS-computed dot products using the analog IMC test chip, (a) for the first stage of the speech processing experiments, and (b) for the first stage of the 2D image processing experiment on the "Rotterdam" image. In (a), the dot product values have been normalized by 1.75×10^5, the maximum true dot product value for the 256-point DFTs. In (b), the values have been normalized by 2.25×10^3, the maximum true dot product value for the 16-point DFTs. The dimensions in parentheses are the size of the SONOS sub-array utilized for the computation.

Appendix 8 Image correction using Parseval's theorem

Parseval's theorem states that the total energy of the signal is preserved through an ideal DFT [71]. For an $N \times N$ 2D DFT, this is expressed as:

$$\frac{1}{N^2} \sum_j \sum_k |X_{jk}|^2 = \sum_j \sum_k |x_{jk}|^2 \tag{H8}$$

For an analog FFT, this does not exactly hold due to errors induced by the physical hardware. The loss of stored charge from the SONOS device and power dissipation in the array parasitic resistances cause a systematic loss of signal energy during the computation. For the image reconstruction examples in Fig. 4, this signal loss has the effect of reducing the brightness of the reconstructed image. We apply a first-order correction for this effect that takes advantage of Parseval's theorem. The sums on the right and left side of Equation (H8) can be evaluated digitally before and after the analog Fourier transform computation, respectively. Then, we brighten the analog reconstructed image $\mathbf{x}_\mathrm{R}$ by uniformly multiplying every pixel by a scalar that depends only on the ratio of the two sums:

$$\mathbf{x}_{\mathrm{R,\ corrected}} = \mathbf{x}_\mathrm{R} \times \sqrt{\frac{\sum_j \sum_k |x_{jk}|^2}{\sum_j \sum_k |X_{jk}|^2 / N^2}} \tag{H9}$$

As shown in Fig. S13, we find that this brightening improves the reconstructed image PSNR, though it does not always improve the SSIM. This is because a constant multiplication does not actually change any of the spatial features that were present in the uncorrected image. Therefore, the correction is unlikely to be necessary for applications that are not specifically optimizing for metrics like PSNR.

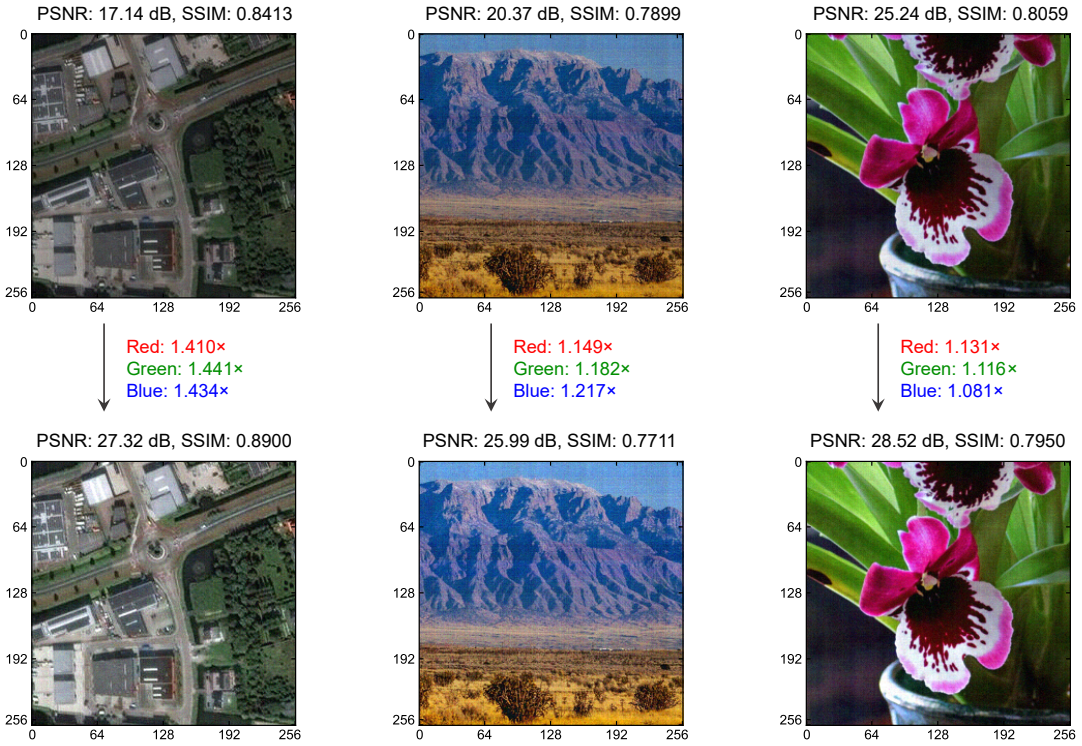

Fig. S13 (Top row) Uncorrected images reconstructed from 2D spectra computed by the SONOS array using analog VR-FFTs. (Bottom row) Reconstructed images after the channel-wise scalar correction.

Appendix 9 Additional results and details on 2D image processing

9.1 Comparison of the analog VR-FFT and direct MVM method

In this section, we compare the numerical precision of 2D DFTs computed by the analog VR-FFT and the direct MVM method for the 256×256 RGB images in Fig. 4. For the analog direct MVM, we used a SONOS sub-array programmed to the DFT-256 matrix (512×1024 devices). Fig. S14 compares the computed 2D frequency spectra and the reconstructed "Rotterdam" images for the two analog DFT methods. Because of the much larger array size of the 256-point analog DFT, we used a more compressed conductance range (0 to 1.67 µS vs. 0 to 20 µS for 16-point DFTs) to avoid saturating the ADC for this application. The direct MVM method produces significantly more degraded reconstructions with visible horizontal and vertical streaks, while the VR-FFT produced much cleaner reconstructions with higher PSNR and SSIM metrics. We performed the same comparison for the two other 256 × 256 images and observed similar results, shown in Fig. S15.

The prominent horizontal and vertical streaks in Fig. S14f trace their origin to the erroneously large values for the spectral components along $f_x = 0$ and $f_y = 0$ in Fig. S14e. When computing these specific components, the analog sum is conducted using a column of the matrix with strictly positive DFT weights that all map to $G_{\max}$. Since SONOS conductance errors increase roughly proportionally with conductance (see Fig. S5e), the devices that are programmed to $G_{\max}$ have larger absolute conductance errors than the other devices. These facts together lead to a large analog current sum on this column, with a correspondingly larger accumulation of conductance errors and IR drops compared to the other columns, which have both positive and negative weights and smaller average conductances. This explains the relatively large errors for $f_x = 0$ and $f_y = 0$ in Fig. S14e. By contrast, this feature does not appear

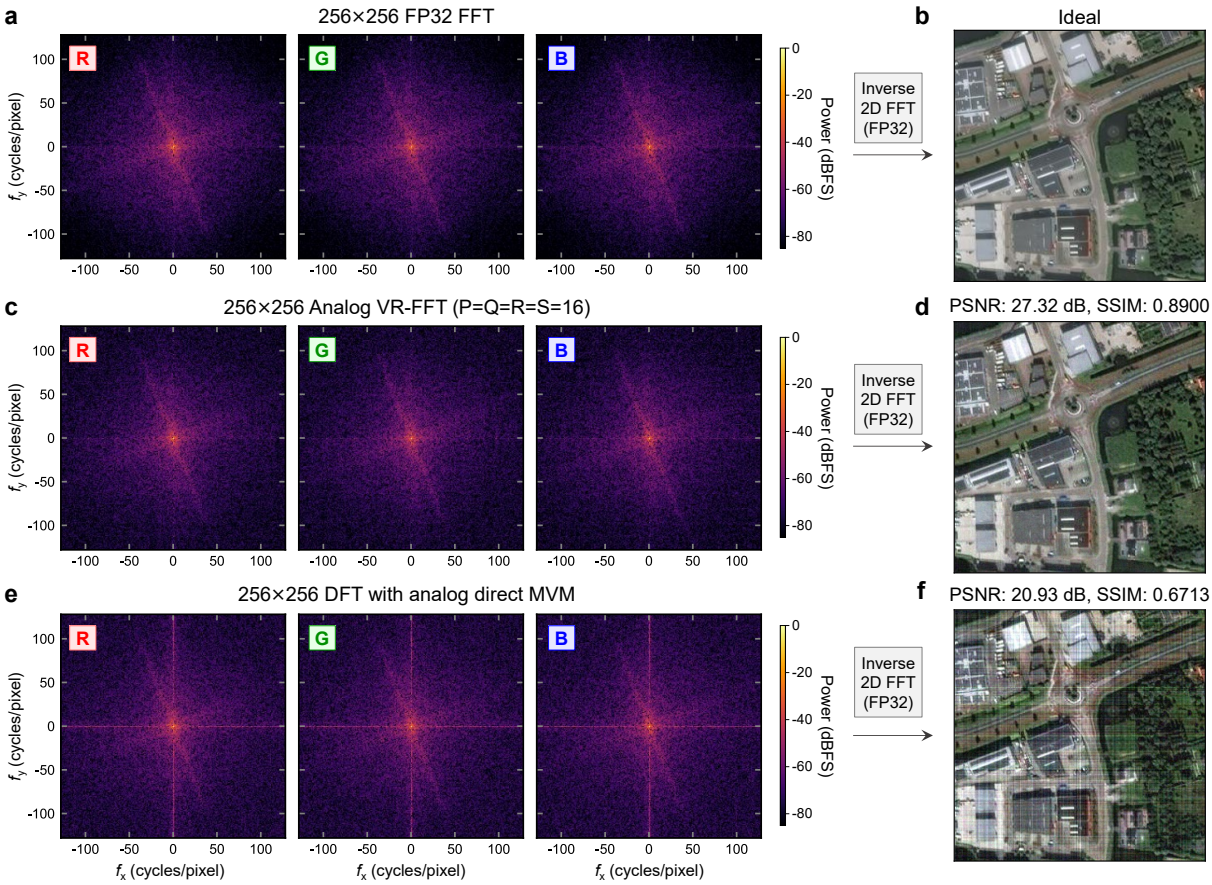

Fig. S14 (a) Ideal 2D power spectrum of the 256×256 "Rotterdam" image computed using an FP32 FFT. (b) The ideal reconstructed image, which is identical to the original image. (c) 2D power spectrum computed by the SONOS chip using the analog VR-FFT. (d) Reconstructed image from the SONOS-computed complex-valued spectrum corresponding to (c). (e) 2D power spectrum computed by the SONOS chip, via a 2D analog DFT implemented directly using MVMs. (f) Reconstructed image from the SONOS-computed complex-valued spectrum corresponding to (e).

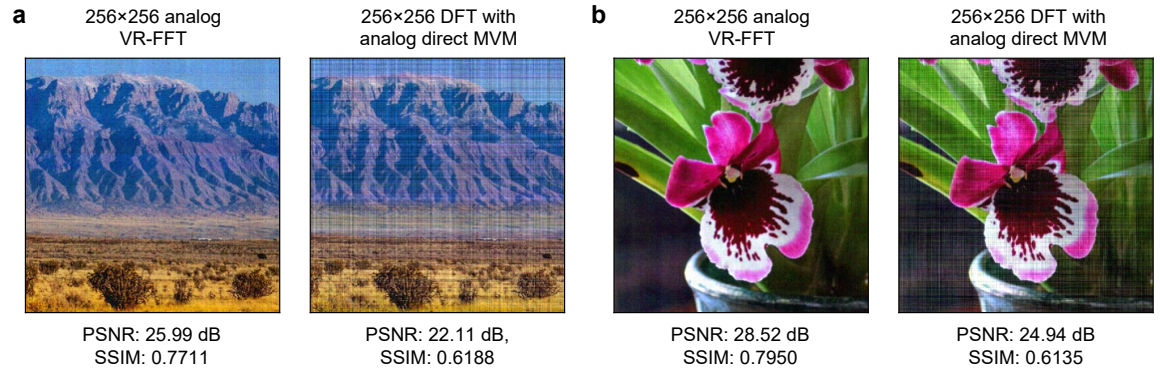

Fig. S15 Reconstructed 256×256 images from 2D frequency spectra computed by the SONOS chip using the analog VR-FFT and direct MVM methods, for (a) the "Sandia" image and (b) the "orchid" image.

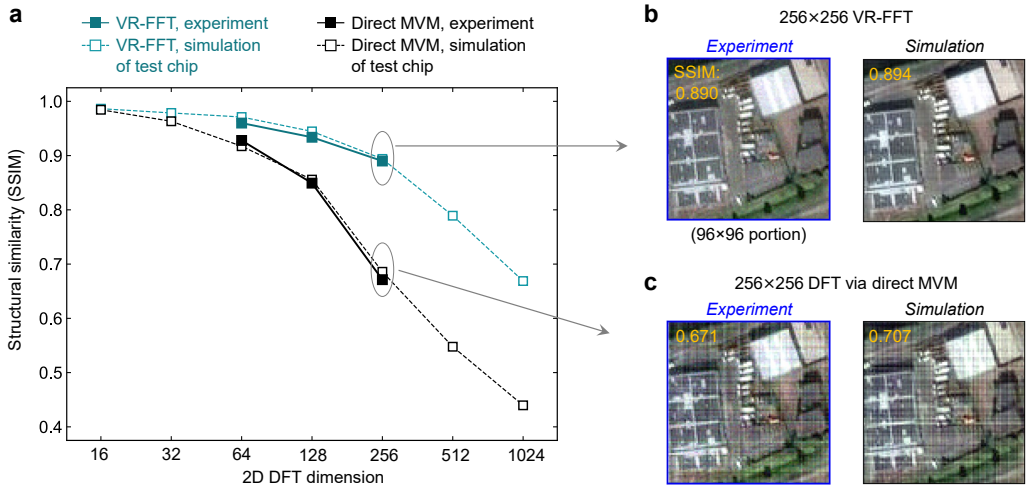

Fig. S16 (a) SSIM of the reconstructed Rotterdam image, generated from experimental and simulated analog VR-FFTs and direct MVMs at various sizes. The input was rescaled from a native resolution of 1024×1024 pixels. The simulations were configured to match the fabricated SONOS test chip. Simulated SSIM values are the average of ten Monte Carlo runs with resampled random conductance errors. The VR-FFT points are the same as the points in Fig. 5a that correspond to the test chip. (b) A 96×96 cropped region of the experimental and simulated reconstructions using the analog VR-FFT. (c) Same region of the experimental and simulated reconstructions using analog 2D DFTs implemented as direct MVMs.

in the analog VR-FFT's frequency spectrum in Fig. S14c for two reasons. First, the elementary DFTs are much smaller (16-point rather than 256-point) so both the current sums and the accumulated errors in the analog MVMs will be smaller. Second, the use of a larger $G_{\max}$ for the 16-point DFTs improved the accuracy by increasing the signal-to-noise ratio in the DFT weights. This is shown in Table S2 below, and will be explained shortly. These two factors lead to lower errors across all spectral components, but the difference is largest for the $f_x = 0$ and $f_y = 0$ components.

9.2 Image reconstruction quality vs transform size

To project how the quality of the 2D DFT scales with image size for the two methods, we experimentally processed both the analog VR-FFT and the direct MVM on the "Rotterdam" image at three different sizes (64×64, 128×128, and 256×256), then used the result to reconstruct the images. We also extended these experimental results by simulating the analog reconstruction over a larger range of sizes (from 16×16 to 1024×1024). The utilized array sizes for these experiments and simulations are shown in Table S1: for the direct MVM, only the 512-point and 1024-point DFTs are partitioned across multiple arrays. The accuracy model, which is described in Methods, replicates the characterized properties of the SONOS devices, ADCs, and metal interconnects in our fabricated chip. Fig. S16a summarizes the quality of the reconstructions vs. image size of the two methods. Two simulated reconstructions are shown in Fig. S16b and S16c, showing that the simulation accurately captures the differences between the two methods both in terms of SSIM and the experimentally observed artifacts. For both methods, the accuracy decreased for larger DFTs due to the use of larger programmed DFT matrices, which have greater accumulated conductance errors and parasitic IR drops.

DFT size	**Array size, VR-FFT**	**Max conductance, VR-FFT**	**Array size, direct MVM** (no partitioning for $N \leq 256$)	**Max conductance, direct MVM** (no partitioning for $N \leq 256$)	**Max conductance, direct MVM** (same array size as VR-FFT)
16	8 × 16	20.00 µS	32 × 64	20.00 µS	20.00 µS
32	16 × 32	20.00 µS	64 × 128	10.00 µS	20.00 µS
64	16 × 32	20.00 µS	128 × 256	5.00 µS	20.00 µS
128	32 × 64	20.00 µS	256 × 512	2.67 µS	10.00 µS
256	32 × 64	20.00 µS	512 × 1024	1.67 µS	10.00 µS
512	64 × 128	10.00 µS	512 × 1024	1.67 µS	5.83 µS
1024	64 × 128	10.00 µS	512 × 1024	1.67 µS	5.83 µS

Table S1 Utilized SONOS array size and max conductance for the simulation and experimental results in Fig. S16 and Fig. S17. For the VR-FFT with unequal radices, the array size and $G_{\max}$ are given for the larger of the two elementary DFT sizes.

Max conductance $G_{\max}$	20.00 µS	10.00 µS	5.83 µS	5.00 µS	2.67 µS	1.67 µS
Conductance SNR	141.4	84.3	62.2	58.1	47.0	42.4

Table S2 Theoretical conductance SNR for the utilized values of $G_{\max}$ in Table S1.

Table S1 (excluding the rightmost column) shows the SONOS array sizes and conductance ranges that were used for both the experimental and simulated 2D DFT results. The utilized SONOS conductance range was optimally reduced with array size to balance the effects of ADC saturation, parasitic IR drops, and loss of weight precision (see below). The direct MVM method requires the largest array size possible to stay efficient, but as a result, it more quickly loses reconstruction fidelity at large image sizes due to the factors above. By comparison, the analog VR-FFT remains significantly more accurate at large image sizes by enabling the array size to scale much more slowly with the image size.

We can quantify the overall loss of weight precision with decreasing $G_{\max}$ by computing a theoretical value for the conductance signal-to-noise ratio (SNR). We define this as the ratio of $G_{\max}$ to the average value of the condutance error σ_G, assuming for simplicity that the DFT weight magnitudes map to a uniform distribution of conductances:

$$\text{Conductance SNR} = \frac{G_{\max}}{\sigma_{\text{avg}}} = \frac{2G_{\max}^2}{\int_0^{G_{\max}} \sigma_G(G)\, dG} \tag{I10}$$

For $\sigma_G(G)$, we use the analytical fit to the characterized SONOS programming errors shown in Fig. S5e. The factor of 2 comes from the fact that when representing signed weights using a differential pair of SONOS cells, only one of the two cells contributes error: the other device can be programmed to a very low conductance state which has effectively zero error. This is a unique benefit of the SONOS device.

Table S2 shows that as $G_{\max}$ is reduced, the conductance SNR first decreases quickly, then saturates. This can be explained by the fact that in Fig. S5e, the error is proportional to the conductance when G is low, but saturates when G is high. This is because the highly conductive SONOS states are operating in the strong inversion regime, while the less conductive states are in subthreshold or weak inversion. As a result, the SNR will be higher when more of the utilized SONOS states are in the strong inversion regime. The decrease in conductance SNR at reduced $G_{\max}$ leads to accuracy loss in the analog DFTs, but this can be partially compensated by the fact that a lower $G_{\max}$ reduces the parasitic IR drops. The chosen values of $G_{\max}$ in Table S1 approximately balance these errors to minimize the accuracy loss.

9.3 VR-FFT and direct MVM comparison at the same array size

For the analog VR-FFT and direct MVM comparison in Fig. S16, we assumed for the direct MVM that the DFT matrix is partitioned only when the matrix size exceeds the maximum size of the SONOS array, which is 1024×1024. This assumption represents the most energy-efficient mode of the direct MVM, but leads to some accuracy loss as a result of the large summed currents and low $G_{\max}$. In Fig. S17, we compare to another mode of the direct MVM (purple curve), where the DFT matrix is partitioned to use the same array size as was used for the VR-FFT. We note that this mode of operation has significantly larger area and energy consumption compared to both the VR-FFT and the unpartitioned direct MVM,

due to the much larger number of ADC conversions needed for partial results. This can be roughly seen in Fig. 1d, where this case roughly corresponds to the curve for a direct MVM using a small array size.

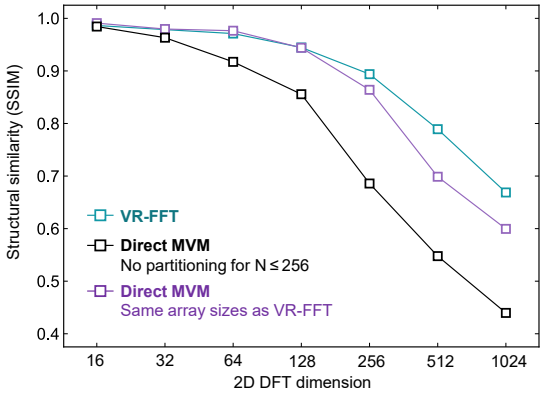

Fig. S17 Simulated SSIM of the reconstructed Rotterdam image, comparing the analog VR-FFT with two configurations of the direct MVM. For the black curve, the DFT matrix was not partitioned for DFT sizes $N \leq 256$ (same as Fig. S16a). For the purple curve, the DFT matrix was partitioned at all DFT sizes to use the same array size as the VR-FFT. In all cases shown, the simulator was configured to model the fabricated SONOS test chip.

Fig. S17 shows that using a smaller array size increases the accuracy of the direct MVM method, because the smaller arrays can have less conductance error accumulation, smaller parasitic IR drops, and better precision in the DFT weights because of a larger $G_{\max}$. However, the direct MVM is still less accurate than the VR-FFT at the same array size. In the VR-FFT, each SONOS array is programmed with a full, small-radix DFT matrix, which has a collection of both high and low conductance values. For the direct MVM case in the purple curve, each one of the many SONOS arrays is programmed with a small partition of a large DFT matrix. The DFT weight values change only by a limited amount within these partitions, so some of these partitions will have a much higher average conductance than a small-radix DFT matrix of the same dimensions, leading to larger error accumulation and ADC clipping. The ADC clipping has been mitigated by re-optimizing the $G_{\max}$ values, leading to smaller conductances compared to the VR-FFT, as shown on the rightmost column of Table S1. However, this reduces the precision of the DFT weights as shown in Table S2, so the VR-FFT still achieves a moderately higher SSIM especially for large DFT sizes.

9.4 Error decomposition of analog VR-FFT results

Here, we attempt to quantify the relative contributions of different sources of error in the analog VR-FFTs that were conducted using the SONOS test chip. While it is not possible to exactly determine these relative contributions from our experimental results, we can study this using simulations of the chip. In Fig. S18, we show how the SSIM of the Rotterdam image reconstruction changes as we selectively enable the models for the major error sources: ADC quantization and clipping, parasitic IR drops, and SONOS conductance errors (including programming errors, drift, and read noise).

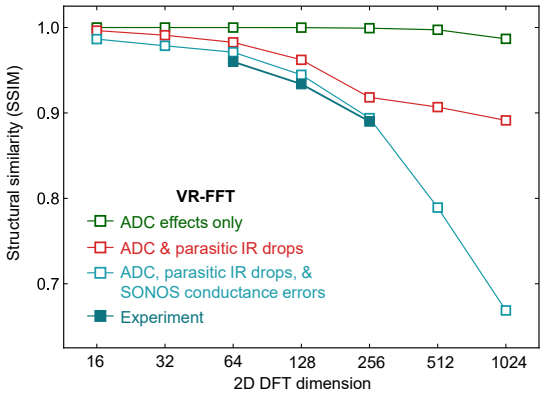

Fig. S18 Simulated SSIM of the reconstructed Rotterdam image for the analog VR-FFT, with selective enabling of different modeled error sources to show the breakdown of the error contributions to a loss of SSIM.

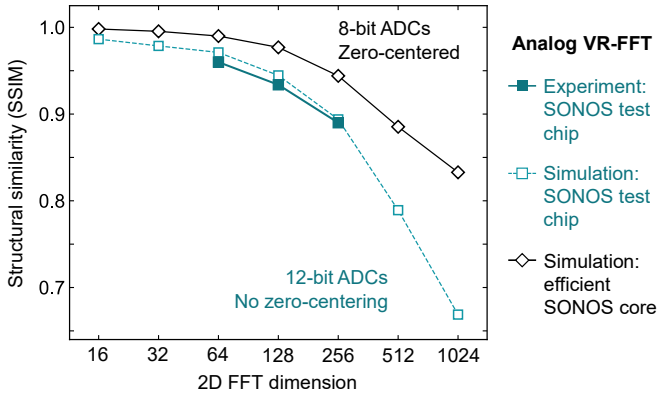

Fig. S19 Simulated SSIM of the reconstructed Rotterdam image vs analog VR-FFT transform size, comparing two hardware configurations: the 40-nm SONOS test chip, and a more optimized 40-nm SONOS core with 8-bit ADCs using zero-centered images. The teal points are the same as the points from Fig. S16a.

The test chip's ADC has a minor effect on accuracy even at large transform sizes, because of its high resolution (12 bits). Parasitic IR drops have an overall larger effect that increases with array size. The slowed rate of error growth due to IR drops for $N = 512$ and $N = 1024$ is due to the fact that the SONOS conductances were reduced to optimize accuracy, as shown in Table S1. However, as shown in Table S2, the reduction of $G_{\max}$ increases the error contribution of SONOS conductance errors by reducing the SNR in the DFT weights. This can be seen directly in Fig. S18 where the share of SSIM loss due to SONOS conductance errors increases significantly for the largest two sizes.

9.5 Simulated accuracy using test chip vs more efficient analog IMC core

The previous simulation results in this section used an accuracy model of the fabricated prototype, while the results in Fig. 5 used a model of a more efficient SONOS IMC core, shown in Fig. S23 and described in detail in Supplementary Section 11. The two accuracy simulation modes are described in more detail in the Methods section, but the most significant features of the optimized core are: (1) it uses 8-bit ADCs (rather than 12-bit), (2) it uses optimized input ranges for the ADCs, (3) it performs analog subtraction of currents from positive and negative DFT weights and inputs, and (4) it performs analog accumulation of results across input bits before the ADC. The inputs to this core were also quantized to 8 bits. Fig. S19 compares the accuracy of the two hardware configurations on the Rotterdam image construction task. One challenge with the lower-resolution 8-bit ADCs was that for the JPEG images in Fig. 4, the zero-frequency component was orders-of-magnitude larger than all the other frequency components. This led to a reduction in accuracy since the 8-bit ADCs did not quite have enough dynamic range to precisely represent all of these components. However, we found that we could recover high reconstrution SSIM if each channel of the 2D image was zero-centered (by subtracting the pixel mean) prior to the analog VR-FFT to remove the zero-frequency component. The digitally computed pixel means would then represent the zero-frequency component in the computed spectrum. This simple pre-processing step greatly reduces the dynamic range requirement on the ADCs for this specific application, and led to higher accuracies across all transform sizes for the more efficient core, as shown in Fig. S19. Importantly, we note that zero-centering is likely unnecessary for many practical sensing applications, where the signals are naturally close to zero-centered, or offsets would be normally removed by the analog front-end. This was the case for the speech audio signals in Fig. 3 and Fig. 5b. It was also true for the SAR phase history data used in Fig. 5a, where no zero-centering was used.

Appendix 10 SAR image formation using analog FFTs

Here, we provide additional simulation results on the SAR image formation exemplar shown in Fig. 5a.

10.1 Analog FFT size scaling of SAR image formation accuracy

We first show the simulated accuracy of polar-format SAR image formation for different image sizes when the analog VR-FFT is used for the 2D DFT step. In these accuracy simulations, the model for the efficient SONOS IMC core design in Fig. S23 is used, rather than the model for the fabricated chip. To evaluate smaller image sizes than the original SAR image, we started with the full 2048×2048 interpolated frequency-domain data, obtained using the polar-format algorithm up to the 2D DFT step. This frequency-domain data was then center-cropped, reducing its size by 2× to 32× in both the range and azimuth dimensions. This center crop reduces the range and azimuth resolution of the final formed image, and hence its pixel dimensions, without changing the spatial extent of the imaged scene. At each transform size, a formed image is created using both a digital FP32 FFT and a simulated analog VR-FFT. The analog VR-FFT simulations used the SONOS $G_{\max}$ values listed in Table S1 for each elementary DFT size. Specifically, for the full size 2048×2048 image, we used $G_{\max} = 5$ µS for the first stage (64-point DFT) and $G_{\max} = 10$ µS for the second stage (32-point DFT). The structural similarity is computed for the logarithm-scale analog formed image relative to the corresponding digital formed image.

The results are shown in Fig. S20a, with some example formed images shown in Fig. S20b-d. The SSIM decreases gradually with the 2D transform size. This is because a larger transform size leads to larger elementary analog DFT operations (represented by the values of P, Q, R and S), which lead to a greater analog accumulation of errors originating from SONOS conductance errors and parasitic IR drops. This is the same effect that is response for the decline of SSIM with VR-FFT transform size in Fig. S16a. However, we note that the decline in SSIM with 2D transform size is significantly smaller for the SAR image compared to the Rotterdam image used in Fig. S16a. This is because of a significant difference in the distribution of input values for these different images. As discussed in Supplementary Section 7, the natural images shown in Fig. 4, including the Rotterdam image, have strictly positive pixel values and hence a large zero-frequency component, which is orders of magnitude larger than all other frequency components. Accommodating this large component while maintaining resolution in all the other components stretches the limits of the dynamic range of 12-bit ADC, leading to some accuracy loss especially at large image sizes. However, the raw RAW sensor data does not have this strong positive bias, and there is no single component of the input or output that dominates the signal to the same extent. Therefore, a relatively high SSIM is possible at an image size of 2048×2048, even when using 8-bit ADCs.

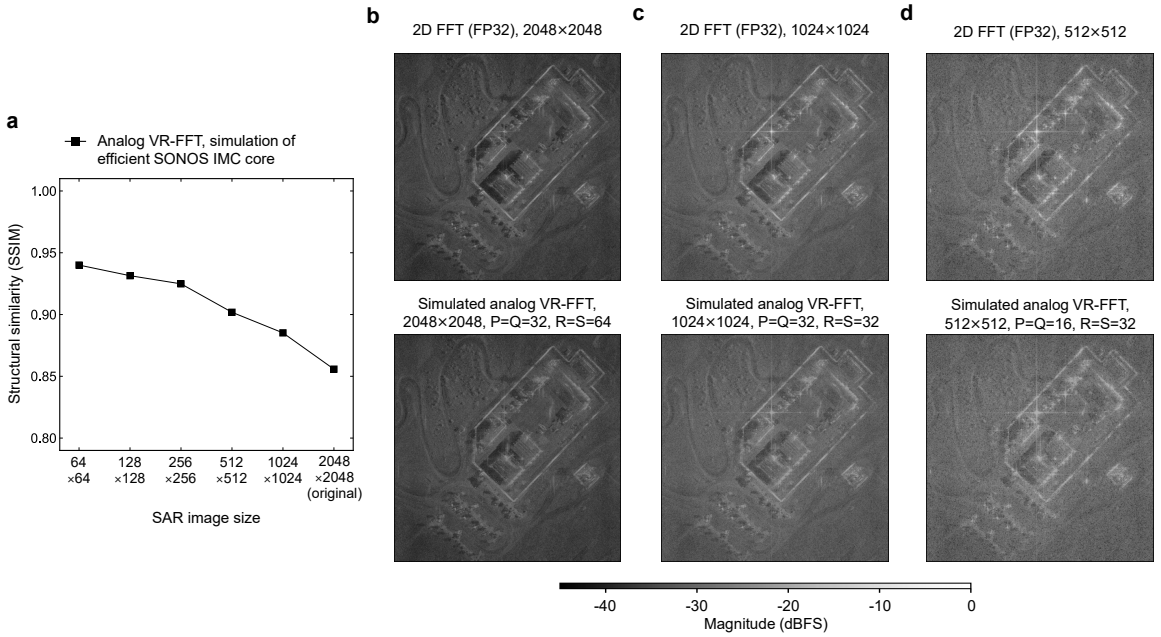

Fig. S20 (a) SSIM between the SAR images formed by a digital processor and the simulated SONOS IMC core, for different dimensions of the formed image. The same raw SAR sensor data is used as the starting point for all simulations. (b)-(d) Comparison of the SAR image formed using an FP32 2D FFT (left) and a simulated analog VR-FFT (right) as the final step of the polar-format algorithm, at three different 2D transform sizes.

10.2 Sensitivity analysis to parasitic resistance and conductance errors

For the formed SAR images using analog VR-FFTs, we now perform a sensitivity analysis to two critical hardware parameters: the parasitic resistance of the array interconnects, and the magnitude of random device conductance errors.

To study the effects of parasitic resistance, we simulate the array topology shown in Fig. S21a using the MVM circuit solver in CrossSim. This topology accurately describes both the fabricated SONOS test chip and the SONOS IMC core design in Fig. S23. The bit-wise inputs are applied as voltages on the select transistor gates (which do not draw current), the memory device is modeled as a linear resistor, and we define a parasitic metal resistance R_p between every two unit cells. For the memory devices, we use the conductance range of SONOS that was used in Fig. 5a: $G_{\max} = 5$ µS ($R_{\min} = 200\text{k}\Omega$) for the first stage which used 128×256 arrays, and $G_{\max} = 10$ µS ($R_{\min} = 100$ kΩ) for the second stage which used 64×128 arrays. We do not model any errors in the conductance to isolate the effect of IR drops, but we do include the effect of 8-bit ADCs in all simulations, which leads to a baseline SSIM of 0.967 relative to floating-point digital. Fig. S21b shows that the SSIM begins to decline sharply when $R_p > 10\Omega$. Fig. S21c shows an example of a formed image with large parasitic IR drops ($R_p = 100\Omega$). Large IR drops cause a large systematic reduction in summed currents, which in turn reduces the dot product values and leads to an overall darker image. For the 40-nm test chip, we expect the effective R_p (including the effects of series resistances at the array terminals) to be on the order of 1Ω. We note that the critical range of values for R_p will scale with the memory device resistance; using higher resistances than the ones used above for SONOS would increase the tolerance for higher R_p.

To study the sensitivity of this SAR processing to random conductance errors, we simulate image formation using two generic conductance error profiles with a parameterizable error magnitude, rather than the conductance errors that are specific to SONOS devices. In both cases, the conductance error in every device is randomly sampled from a normal distribution $\mathcal{N}(0, \sigma_G)$, where σ_G can depend on the target conductance state G. These two generic state dependences are illustrated in Fig. S21d: state-independent errors have an error magnitude that is flat across conductance, while state-proportional errors are proportional to the conductance. As can be seen in Fig. S5e, the combined effect of write errors

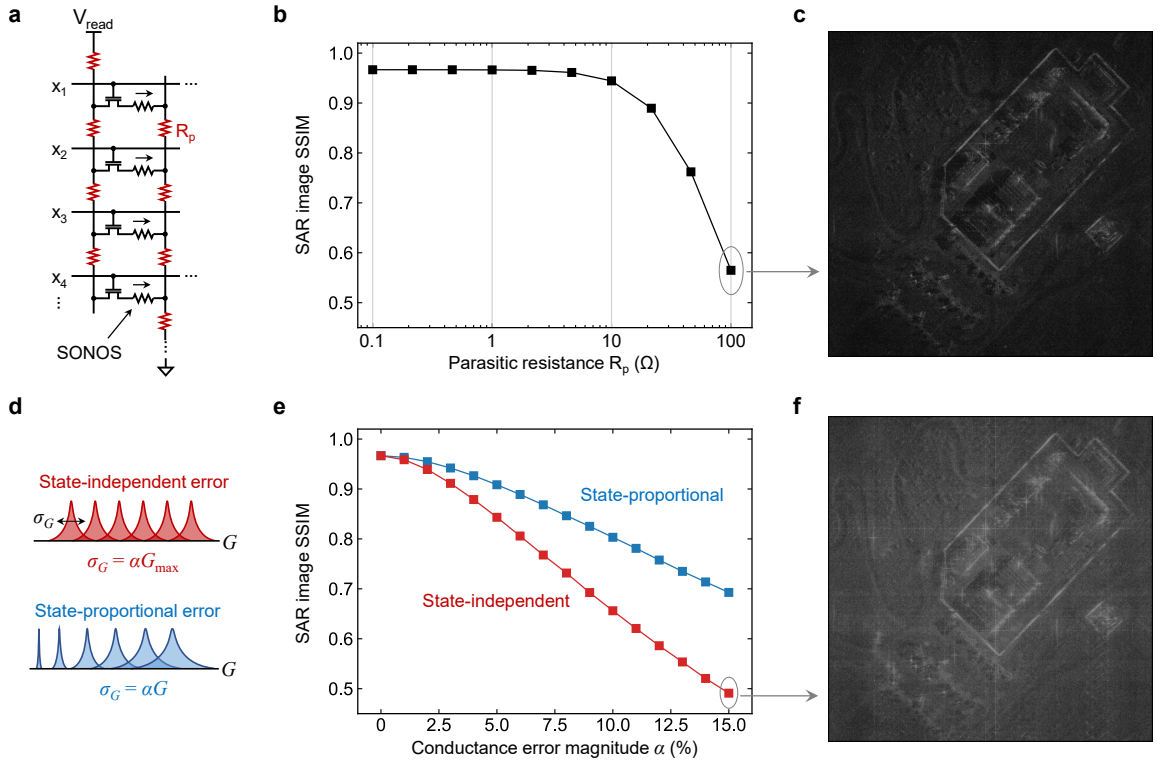

Fig. S21 Sensitivity analysis of the SSIM of formed SAR image using the analog VR-FFT. All results are on the original full-size 2048×2048 SAR image. (a) Diagram showing the simulated array topology with parasitic wire resistance. (b) Sensitivity of the SSIM to unit cell parasitic resistance with zero conductance errors. (c) Example of a formed image at the indicated point in (b). (d) Definition of state-independent and state-proportional generic conductance errors. (e) Sensitivity of the SSIM to the magnitude of each type of generic conductance error. (f) Example of a formed image at the indicated point in (e).

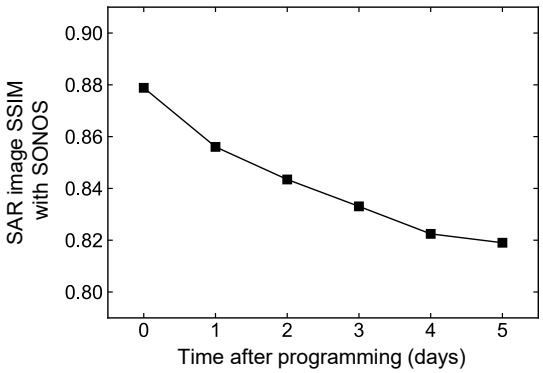

Fig. S22 Simulated SSIM of the formed SAR image using the analog VR-FFT, as a function of time after programming the SONOS devices.

and device-to-device variation in the SONOS devices has a conductance dependence that is closer to the state-proportional case, with: $\alpha \approx 11\%$ at $G = 0$ µS, $\alpha \approx 5.5\%$ at $G = 5$ µS, and $\alpha \approx 3.2\%$ at $G = 10$ µS.

Fig. S21e shows how the SSIM depends on the error magnitude α for both types of error. In general, the analog VR-FFT has similar sensitivity to state-proportional errors and state-independent errors. This is in stark contrast to DNN inference workloads, where the accuracy tends to be much less sensitive to state-proportional errors than state-independent errors [39]. The reason for this difference was discussed in Supplementary Section 4: when mapped to resistive crossbars, DFT matrices have conductance distributions that are close to uniform, while DNN weight matrices are highly concentrated around zero conductance. Therefore, kernels that rely on the DFT matrix like the analog VR-FFT have errors that do not depend strongly on the state dependence of the conductance error. This suggests that when considering random conductance errors alone, different memory devices should generally achieve similar accuracy for FFT applications if they have similar average conductance errors over their dynamic range. In Fig. S21e, the difference between the two curves mainly arises from the definition of the two errors: for the same α, the state-proportional case will have a lower average conductance error over the full range from 0 to $G_{\max}$. Fig. S21f shows an example of a formed SAR image with large state-proportional conductance errors, showing artifacts (mainly noise) that differ qualitatively from those in Fig. S21c despite the similar SSIM.

10.3 Accuracy degradation due to conductance drift

Conductance drift in the SONOS devices also causes a degradation in the SSIM of the formed SAR image over time. Here, drift refers to the combination of increasing random conductance variability over time (shown in Fig. S5e) and increasing mean shift in conductance over time (shown in Fig. S5f). The simulated change in SSIM over the first five days after programming is shown in Fig. S22, based on the SONOS drift characterization data in Fig. S5. The SSIM drops from 0.8789 to 0.8190 over this period, with a rate of decrease that slows over time, because the rate of conductance drift also slows over time.

Appendix 11 Energy, performance, and area estimation of SONOS-based analog FFT core

In this section, we describe the design of an energy-efficient analog IMC core and estimate its energy efficiency, area, and throughput for executing pipelined analog FFTs. This core uses the same 40-nm SONOS technology and uses the size of the SONOS array in the fabricated test chip (1024×1024) as an upper bound, but with more optimal peripheral circuits, digital buffering, and dataflow. This design is roughly based on the 40-nm analog IMC core design in Ref. 45, but with several modifications as noted below.

11.1 Pipelined analog MVM core operation

Fig. S23 shows the design of the analog IMC core that can fully execute a DFT using a single analog MVM; i.e. there is a single ADC conversion for each real or imaginary output of the DFT. The digital inputs and outputs are sign-magnitude integers. The 2T SONOS cell and its operating bias are the same as for the array on the test chip, shown in Fig. 2a. However, the DFT mapping in Fig. 2b is modified to allow for simultaneous processing of positive- and negative-valued inputs. Since we operate the SONOS cells to conduct current only in one direction, this means that the array needs $4K \times 4K$ cells to execute a K-point complex DFT. The maximum DFT size that can be computed by a single 1024×1024 array is $K = 256$. The columns of the array are held at virtual ground by current conveyors (CCs), which also pass the current from the column to an output node with a current gain of either +1 or −1. Opposing gains from two CCs are used to subtract summed currents from positive and negative terms in the dot product, prior to digitization by the ADC.

The SONOS array processes the input vector bit-serially, but the bit-wise partial dot products are accumulated in the analog domain using the successive integration and rescaling technique to reduce the ADC energy consumption [72]. For a given input bit, the differential current from the two CC's is integrated on an integration capacitor ($C_{\text{int}} = 150$ fF), which can be implemented as a metal-oxide-metal (MOM) capacitor using multiple metal layers. After integration, the capacitor is disconnected from the array and connected to a second identical capacitor ($C_{\text{div}} = 150$ fF) to halve the charge and voltage

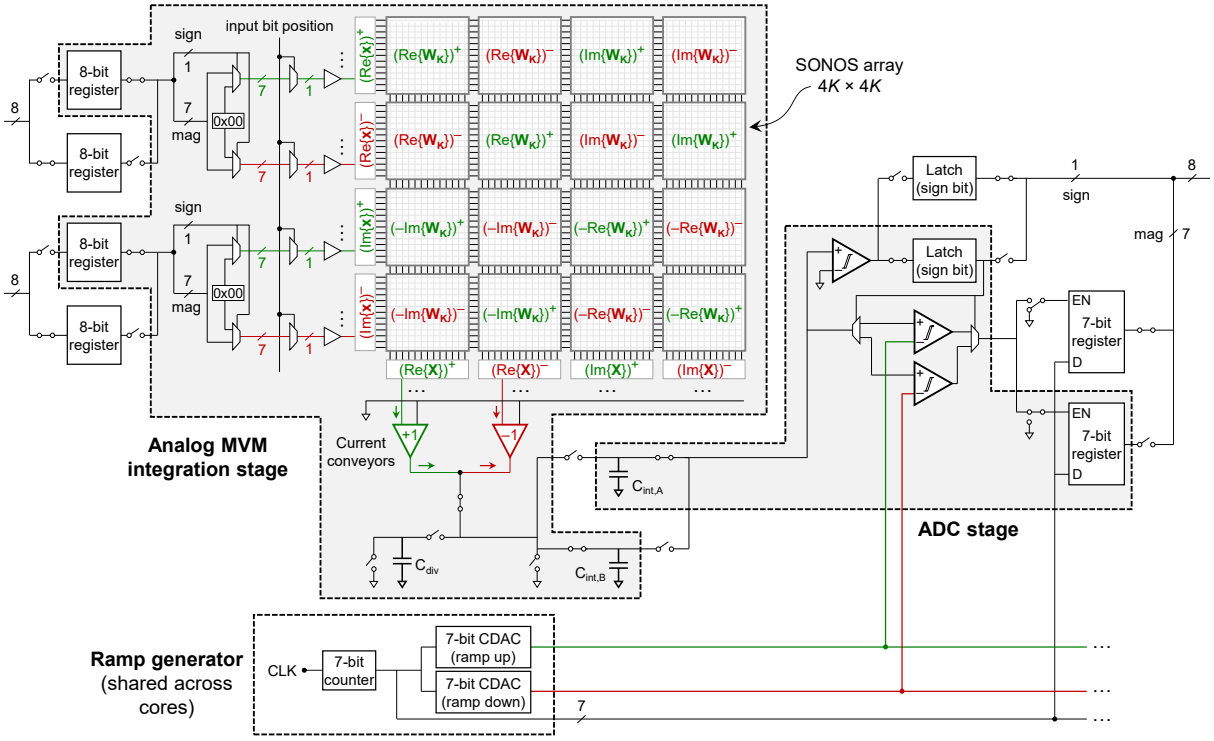

Fig. S23 High-level diagram of a SONOS analog IMC core for executing pipelined analog FFTs, shown for an input and output resolution of 8 bits. The core fully computes a K-point DFT using a single analog MVM operation. The different highlighted blocks represent pipelined stages that can be occupied by independent data batches. Different logical partitions of the SONOS array are shown, but there is no physical separation between these partitions.

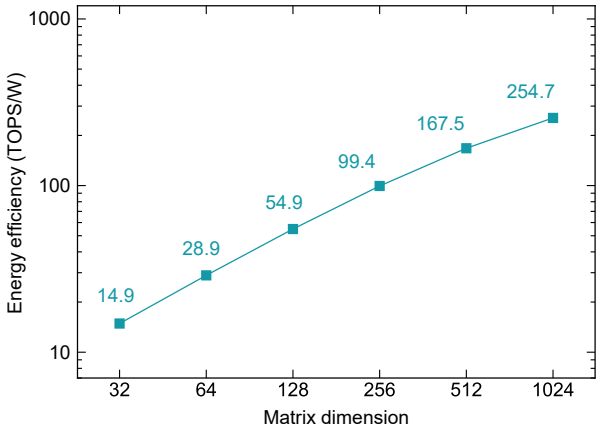

Fig. S24 Energy efficiency of MVMs using the analog IMC core in Fig. S23 for a real-valued matrix. An operation is defined at 8-bit precision for real values.

on C_{int}. For the next input bit, current is integrated on the accumulated charge on C_{int} while C_{div} is discharged. Repeating this process for seven integration cycles (for the seven magnitude bits) implements an analog charge-domain shift-and-add accumulation. The cycle time for each input bit is assumed to be 5 ns, which allows ample time for the array to settle [73]. This also allows a 150 fF capacitor to integrate a differential current of up to ∼30 µA per input bit with a supply voltage of 1V. Based on our accuracy simulations, this is more than enough to run all of the FFT workloads studied in this paper.

We implement double (ping-pong) buffering of the integration capacitor to allow the analog MVM integration stage to be pipelined with the subsequent ADC stage. Each capacitor is used for integration in one cycle, then is used to hold the integrated voltage for the ADC stage in the next cycle. We use a ramp ADC, which allows the analog dot products from all the columns to be digitized in parallel with a small footprint per column. We find this to be an optimal choice at 8-bit resolution, though for higher precision, a successive-approximation-register (SAR) ADC may be optimal [66]. To increase speed, we use a first comparator stage to detect the sign bit. Then, based on the sign bit, the input voltage is compared to one of two voltage ramp signals (ramp-up or ramp-down). The ramp generation circuitry consists of a counter and two capacitive digital-to-analog converters (CDACs) that are driven by a 1 GHz clock. We assume that each ramp generator can be shared by 1024 active columns, which can be distributed to one or more arrays depending on the DFT size. When the comparator in this stage switches, the counter's value is latched to a 7-bit register which contains the magnitude bits. The registers that store each 8-bit output are also double buffered to enable pipelining of the ADC operation with the subsequent stage, e.g. writing the intermediate digital outputs to SRAM.

11.2 Energy consumption

We estimate the energy consumption of the analog FFT for various FFT sizes. To simplify the analysis, we lump the energy costs into a total energy per 8-bit output value (real or imaginary) of an analog DFT operation. As described in Supplementary Section 1, using the parallel analog FFT implementation enables the twiddle factor multiplications to be folded into the analog MVMs, so that they do not incur any additional energy cost. The dominant energy contributions are summarized below:

- **SONOS array**: We include energy dissipation in the SONOS devices that draw current, and the CV^2 energy to charge the select gate lines from 0V to 2.5V. We assume $G_{\text{max}} = 16.7$ µS and $G_{\text{min}} = 10$ pS, based on the large on/off ratio of the SONOS device shown in Fig. S4c. There are at most $4K$ SONOS cells that contribute to a given digital output, since at least half the rows will be inactive due to input sign. The voltage across each cell's current-conducting terminals is 0.06V and power is dissipated for seven cycles. The average conductance for a DFT weight is $\approx 0.32 G_{\text{max}}$. We assume an input activity factor of 25%, averaged over input bits. For CV^2, we use values for the metal interconnect capacitance per length, SONOS cell dimensions, and the select gate capacitance from Ref. 45, which is based on the same 40-nm process. The total energy consumption in the array is estimated as:
  - IV energy: 0.011 pJ/output ($K = 16$) to 0.17 pJ/output ($K = 256$)
  - CV^2 energy: 0.11 pJ/output ($K = 16$) to 1.8 pJ/output ($K = 256$)

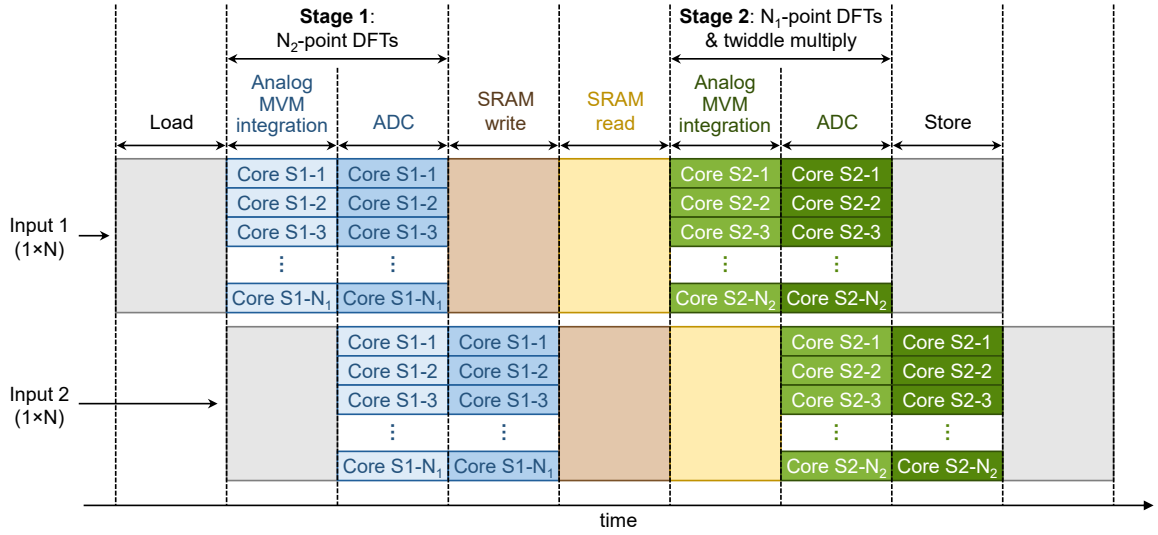

Fig. S25 Dataflow diagram showing the pipelined execution of the parallel analog N-point FFT in Fig. S1.

- **Integrators**: We assume that two optimally designed CC's dissipate 21.6 µW of power each, based on the fast CCII design that is used for analog IMC in Ref. 73. Integration over seven cycles leads to a total energy consumption of 1.5 pJ/output.
- **ADC**: The dominant energy contribution in the ADC step is the three comparators in Fig. S23. The energy consumption of the ramp generator is negligible since it is amortized across many digital outputs. Based on circuit simulations in a commercial 40-nm process for a similar design [45], the total energy consumption for an 8-bit conversion is 2.1 pJ/output. This is about 8× more energy than the limit for 8-bit ADCs from a well-known ADC survey [74]. (A SAR ADC can potentially operate closer to the limit, but consumes more area.)
- **SRAM access**: The digital outputs of the first DFT stage must be written to local SRAM buffers, then the values must be read out from SRAM for the second DFT stage. We assume that each analog IMC array can write to an independent SRAM bank with an 8-bit block size. We use CACTI 7.0 to estimate the access energy, latency, and area, using a custom technology file for a commercial 40-nm process [75]. The SRAM access energy, averaged over reads and writes, is 0.56 pJ/output. This energy is not included for small DFTs ($N \leq 256$) that can be implemented with a single MVM, and thus has no intermediate results.

The estimated total energy per digital output varies from 4.3 pJ to 5.5 pJ/output, depending on the matrix size. Fig. S24 expresses the equivalent energy efficiency in TeraOperations/s/W (TOPS/W) of real-valued MVMs using the analog IMC core. Since the energy consumption is dominated by peripheral circuits especially at smaller array sizes, the efficiency (in TOPS/W) increases directly with the size of the matrix and would have nearly the same value for FFTs and DNN layers. To obtain the total DFT energy consumption, the per-output energy consumption is multiplied by the total number of intermediate and final digital outputs of the N-point DFT computation. This is equal to $2N$ for small DFTs that can be implemented as a single MVM, and is equal to $4N_1N_2 = 4N$ for the analog FFT with a single Cooley-Tukey decomposition. These results are plotted in Fig. 5c and compared to state-of-the-art digital FFT processors.

As a point of reference, we compare specifically to the efficiency of the AMD Versal AI core, which can accelerate both DSP and ML applications. At the same 8-bit precision, the analog IMC core can compute FFTs with at least 60× higher efficiency for the FFT sizes from 64 to 2048 evaluated in Fig. 5c. For matrix multiplication, the analog IMC core is more efficient (in terms of TOPS/W) than the Versal by a factor of 36×, 65×, 110×, and 167×, for matrices containing 128, 256, 512, and 1024 rows, respectively [76].

11.3 FFT throughput and latency

For throughput estimation, we focus on the 4096-point FFT design point, which is a particularly relevant size for 5G wireless communications [29, 57], though the cores can be dynamically re-configured to compute other FFT sizes. This requires elementary DFTs of size $N_1 = N_2 = 64$. To attain high throughput, we use the parallel FFT scheme in Fig. S1, where the independent analog DFTs within each stage of the FFT are computed in parallel on multiple arrays. We further increase throughput by pipelining the

stages of the analog FFT as shown in Fig. S25, which is supported by ping-pong buffers at the boundaries between stages. Some of these buffers are shown in Fig. S23. The SRAM memory is also double buffered. We also allocate a stage to load the input elements into the core's ping-pong input buffers in the correct order. These buffers allow multiple independent FFTs to be processed concurrently in different stages of the pipeline.

The FFT throughput is set by the length of a single pipeline stage. This length is set by the limiting step, which is the digitization of analog DFT outputs using the ramp ADC. For an 8-bit ADC, the latency of this step is 130 ns, or 130 clock cycles at 1 GHz: two cycles for sign detection and 128 cycles for the 7-bit ramp to determine the magnitude. Meanwhile, the analog MVM integration stage takes 42 ns to integrate all of the input bits. The latency of SRAM access is 0.43 ns per 8-bit word (using CACTI), so the latency to read or write 128 words as needed for a 64-point DFT is at most ∼55 ns. Therefore, with the analog IMC cores working in parallel, a 4096-point FFT can be completed once every 130 ns, and the throughput (in GigaSamples/s) is:

$$\text{FFT throughput} = 4096\,\text{samples} \,/\, 130\,\text{ns} = \mathbf{31.5\ GSamples/s}$$

The latency of the 1D 4096-point FFT computation is the total time needed for a computation to traverse the full pipeline in Fig. S25. Since there are eight pipeline stages that all have the same length of 130 ns, the latency is:

$$\text{Latency of 4096-point FFT} = 8 \times 130\,\text{ns} = \mathbf{1040\ ns}$$

We can quantify the raw compute throughput of the accelerator in TOPS. The 4096-point analog FFT implementation involves 64 MVMs in the first stage and 64 MVMs in the second stage. Each MVM is a multiplication between a 64×64 complex matrix and a 1×64 complex vector, which has $2 \times 128 \times 128 = 32768$ real operations (multiply and add counted separately). A 4096-point FFT completes every 130 ns. Therefore, the compute throughput is:

$$\text{Compute throughput} = 2 \times 64 \times 32768\,\text{operations} \,/\, 130\,\text{ns} = \mathbf{32.3\ TOPS}$$

11.4 Area estimation

To estimate the area-normalized performance of the analog FFT processor, we again focus on the 4096-point FFT design point described above. This implementation requires 128 analog IMC cores that each contains a 256×256 SONOS array. It also requires 16KB of SRAM memory to buffer the intermediate results, and 16 ramp generators for the ADCs that are shared by 8 IMC cores each. Since the IMC core design is similar to that in Ref. 45, which was based on the same 40-nm process, we use the methods from that work to estimate the area of all components of the IMC core in Fig. S23. We note that these are based on summed component areas rather than a full physical layout, so we have conservatively included an additional 25% area overhead within the analog IMC core for wiring and a basic digital control unit. We also use CACTI to estimate the area of the SRAM buffer. SONOS flash arrays require charge pump circuits to generate the voltages needed for programming. Since the SONOS arrays need only to be infrequently programmed (i.e. once every few days to reset the effects of drift), a set of charge pumps can be shared by multiple arrays. To roughly estimate its area, we follow the 40-nm flash AIMC chip in Ref. [21], where a single set of charge pumps with ∼2.0 mm^2 area was shared by 16 flash arrays that

Contribution	40-nm design	22-nm design
SONOS array	0.839 mm^2	0.254 mm^2
Row logic and drivers	0.424 mm^2	0.221 mm^2
Column analog peripheral circuits (including integration capacitors)	1.663 mm^2	0.973 mm^2
Column comparators	0.208 mm^2	0.063 mm^2
Output registers	0.629 mm^2	0.190 mm^2
SRAM	0.081 mm^2	0.019 mm^2
Ramp generators	0.056 mm^2	0.017 mm^2
Control and wiring layout overhead	0.975 mm^2	0.482 mm^2
Charge pumps	0.500 mm^2	0.339 mm^2
Total	**5.374 mm^2**	**2.558 mm^2**

Table S3 Area breakdown of the 4096-point analog FFT designs.

had a total of 33.5M devices. The 4096-point FFT design needs a total of 8.4M devices, so we estimate the corresponding share of charge pump area required to be 0.5 mm^2. The estimated total area for the 4096-point FFT design is 5.37 mm^2. The area breakdown is summarized in Table S3.

The area-normalized FFT throughput and compute throughput of this design are:

40-nm area-normalized FFT throughput = (31.5 GSamples/s) / 5.37 mm^2 = **5.87 GSamples/s/mm^2**

40-nm area-normalized compute throughput = 32.3 TOPS / 5.37 mm^2 = **6.01 TOPS/mm^2**

A 22-nm SONOS flash memory is being developed for analog IMC applications [46], so we also estimate the area of a 22-nm implementation of the analog IMC core. We assume a simple quadratic scaling of the area of the transistors and the SONOS cells. The density of the MOM capacitors increases by ~47% from the 40-nm node to the 22-nm node, from 5.9 fF/μm^2 to 8.7 fF/μm^2, due to the availability of additional metal layers [77]. We also use this capacitance density scaling to project the area reduction of the charge pumps. We estimate that these changes reduce the total area to 2.56 mm^2, leading to an area-normalized FFT throughput of 12.3 GigaSamples/s/mm^2.

22-nm area-normalized FFT throughput = (31.5 GSamples/s) / 2.56 mm^2 = **12.3 GSamples/s/mm^2**

22-nm area-normalized compute throughput = 32.3 TOPS / 2.56 mm^2 = **12.6 TOPS/mm^2**

Appendix 12 Asymptotic scaling laws for the analog FFT

In this section, we derive mathematical scaling laws for the energy, area, and performance of the analog FFT and the analog direct MVM method, summarized in Table S4. We note that these are theoretical, asymptotic scaling laws whose purpose is to illustrate the feasibility (or infeasibility) of scaling to very large DFT sizes, and do not account for the actual costs of the underlying hardware operations (e.g. ADC conversions) or effects at small DFT size, which were modeled in Supplementary Section 11. By comparison, digital FFT algorithms typically follow a $\mathcal{O}(N\log_2 N)$ scaling for both time and energy [22], though the actual FFT processor may follow a different scaling law because the hardware is optimized to be most efficient at one or a few specific FFT sizes. The analysis here considers 1D DFTs in the limit of large DFT size N, but can be straightforwardly generalized to two or more dimensions. The explanations for these scaling laws are given below.

DFT processing method	**Energy scaling**	**Area scaling**	**Time scaling**
Analog FFT	$\mathcal{O}(N\log_K N)$	Analog: $\mathcal{O}(K^3)$ or $\mathcal{O}(K^2)$* Buffering: $\mathcal{O}(N\log_K N)$	MVMs: $\mathcal{O}(1)$ or $\mathcal{O}\left(\frac{N}{K^2}\log_K N\right)$ † Buffering: $\mathcal{O}(N\log_K N)$
Analog direct MVM	$\mathcal{O}\left(\frac{N^2}{K}\right)$	$\mathcal{O}(N^2)$ or $\mathcal{O}\left(\frac{N^2}{K}\right)$*	MVMs: $\mathcal{O}(1)$ Digital adds: $\mathcal{O}\left(\log_2 \frac{N}{K}\right)$

Table S4 Asymptotic scaling laws for the energy, area, and time overheads of different analog DFT processing methods. *The area scaling depends on whether the memory elements or peripheral circuits dominate the area. †If Cooley-Tukey decomposition is only applied once, the scaling is $\mathcal{O}(1)$.

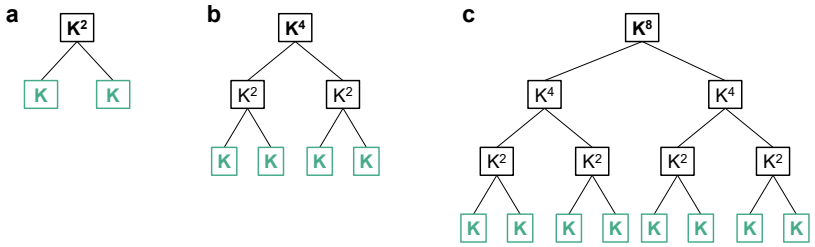

Fig. S26 Cooley-Tukey decompositions for three exemplary DFT sizes: (a) $N = K^2$, (b) $N = K^4$, and (c) $N = K^8$, where K is the largest analog DFT that can fit in a single resistive crossbar array.

12.1 Energy scaling of the analog FFT

To analyze the energy scaling properties, we will use the basic assumption that the energy of an analog MVM is dominated by the output peripheral circuits such as TIAs, integrators, and ADCs. This has been true for published analog IMC accelerators that use 8-bit or higher-resolution ADCs [12, 17, 34], and for the analog core analyzed in Supplementary Section 11. While DNNs can be trained to tolerate lower precision, we will assume that DSP applications require at least 8-bit ADC outputs. When peripheral circuits dominate the energy, the analog MVM's energy scales with the number of output values. For the full analog FFT, we account for the energy of analog MVMs, the energy of digital twiddle multiplications if needed, and the energy of intermediate reads and writes to digital buffers.

We consider the three exemplary DFT sizes in Fig. S26. The $N = K^2$ case in Fig. S26a is the largest DFT that can be computed using only one application of Cooley-Tukey decomposition. Following the procedure described in the main text, this involves two sets of K analog DFTs of size K. Each analog DFT has $2K$ ADC conversions (for the real and imaginary outputs), so the total number of ADC conversions for the K^2-point analog FFT is: $n_{\mathrm{ADC}}(K^2) = K \cdot 2K + K \cdot 2K = 4K^2$. We now consider the $N = K^4$ case in Fig. S26b, which is the largest DFT that can be computed using a Cooley-Tukey decomposition tree of depth ≤ 2. At the top level, this DFT is factored into two sets of K^2 DFTs of size K^2. Each K^2-point DFT can be computed using the analog FFT in Fig. S26a, so the total number of ADC conversions is: $n_{\mathrm{ADC}}(K^4) = 2 \cdot K^2 \cdot n_{\mathrm{ADC}}(K^2) = 8K^4$. Applying the same method, the total number of ADC conversions for the $N = K^8$ case in Fig. S26c is found to be: $n_{\mathrm{ADC}}(K^8) = 2 \cdot K^4 \cdot n_{\mathrm{ADC}}(K^4) = 16K^8$. For these three cases, the number of ADC conversions scales as $2N\log_K N$, and this $\mathcal{O}(N\log_K N)$ scaling law for

the number of ADC conversions holds generally for increasing N. The sequential analog FFT in Fig. 1b and the parallel analog FFT in Fig. S1 have the same number of ADC conversions, so the same energy scaling law applies to both.

Since the twiddle factors are multiplied element-wise with the digitized first-stage DFT outputs, the number of multiplications scales proportionally with the number of ADC conversions. The same is true for the number of buffered intermediate results. We note that no digital twiddle multiplications are needed if using the parallel FFT scheme with only one Cooley-Tukey decomposition. Nonetheless, because all major contributions to the energy of the analog FFT follow the same worst-case asymptotic scaling behavior, the energy of the analog FFT scales as $\mathcal{O}(N\log_K N)$.

12.2 Time scaling of parallel analog FFTs

In an analog MVM, all of the multiply-accumulate operations are processed in parallel across the full array. We also assume that the time to digitize analog MVM results does not scale with array size; this can be accomplished with a ramp ADC, or by increasing the number of ADCs together with the number of array columns. Under these assumptions, the latency of a single elementary analog DFT is $\mathcal{O}(1)$.

Our analysis is based on the parallel analog FFT scheme in Fig. S1. First, consider a single Cooley-Tukey decomposition ($N = K^2$). Because the MVMs occur in parallel and there are no digital twiddle multiplications, the time associated with each stage is $\mathcal{O}(1)$. Therefore, the combined time scaling for both stages of the analog FFT is $\mathcal{O}(1)$.

When performing more than one level of Cooley-Tukey decomposition, we only assume that the lowest level of the decomposition is parallelized in order to maintain a relatively small footprint. Consider the case of two decompositions ($N = K^4$): this requires sequentially performing $2K^2$ DFTs of size K^2, each of which has a time cost of $\mathcal{O}(1)$. Similarly, the third level of decomposition ($N = K^8$) requires $4K^6$ DFTs of size K^2. Continuing this pattern, we find that the asymptotic time scaling associated with analog MVMs is $\mathcal{O}((N/K^2)\log_K N)$. We note that if Cooley-Tukey decomposition is applied more than once, then digital twiddle multiplications are still needed in the higher-level decompositions.

We assume that the time associated with buffering intermediate results scales with the number of intermediate results: $\mathcal{O}(N\log_K N)$. While this scales faster asymptotically than the time cost of analog MVMs, it will have a very different proportionality costant. Furthermore, the analog MVMs in the first stage, the storage of intermediate results, and the analog MVMs of the second stage can all be pipelined to increase throughput.

12.3 Area scaling of parallel analog FFTs

For a single resistive crossbar that implements a K-point analog DFT, the area scales as $\mathcal{O}(K^2)$ if the memory elements dominate the area. For highly scaled memory technologies, the area may instead be dominated by peripheral circuits, which would scale as $\mathcal{O}(K)$. For the parallel FFT implementation, we would allocate K arrays of the above size to implement the first stage of the Cooley-Tukey decomposition, and another K arrays to implement the second stage. The total area scales as either $\mathcal{O}(K^3)$ if the memory elements dominate, or $\mathcal{O}(K^2)$ if the peripheral circuits dominate. The scaling remains the same for multiple levels of Cooley-Tukey decomposition, since as mentioned above, the same arrays would be used to process the higher-level DFTs sequentially. Meanwhile, since a matrix transpose is still needed between the two stages of the parallelized analog FFT, the area overhead of intermediate digital storage does not meaningfully change. This overhead scales as $\mathcal{O}(N\log_K N)$, following the scaling of the number of intermediate results that need to be stored, as described above.

12.4 Scaling laws for analog DFTs using direct MVMs

A direct analog MVM mapping of a large DFT would require the DFT matrix to be split up across many arrays. In this case, K is proportional to the maximum dimension of a given array in this partition. The number of outputs for an N-point DFT scales as N, and each of these outputs must be obtained by digitally summing the partial results of N/K ADC conversions from different arrays. Therefore, the number of ADC conversions and the number of digital additions would both scale as $\mathcal{O}(N^2/K)$, and this is the overall energy scaling of the direct MVM approach.

Since the direct MVM approach stores every element of the matrix $\mathbf{W}_N$ and does not require digital buffering, the area scaling is straightforward. The overall area scaling is $\mathcal{O}(N^2)$ if memory elements dominate the area, and is $\mathcal{O}(N^2/K)$ if the peripheral circuits dominate the area. For the digital additions,

we assume that enough adders are allocated so that partial results for each DFT output can be added in parallel to increase throughput. This would require $\mathcal{O}(N^2/K)$ digital adders.

In terms of performance, all of the analog MVMs across all of the arrays implementing the DFT can in principle be performed simultaneously, so the time complexity of the analog processing is $\mathcal{O}(1)$. The digitized partial sums would then need to be accumulated. Assuming as above that partial sums are added in parallel, the optimal throughput can be obtained by using an adder tree for each DFT output. This would lead to a time complexity of $\mathcal{O}(\log_2(N/K))$ for the partial sum accumulations.